Universidade do Minho
Escola de Ciências

Abbas M. K. AL-Rjoub

Design, fabrication, characterization and aging studies of solar selective absorber surfaces

março de 2019

Design, fabrication, characterization and aging studies of solar selective absorber surfaces
Abbas M. K. AL-Rjoub
UMinho | 2019

Universidade do Minho
Escola de Ciências

Abbas M. K. AL-Rjoub

Design, fabrication, characterization and aging studies of solar selective absorber surfaces

Tese de Doutoramento
Programa Doutoral em Física (MAP- fis)

Trabalho efetuado sob a orientação do
Luís Manuel Fernandes Rebouta

e sob co-orientação de
Senentxu Lanceros-Mendez

março de 2019

STATEMENT OF INEGRITY

I hereby declare having conduced my thesis with integrity. I confirm that I have not used plagiarism or any form of falsification of results in the process of the thesis elaboration.

I further declare that I have fully acknowledged the Code of Ethical Conduct of the University of Minho.

University of Minho, / 03 /2019

Full name: Abbas M.K. AL-Rjoub.

Signature:

I would like to dedicate this thesis to my loving parents

Acknowledgements

I would firstly like to thank my thesis advisor professor Luís Manuel Fernandes Rebouta from the Center of Physics at University of Minho. The door to Prof. Rebouta office was always open whenever I ran into a spot of trouble or had a question about my research or writing. He consistently allowed this research to be my own work but steered me in the right the direction whenever he thought I needed it. Words cannot describe your acknowledgements. I am also, so thankful to my co-supervisor professor Senentxu Lanceros-Mendez for his continuous support and help.

I would also like to include my thanks to professor Eduardo Jorge da Costa Alves and professor Nuno Pessoa Barradas who contributed in the Rutherford Backscattering Spectrometry (RBS) analyses, and my thanks to Pedro Costa and laboratory technicians César Costa and Adão Ferreira for their very valuable support.

I must express my very profound gratitude to my parents and to my brothers and sisters for providing me with unfailing support and continuous encouragement throughout my years of study and through the process of researching and writing this thesis. This accomplishment would not have been possible without them. Thank you.

I am very grateful to all the teaching and research staff from the MAP- fis program whom have taken some time to discuss and enrich my work.

Some special words of gratitude go to my friends who have always been a major source of support.

Finally, I acknowledge the financial support of FCT, POCI and PORL operational programs through the project POCI- 01-0145-FEDER-016907 (PTDC/CTM-ENE/2882/2014), co-financed by European community fund FEDER

Resumo

Esta tese tem como objetivo o desenvolvimento de revestimentos para absorção seletiva da radiação solar, que tenham um elevado coeficiente de absorção solar (α) (> 95%), baixa emissividade (ε) (<12% a 400 ºC), e com elevada estabilidade térmica, acima de 400 ° C ao ar e acima de 600 ºC em vácuo, de modo a que possa ser usado em sistemas de concentração da radiação solar (CSP) que utilizem temperaturas elevadas. Os revestimentos são multicamadas, que têm quatro a cinco camadas, sendo as duas primeiras, uma barreira de difusão e um refletor de radiação infravermelha, tungsténio. As restantes são constituídas por uma estrutura de dupla camada para absorção da radiação solar e uma camada antirefletora. Para a configuração das camadas de absorção, foram utilizadas três soluções diferentes. As duas primeiras soluções baseiam-se em camadas de nitreto / oxinitreto de metais de transição, nomeadamente a partir de crómio (CrAlSiNx/CrAlSiNxOy) e tungsténio (WsiAlNx/WSiAlNxOy). A terceira solução é baseada em compósitos cerâmico-metal de AlSiOx:W.

Camadas individuais das diferentes soluções foram depositadas em substratos de vidro, aço inoxidável (SS) e silício (Si) para estudar a composição química, estrutura, propriedades ópticas e mecânicas. Os espectros de transmitância e reflectância das camadas individuais, depositados em substratos de vidro, foram simulados com o software SCOUT, de modo a calcular a respetiva função dielétrica, as constantes ópticas espectrais e espessuras. As multicamadas foram desenhadas utilizando as constantes ópticas das camadas individuais, utilizando também o software SCOUT. Utilizando os resultados das simulações, as multicamadas foram depositadas em substratos de aço inoxidável utilizando a técnica de pulverização catódica por magnetrão e o desempenho dos revestimentos foi verificado por meio da sua absorção solar, da emissividade e do seu comportamento quando sujeitos a tratamentos térmicos ao ar e em vácuo. Diversas técnicas de caracterização foram utilizadas para estudar os revestimentos, nomeadamente por microscopia eletrónica de varrimento (SEM), espectrometria de retrodispersão de Rutherford (RBS), difração de raios X (DRX), espectroscopia de infravermelho com transformada de Fourier (FTIR), espectroscopia de fotoeletrões de raios-X (XPS), espectroscopia de raios-X por dispersão em energia (EDS), análise de detecção de recuo elástico por tempo de voo (TOF-ERDA), espectroscopia Raman e espectroscopia UV-VIS-NIR.

Os revestimentos multicamada apresentados nesta tese mostraram boa estabilidade térmica e resistência à oxidação após o tratamento térmico em vácuo a 600 ºC ou 580 ºC e tratamento térmico ao ar a 400 ºC ou 450 ºC. A solução baseada na estrutura WSiAlNx/WSiAlOyNx apresentou os melhores resultados, em termos de estabilidade térmica, resistência à oxidação e coeficiente de absorção solar, enquanto a baseada em CrAlSiNx/CrAlSiNxOy apresentou os valores mais baixos de emissividade à temperatura de 400 ºC. As alterações no coeficiente de absorção solar (α_{sol}) e na emissividade (ε) são insignificantes na maioria dos casos. Em alguns casos, só foram reveladas pequenas mudanças nas curvas de refletância após o primeiro passo de tratamento térmico, não aparecendo alterações nos passos subsequentes. No caso dos revestimentos baseados em CrAlSiNx / CrAlSiNxOy, após o tratamento térmico em vácuo a 600 ºC, verificou-se que ocorreu a difusão de átomos de tungsténio da camada de W para o substrato de aço inoxidável. Assim, foi introduzida uma camada de barreira de CrAlSiNx entre a camada de tungsténio e o substrato de aço e fetuado o respetivo estudo, tendo-se verificado a não ocorrência da difusão do W.

Abstract

This thesis has the objective to develop solar selective absorber coatings having simultaneously high solar absorptance (α) (>95%) and low emissivity (ε) (<12% at 400 ºC) together with high thermal stability above 400°C in air and above 600 ºC in vacuum, which could be used in the concentrated solar power (CSP) or in other high temperature applications. The coatings are multilayer stacks, that have four to five layers, being the first two, a barrier layer and a back-reflector tungsten layer. The remaining layers comprise a double film structure for phase interference finished by an antireflection layer. For the double absorption layer configuration, three different approaches have been used. The first two are based on transition metal nitride/oxynitride layers, namely from chromium as (CrAlSiNx/CrAlSiNxOy) and from tungsten as (WSiAlNx/WSiAlNxOy). Whereas, the third one is based on (AlSiOx:W) cermets.

The single layers of each approach were deposited on glass, stainless-steel (SS) and silicon (Si) substrates to study their chemical composition, structure, optical and mechanical properties. The transmittance (T) and the reflectance (R) spectra of single thin layers, deposited on glass substrates, were modelled with the help of SCOUT software and the spectral optical constants and thicknesses were calculated. The multilayer designs were performed using the optical constants of the single layers and conducted with SCOUT software. The final multilayer stacks were deposited on stainless-steel substrates using DC magnetron sputtering technique and the functionality of the absorbers optical stacks was verified through solar absorptance, emissivity and accelerated thermal ageing treatments.

All tandems and their individual layers were characterized by Scanning Electron Microscopy (SEM), Rutherford Backscattering Spectrometry (RBS), X-ray diffraction (XRD), Fourier-transform Infrared Spectroscopy (FTIR), X-Ray Photoelectron Spectroscopy (XPS), Energy Dispersive X-ray Spectroscopy (EDS), Time of flight Elastic Recoil Detection Analysis (TOF-ERDA), Raman spectroscopy and UV–VIS–IR spectroscopy.

The absorber tandems presented in this thesis showed good thermal stability and oxidation resistance after vacuum annealing at 600 ºC or 580 ºC and air annealing at 400 ºC or 450 ºC. The approach based on $WSiAlN_x/WSiAlO_yN_x$ tandem showed the best thermal stability, oxidation resistance and it has higher solar absorbance, α_{sol}, while the CrAlSiNx/ CrAlSiNxOy shows the lowest thermal emittance at the temperature (400 ºC). The variations in the solar absorptance (α_{sol}) and the thermal emittance (ε) are negligible in most cases. In some cases, small variations in the reflectance curves after the first step of annealing were observed. After the annealing in vacuum at 600 ºC, tungsten diffusion from the back-reflection layer towards the stainless-steel substrate was found in the tandem based on CrAlSiNx/ CrAlSiNxOy. Thus, a CrAlSiNx barrier layer with higher nitrogen N content was included between the stainless-steel substrate and tungsten. The influence of that barrier layer upon the W diffusion was also studied.

List of published articles

[1] A. AL-Rjoub, P. Costa, L. Rebouta, M.F. Cerqueira, P. Alpuim, N.P. Barradas, E. Alves, Characterization of magnetron sputtered sub-stoichiometric CrAlSiNx and CrAlSiOyNx coatings, Surf. Coatings Technol. 328 (2017) 134–141.

[2] A. AL-Rjoub, P. Costa, L. Rebouta, I. Bogdanovi, K. Arstila, N.P. Barradas. (in press), A study of solar thermal absorber stack based on CrAlSiNx/ CrAlSiNxOy structure by ion beams, Nucl. Inst, Methods Phys. Res. B. (2018).

[3] A. AL-Rjoub, L. Rebouta, P. Costa, N.P. Barradas, E. Alves, P.J. Ferreira, K. Abderra, A. Matilainen, K. Pischow, A design of selective solar absorber for high temperature applications, Sol. Energy. 172 (2018) 177–183.

[4] A. AL-Rjoub, L. Rebouta, P. Costa, L.G. Vieira, Multi-layer solar selective absorber coatings based on W/WSiAlNx/WSiAlOyNx /SiAlOx for high temperature applications, Sol. Energy Mater. Sol. Cells. 186 (2018) 300–308.

[5] D. Dias, L. Rebouta, P. Costa, A. AL-Rjoub, M. Benelmeki, C.J. Tavares, N.P. Barradas, E. Alves, P. Santilli, K. Pischow, Optical and structural analysis of solar selective absorbing coatings based on AlSiOx :W cermets, Sol. Energy. 150 (2017) 335–344.

[6] P. Costa, A. AL-Rjoub, L. Rebouta, N.K. Manninen, D. Alves, B. Almeida, N.P. Barradas, E. Alves, Influence of Al/Si atomic ratio on optical and electrical properties of magnetron sputtered $Al_{1-x}Si_xO_y$ coatings, Thin Solid Films. 669 (2019) 475-481.

[7] A. AL-Rjoub, L. Rebouta, P. Costa, L.G. Vieira, T.M.R. Miranda, N.P. Barradas, E. Alves, CrAlSiN barrier layer to improve the thermal stability of W/CrAlSiNx/CrAlSiOyNx /SiAlOx solar thermal absorber, Sol. Energy Mater. Sol. Cells. 191(2019) 235-242.

Contents

List of Figures

List of Tables

List of Symbols, Acronyms and Abbreviation

α_a	Coefficient of Absorption
α_{-sol}	Solar Absorptance
β	The Line Broadening
γ_C	Conduction Band
γ_V	Valence Band
δ	Phase Shift
ε	Thermal Emittance
ε_0	Permittivity of Free Space
ε_∞	Electronic Contribution to the Dielectric Constant.
ϵ_1	Real Part of the Dielectric Function
ϵ_2	Complex Part of the Dielectric Function
$\tilde{\epsilon}_{back\ ground}$	Background Term
$\tilde{\epsilon}_{Drude}$	Drude Model
$\tilde{\epsilon}_{Lorentz}$	Harmonic Lorentz Oscillators
$\tilde{\epsilon}_{OJL}$	The OJL Term
η	Efficiency of the Solar Thermal Conversion to Heat
θ	Incident Angle
ϑ	Bragg Angle
λ	Wavelength
μ	Dielectric Permeability
$\tilde{\upsilon}$	Light Frequency
ξ	Dielectric Permittivity
π	Pi = 3.14
ρ_r	Coefficient of Reflection
σ	Stefan-Boltzmann

σ_ε	Root Mean-Square (rms) of Surface Roughness
τ_t	Coefficient of Transmission
χ	Susceptibility
ω	Angular Frequency
Ω_P	Plasma Frequencies
Ω_τ	Damping Oscillator Strength
Ω_{jTO}	Frequency Damping Coefficients of the j^{th} Transversal Optical Mode
$\Omega_{\tau,\ Low}$	Damping Constant at Low Frequencies
$\Omega_{\tau,\ High}$	Damping Constant at High Frequencies
$\Omega_{\tau,\ cross\ over}$	Cross Over Frequencies at Transition Region
$\Omega_{\tau,\ Width}$	Width of the Transition Region
$\vec{B}$	Magnetic Field
c	Light Speed in Vacuum
C	Solar Concentration
d	Thickness
e	Electron Charge
$\vec{E}$	Electric Field
$E_{b\lambda}$	Emissive Power of a Black-body
E_0	Energy Gap
I	Incident Electromagnetic Radiation
I	Light Intensity
I_{abs}	Absorbed Light
I_b	Intensity of Radiation
I_0	Initial Light Intensity
I_{ref}	Reflected Light
$I_s(\lambda)$	Solar Spectral Irradiance
I_{solar}	Solar Flux Intensity

I_{tr}	Transmitted Light
J	Mean Size of the Ordered (Crystalline) Domains
k	Extinction Coefficient
k	Wave Number
m	Effective Mass of Electron
n	Number of Density Electrons
n	Refractive Index
$\vec{P}$	Polarizability
P_N	Nitrogen Partial Pressure
P_O	Oxygen Partial Pressure
P_{ON}	Oxygen and Nitrogen Partial Pressure
R_N	Reflectance at Normal Incident
R_p	Reflectance of Polished Surface
R_r	Reflectance of a Rough Surface
T	Temperature
t	Time
T_N	Transmittance at Normal Incident.
v	Light Velocity in the Medium
x	Propagation Distance
AL	Absorption Layer
AM	Air Mass
amu	Atomic Mass Unit
AR	Anti-reflection layer
CSP	Concentrated Solar Power
CT	Central Tower
DC	Direct Current
EDS	Energy Dispersive X-Ray Spectroscopy
FTIR	Fourier-Transform Infrared Spectroscopy

FWHM	Half Width the Maximum Intensity.
HA	High Absorber
IHP	Industrial Heat Process
IR	Infrared
LA	Low Absorber
NIR	Near Infrared
PD	Parabolic Dish
PT	Parabolic Trough
RBS	Rutherford Backscattering Spectroscopy
SEM	Scanning Electron Microscopy
SS	Stainless-Steel
TOF-ERDA	Time-of- Flight Elastic Recoil Detection Analysis
UV	Ultraviolet
Vis	Visible Light
XPS	X-Ray Photoelectron Spectroscopy
XRD	X-Ray Diffraction

Chapter 1

1.1 Introduction

Solar energy is one of the most available and efficient green renewable energy. The annual amount of that energy delivered into the earth is almost ten thousand times of the annual energy that human can use [8]. This huge energy can be converted into one of the three main useful energy forms: solar electricity (photovoltaic solar cells), solar fuels and solar thermal energy [9]. The solar thermal energy can be used in low, medium and high temperature applications. Non-concentrating collectors are used for low temperature applications (less than 150 ºC) [10], especially using the plate collectors with evacuated tubes for houses hot water and other industrial applications [11]. The high temperature applications, such as electricity production, need to use the concentrated solar power (CPS) [12-14] technology. So, solar thermal energy can be used for generating electricity, industrial heat process (IHP), domestic hot water and space heating, air-conditioning and refrigeration, pumping irrigation water, desalination, solar chemistry and other applications [15].

Concentrated solar power (CSP) technology uses different designs of solar systems, that can concentrate sunlight from 50 to 1500 times. The resulting energy can be subsequently used in steam turbines to produce electricity or it can be applied for other high temperature applications [16-18]. These concentrated solar powers (CSP) are divided into three main technologies [19]; parabolic trough (PT) collector [20,21], linear Fresnel reflector, parabolic dish (PD) reflector [22] and central tower (CT) [23].

However, comparing with the current energy resources, the relative cost of electricity generated by the solar thermal technology is still high. For example, CSP represented less than 2% of worldwide installed capacity of solar electricity plants in 2015 [19,24, 25]. Fortunately,

in the recent years the prices of CSP plants are fallen and made this technology more competitive with the other power plants based on fossil and nuclear fuel.

Any improvements on the optical absorber tandems should include the two important things; the thermal properties of the absorber coatings materials such that it capable to increase the operating temperature more than 450 ºC [26] and the long-term stability against corrosion, degradation, diffusion and oxidation. Improvements can be achieved by an adequate selection of used materials [27], maintaining the optical performance at higher temperatures and with higher durability. The final designs of such absorber tandems should be performed in smart way that guarantee high efficiency in terms of selectivity, high absorbance (α_{sol}) at solar radiation region (wavelength range of 0.3- 2.0 μm) and low thermal emittance in infrared (IR) region (wavelength range greater 2.0 μm). The term 'selective coating' comes from this point. In addition to good selectivity, long-term resistance against oxidation and barrier diffusion at high temperature are also needed.

The first investigations of the solar selective coating absorbers were proposed by Tabor [28], Gier and Dunkle [29] and Shaffer [30] in 1955. Then, further studies and improvements were proceeded by other scientists. Most of the current selective solar thermal absorber coatings are based on metal dielectric composite (cermet) coatings [31-34] , such as Mo- Al_2O_3 [35], Cr-Cr_2O_3 [36] yttria-stabilized zirconia (YSZ) [37], Pt-Al_2O_3 [38], ZrC- based materials [39], titanium diboride (TiB_2) [40], WTi-Al_2O_3 [41], W-Al_2O_3 [42] and AlSiOx:W [5]. With those kinds of materials, it is easier to tune the optical properties and the optical constants of the different layers, which can be done by varying the metal volume fraction of cermet layers. As a result, it is possible to optimize the optical selectivity with a high number of layers with decreasing refractive index and extinction coefficient, from substrate to surface according to the double interference theory of absorption [43]. Moreover, all these absorbers are multilayer coatings that consist of infrared IR-reflective metallic base layer such as tungsten or molybdenum, a double interference absorption (high absorber (HA) and low absorber (LA)) layers and a ceramic anti-reflection (AR) surface layer [26]. However, such coatings have limited durability at higher temperature due to oxidation or diffusion of the metal component in the dielectric matrix, which limits their applications [10]. The other group of designs are

based on layers of metal nitrides and oxynitrides structure as absorber layers, such as TiAlN/ TiAlON/ Si3N4 [44], W/AlSiN/AlSiON/AlSiOy [26], W/CrAlSiNx/CrAlSiOyNx/SiAlOx [3], Al/NbTiSiN/NbTiSiON/SiO_2 [45] and AlCrSiN/AlCrSiON/AlCrO [46]. Structures based on transition metal nitrides and oxynitrides are commonly used in the current selective solar thermal absorber stacks because of their high thermal stability, high oxidation resistance, good diffusion barrier and excellent selectivity [3,46-48].

The most used transition metals are Ti [47,49-51], Cr [2,3,46,52], W [4,16], Nb [45], Zr [53] and Al [26] or combination between them. Most of their designs show good thermal stability and oxidation resistance and share the same structure of general design as substrate (i.e. stainless-steel)\back reflector metal (i.e. W)\metal nitride\metal oxynitride\oxide layer as antireflection layer.

It is very important to emphasize again that any absorber tandem should be highly efficient in terms of selectivity, that it should have a high absorptance (α_{sol}) at solar radiation region (wavelength range of 0.3- 2.0 μm), and a low thermal emittance in infrared IR region (wavelength range dependent on temperature application, but usually greater than 2.0 μm). The low thermal emittance in IR region is a vital condition, because the efficiency decreases as the temperature increases due to the thermal radiation loss and the overlapping between the incident solar region and the re-emission thermal spectra [54]. Superior selectivity can be achieved if the multi-layer absorber tandem has a decreasing refractive index (n) and extinction coefficient (k) from substrate to surface, which can be easily achieved by appropriate choice of layers thicknesses and material composition. In the ideal case, at the front of the solar absorber, in the antireflection layer, n and k should be 1 and 0, respectively [55].

1.2 The aim of study

The main purpose of this study is to develop solar selective coatings with simultaneously high solar absorptance (α_{sol}) (higher than 95% and low emissivity (ε) (lower than 12% at 400 ºC) together with high thermal stability above 400°C in air and above 600 ºC in vacuum, such that can be used in concentrated solar power (CSP) or in other high temperature applications. In addition, deep knowledge will be gained about the multilayer structures through their solar

absorptance and emissivity measurements. Finally, the coating performance and durability will be studied after thermal annealing in air at 400 ºC or 450 ºC and in vacuum at 600 ºC.

1.3 Thesis structure

This thesis is divided in seven chapters. The first chapter introduces the concept of selective coatings and their contribution for improving solar thermal absorber tandems.

The second chapter presents the literature on review of the electromagnetic solar thermal radiation and on the optical properties of materials.

Chapter three is about the methodology for complete design of solar selective coatings. It presents a brief explanation of the simulation and experimental details used in this study. Further, the main characterization techniques and their performance functional parameters of each absorber layer are included and briefly illustrated in this chapter.

Chapter four presents the first solar selective absorber based on W/CrAlSiNx/CrAlSiOyNx/ SiAlOx. It shows the simulated, and experimental description, together with the functionality and aging characterization of the tandems. The CrAlSiN barrier layer to improve the thermal stability of the selective absorber is also presented in this chapter.

Chapter five reports on the solar selective absorber based on W/WSiAlN_x/WSiAlO_yN_x/ SiAlO_x with a similar methodology as the one followed in chapter four.

Chapter six presents a solar selective absorber coating based on AlSiOx:W cermets. Finally, the main discussion, conclusions and further work are presented in chapter seven.

Chapter 2

2.1 Electromagnetic and solar thermal radiation

"Light consists in the transverse undulations of the same medium which is the cause of electric and magnetic phenomena." (James Clerk Maxwell)

Among the most relevant investigations on the electromagnetic phenomena are the ones by the Scottish scientist James Clerk Maxwell in 1865. He proved theoretically that the electric and the magnetic fields satisfy the familiar wave equation with light propagation speed c, which supporting the fact that light is an electromagnetic phenomenon and classified to its wave frequency [56]. He gathered his work in a treatise on electricity and magnetism (1873) [57]. Electromagnetic wave is a transverse wave combined of the electric ($\vec{E}$) field oscillating perpendicular to the magnetic ($\vec{B}$) field, which propagates in space and is classified according to the frequency of its wave, as shown in Fig. 1a. As a result, light (ray) spectrum can be classified to several radiations according to its wavelength; Gamma, X-ray, Ultraviolet (UV), visible (Vis), infrared (IR), Microwave and Radio radiations. As an example, the spectrum of solar radiation is an electromagnetic radiation divided into several ranges of wavelengths according to the different criteria, as shown in Fig. 1b. The most important wavelength ranges for solar applications are UV/ Vis/ NIR (λ=0.3-2.5 μm) and thermal (λ=2.5-50 μm).

However, part of the solar radiation is absorbed or scattered by atmospheric components. The solar radiation outside the atmosphere is referred to AM 0 (average power of 1367 W/m^2) and AM 1.5 (average power of 1000 W/m^2) on the earth at a latitude of 48.2º [58], where AM stands for air mass unit (air mass is defined as the ratio of optical mass in the direct optical path to that of the vertical path [59]).

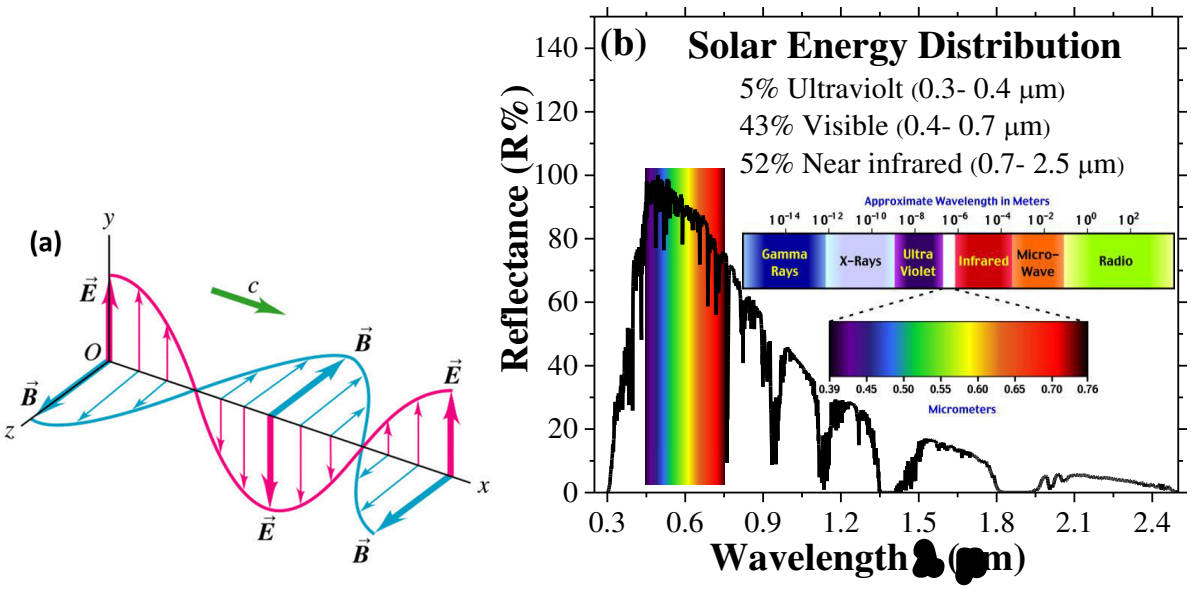

Figure 1: a) Schematic electric and magnetic fields composed an electromagnetic radiation, propagating in the x-axis. b) Solar energy distribution (AM 1.5) with classified wavelength.

As well known, any object above absolute zero temperature emits energy as electro-magnetic radiation (thermal radiation). This energy is proportional to the fourth power of the temperature of that object as completely described by Plank's law of the black-body radiation:

$$E_{b\lambda}(\lambda, T) = \frac{C_1}{\lambda^5\left(e^{(C_2/\lambda T)}-1\right)} \qquad 2.1$$

where, $E_{b\lambda}$: monochromatic emissive power of the black-body $(W/m^2\mu m)$, T is the temperature of the body in (K), λ is the wavelength (μm), $C_1 = 3.74 \times 10^8$ $(W\mu m^4/m^2)$ and $C_2 = 1.44 \times 10^4$ $(\mu m.K)$.

The black-body is an ideal physical body that absorbs all incident radiation (perfect absorber) and emits the maximum amount of energy for a given temperature. It is usually used as a reference to compare the properties of real surfaces. As shown in Fig. 2, the black-body is characterized by its thermal emission as a function of its temperature.

The wavelength corresponding to the maximum of the distribution decreases with temperature (Wien's displacement law):

$$\lambda(E_{b,max})T = 2897.8 \times 10^{-3}\mu m.K \qquad 2.2$$

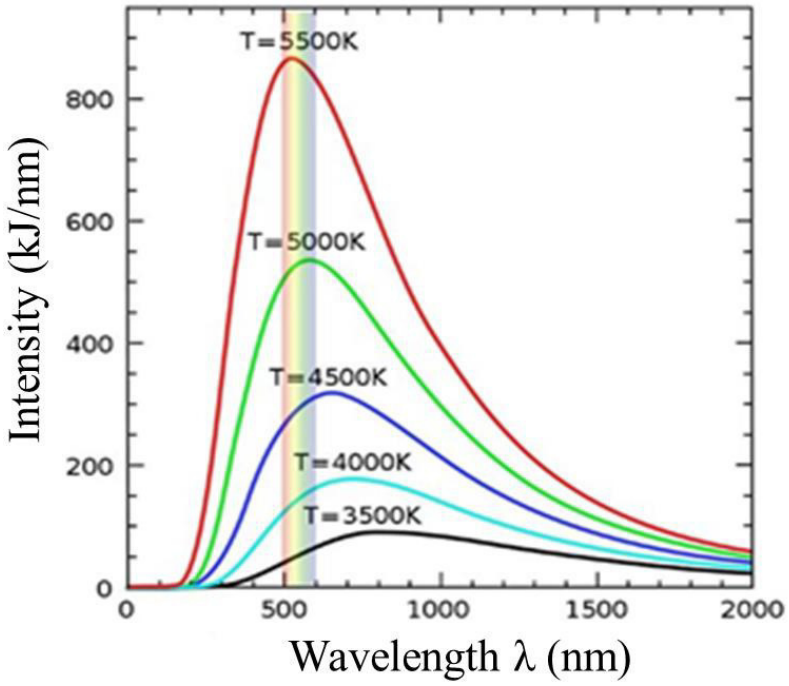

Figure 2: The radiation energy as a function of wavelength at different temperatures of a radiating black-body, per unit frequency [60].

The total emissive power $E_{b\lambda}$ of a black-body is given by (Stefan-Boltzmann law):

$$E_{b\lambda} = \int_0^\infty E_{b\lambda}(\lambda, T)d\lambda = \sigma T^4 \qquad 2.3$$

where, σ is the Stefan-Boltzmann constant, which magnitude is $5.6696 \times 10^{-8}\ W/m^2K^4$. For any real object, the emissive power E is expressed as:

$$E(T) = \varepsilon(T)\sigma T^4 \qquad 2.4$$

where $\varepsilon(T)$ is the emissivity of the object.

The black-body is a perfect diffuse emitter, such that the intensity of radiation I_b is constant in all directions:

$$E_b = \pi I_b \qquad 2.5$$

2.2 Optical properties and optical constants of materials

Matters appear differently to human eyes. For example, metals are shiny, water is colorless, milk is white and stained glass transmits some colors and absorbs others due to the light interacts with matter in different ways [61]. Depending on the type and the structure of materials, light can be reflected, absorbed, or transmitted when hitting an object as illustrated in Fig. 3.

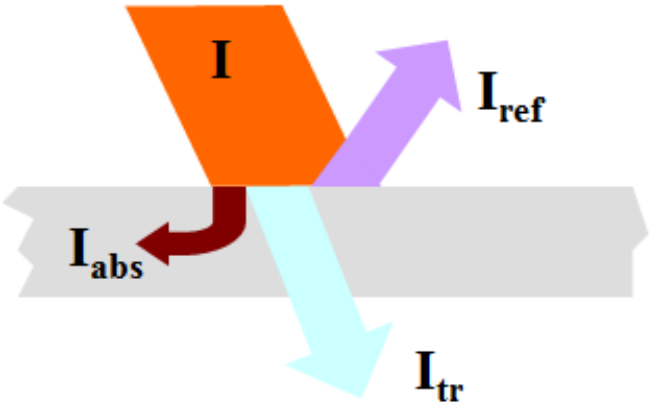

Figure 3: Schematic diagram of an incident light interacts with matter.

The incident electromagnetic radiation I is given by [62]:

$$I = I_{ref} + I_{abs} + I_{tr} \qquad 2.6$$

where, I_{ref} , I_{abs} and I_{tr} are the reflected, the absorbed and transmitted light, respectively. With $I_{ref} = \rho_r I$, $I_{abs} = \alpha_a I$ and $I_{tr} = \tau_t I$. Such that:

$$\rho_r + \alpha_a + \tau_t = 1 \qquad 2.7$$

where;

ρ_r: Reflectivity or coefficient of reflection, fraction of radiation reflected.

α_a: Absorptivity or coefficient of absorption, fraction of radiation absorbed.

τ_t: Transmissivity or coefficient of transmission, fraction of radiation transmitted.

When light hits the surface of matter, a reduction of propagate light wave velocity (c) happens and the light rays are bent at interference point described by Snell's law [63]. Thus, reflection happens at the interface between two different optical materials that have different refractive indices. The absorption of light is occurred during the propagation of light through the matter, for example, the coloration of some metals is due to the electronic interband absorption.

On the other hand, the transmitted beams are completely related to the absorption, this is simply, because of the unabsorbed beams are the transmitted one. There are other phenomena that happen when light interacts with matter, such as luminescence, scattering, polarization and diffraction [64].

As shown previously in equation (2.7), the coefficients (ρ_r, α_a, τ_t) depend on the direction and on the wavelength of the incident radiation. In the case of opaque body, such that, $\tau_t = 0$, equation (2.7) becomes $\rho_r + \alpha_a = 1$. The propagation of light through the medium is described by the complex refraction number $\tilde{n} = n + i\,k$, where the real part n determines the light velocity (v) in the medium $\left(n = \frac{c}{v}\right)$, c is the speed of the light in vacuum, and the complex part k is the extinction coefficient, which is directly related with the absorption coefficient of the medium. The electric field ($\vec{E}$) of propagated light in the absence of free charges can be derived from the Maxwell's equations as:

$$\nabla^2\vec{E} = \mu\epsilon\frac{\partial^2\vec{E}}{\partial t^2} + \mu\xi\frac{\partial\vec{E}}{\partial t} \qquad 2.8$$

The one-direction solution of equation (2.8) is given by:

$$\vec{E}(x,t) = \vec{E}_0 \exp\left(\frac{-2\pi kx}{\lambda}\right)\exp\left[i(\omega t) - \left(\frac{-2\pi nx}{\lambda}\right)\right] \qquad 2.9$$

where, μ, ϵ, ξ, k and n are dielectric permeability, dielectric permittivity, dielectric conductivity, extinction coefficient and refractive index, respectively. When the solar ray become an evanescent wave such that getting into conductive medium, then conductivity ξ is not zero ($\xi \neq 0$). According to Beer-Lambert law, the attenuation of light is directly correlated with the absorption coefficient (α) and the propagation distance x, when the light travels through a material intensity (I) given by:

$$I = I_0 e^{-\alpha x} \qquad 2.10$$

where α is the absorption coefficient and I_0 is the incident intensity of the electromagnetic wave entering the medium. Then, using the fact that the light intensity I is proportional to the square of electric field amplitude:

$$I \alpha \ |\vec{E}_0|^2 \quad 2.11$$

one can conclude:

$$\alpha = \frac{2\omega k}{c} = \frac{4\pi k}{\lambda} \quad 2.12$$

and

$$ln\left(\frac{I}{I_0}\right) = -\alpha x = -4\pi \frac{kd}{\lambda} \quad 2.13$$

where d is the thickness of the film. If the film is too thin i.e. $\lambda \gg kd$, then it becomes transparent [65-67].

The complex refraction index $\tilde{n}$ given by [61]:

$$\tilde{n}^2 = \tilde{\epsilon} \quad 2.14$$

The complex relative dielectric function $\tilde{\epsilon}_r$ describes the electrical and optical properties versus frequency, wavelength, or energy. It also describes the polarization (electric polarizability ($\vec{P}$)) and absorption properties of the material and given by:

$$\vec{P} = \varepsilon_0 \chi \vec{E}(x,t) \quad 2.15$$

with the dielectric function ($\tilde{\epsilon}_r$) and the susceptibility (χ) relation, at high frequency limit:

$$\tilde{\epsilon}_r = 1 + \chi \quad 2.16$$

The relative dielectric function ($\tilde{\epsilon}_r$) is considered as a sum of several contributions, which model intraband and interband transitions as [68,69]:

$$\tilde{\epsilon}_r = \tilde{\epsilon}_{back\ ground} + \tilde{\epsilon}_{Drude} + \sum \tilde{\epsilon}_{Lorentz} + \tilde{\epsilon}_{OJL} \quad 2.17$$

where, $\tilde{\epsilon}_{back\ ground}$: background term.

$\tilde{\epsilon}_{Drude}$: Drude model, which represents unbound electron oscillators and describes the intraband transitions of the electrons in the conduction band.

$\tilde{\epsilon}_{Lorentz}$: Harmonic Lorentz oscillators (bound charges contribution).

$\tilde{\epsilon}_{OJL}$: The OJL term follows the model proposed by O'Leary, Johnson and Lim which is used to describe the band gap transitions. The parabolic bands are assumed with tail states exponentially decaying into band gap, as will explained briefly in section 3.1 of Ch. 3.

The complex relative dielectric function $\tilde{\varepsilon}_r$ can be written as real and complex parts as $\tilde{\epsilon}_r = \epsilon_1 + \epsilon_2 i$. From the relation between the complex refractive number and complex dielectric function equation (2.14), it is possible to obtain the optical constants refractive index (n) and extinction coefficient (k) from $\epsilon_1$and ϵ_2, and vice versa as following [61]:

$$\epsilon_1 = n^2 - k^2 \text{ and } \epsilon_2 = 2nk \qquad 2.18$$

with

$$n = \left(\epsilon_1 + (\epsilon_1^2 + \epsilon_2^2)^{1/2}\right)^{1/2} \text{ and } k = \left(-\epsilon_1 + (\epsilon_1^2 + \epsilon_2^2)^{1/2}\right)^{1/2} \qquad 2.19$$

The refractive index of the absorbing layers of selective solar thermal absorbers should be an increasing function of wavelength in the wavelength range 300 –1000 nm because it contributes to the solar absorption enhancing through the interference effect. Refractive indices and thicknesses of the bilayer structure should be chosen in order to obtain destructive interference at wavelengths around 0.5 μm and 1.3 μm, contributing to the decrease of the reflectance of the solar radiation and consequently improving its absorptance. An optical path length (product of the refractive index with the thickness, *nd*) of 1/4 wavelength (in a layer) would produce a net shift of 1/2 wavelength between the light reflected from the top surface and from the bottom interface, resulting in cancellation [70]. Increasing refractive index in the wavelength range of 300 – 1000 nm allows to have a broad range with high degree of destructive interference effect. The interference effects don't occur near and above the wavelength 2.5 μm because the total optical path is not large enough. Similar behavior occurs near the wavelength of 300 nm. So, the surface absorption maximized in the range of the wavelength 500 – 2500 nm and minimized near these regions.

2.3 Theory of thin films optics

As introduced before, reflection and refraction of light occur when it travels through different media. Fig. 4a illustrates the propagation of a light beam through two media.

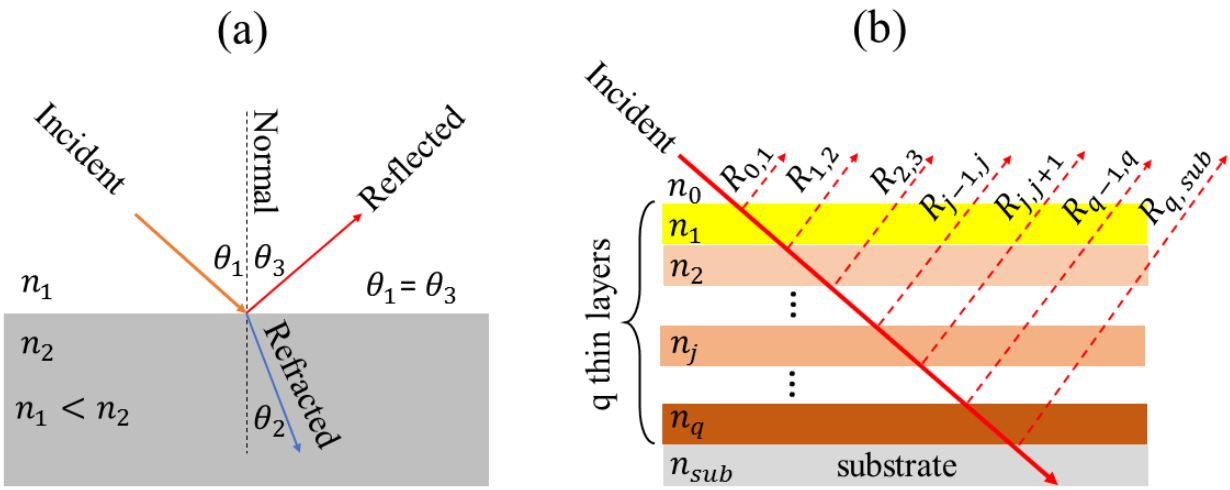

Figure 4: Schematic graph of the propagation of light beams through (a) two mediums and (b) q multi-thin layers deposited in a substrate (the reflectance vector originates from the j^{th} interface).

When two media are involved, at the interface boundaries and according to Snell's law of refraction:

$$\tilde{n}_1 sin\,\theta_1 = \tilde{n}_2 sin\,\theta_2 \qquad 2.20$$

Applying the continuity interfaces conditions of Maxwell's equations, the amplitudes of reflected (r) and transmitted (t) vectors are described by Fresnel- coefficients as [9,71-72]:

$$r_{\perp} = \frac{\tilde{n}_1 cos\,\theta_1 - \tilde{n}_2 cos\,\theta_2}{\tilde{n}_1 cos\,\theta_1 + \tilde{n}_2 cos\,\theta_2} \quad 2.21$$

$$r_{\parallel} = \frac{\tilde{n}_1 cos\,\theta_2 - \tilde{n}_2 cos\,\theta_1}{\tilde{n}_1 cos\,\theta_2 + \tilde{n}_2 cos\,\theta_1} \quad 2.22$$

$$t_{\perp} = \frac{2\tilde{n}_1 cos\,\theta_1}{\tilde{n}_1 cos\,\theta_1 + \tilde{n}_2 cos\,\theta_2} \quad 2.23$$

$$t_{\parallel} = \frac{2\tilde{n}_1 cos\,\theta_1}{\tilde{n}_1 cos\,\theta_2 + \tilde{n}_2 cos\,\theta_1} \quad 2.24$$

where, $\perp, \parallel$ are the perpendicular and the parallel to the interface vectors, respectively. For the normal light incidence $(\theta_1 = \theta_2 = \theta_3 = 0)$ the above equations can be simplified as:

$$R_N = |r_{\perp} r_{\perp}{}^*| = |r_{\parallel} r_{\parallel}{}^*| = \left|\frac{\tilde{n}_2 - \tilde{n}_1}{\tilde{n}_2 + \tilde{n}_1}\right|^2 = \frac{(\tilde{n}_2 - \tilde{n}_1)^2 + k^2}{(\tilde{n}_2 + \tilde{n}_1)^2 + k^2} \quad 2.25$$

$$T_N = |t_{\perp} t_{\perp}{}^*| = |t_{\parallel} t_{\parallel}{}^*| = \left(\frac{2\tilde{n}_1}{\tilde{n}_1 + \tilde{n}_2}\right)^2 \quad 2.26$$

where, R_N and T_N are the reflectance and the transmittance at normal incident.

These results can be generalized for q thin multilayers by using the matrix form. The term thin is very important for assumptions and calculations according to the interference theorems. So, let q be the number of thin layers as shown in Fig. 4b. Then, the total electric field of the q layers and substrate can be expressed in the matrix form as [73]:

$$\begin{pmatrix} E_0^+ \\ E_0^- \end{pmatrix} = \prod_{j=0}^{q} \boldsymbol{I_{j,j+1} L_{j+1}} \begin{pmatrix} E_{sub}^+ \\ \mathbf{0} \end{pmatrix} \quad 2.27$$

where, E_0^+ and E_0^- are the complex amplitudes of the forward and backward travelling wave, respectively, $\boldsymbol{I_{j,j+1}}$ is the scattering matrix of the interface transition from j^{th} layer to layer j+1 and $\boldsymbol{L_{j+1}}$ is the propagation matrix through the layer j+1.

The characteristic matrix of the whole system is given by [72]:

$$\begin{bmatrix} B \\ C \end{bmatrix} = \left\{ \prod_{j=1}^{q} \begin{bmatrix} cos\delta_j & (isin\delta_j)/\tilde{n}_j \\ i\tilde{n}_j sin\delta_j & cos\delta_j \end{bmatrix} \right\} \begin{bmatrix} 1 \\ \tilde{n}_{sub} \end{bmatrix} \quad 2.28$$

where $\delta = 2\pi\tilde{n}d\ cos(\theta)/\lambda$ is the phase shift of the wave traveling a distance d normal to the boundary, $\tilde{n}_j$ is the refractive index of the j[th] layer and $\tilde{n}_{sub}$ is the refractive index on the substrate. The operator matrix can be expressed as a product of operator matrices of each layer. So, eq (2.28) can rewritten as:

$$\begin{bmatrix} B \\ C \end{bmatrix} = [M_1][M_2] \dots [M_j] \dots [M_{q-1}][M_q] \begin{bmatrix} 1 \\ \tilde{n}_{sub} \end{bmatrix} \quad 2.29$$

C/B is the refractive index of the whole system (layers and substrates). The total reflectance, transmittance and absorption are given by:

$$R_N = \left(\frac{\tilde{n}_0 B - C}{\tilde{n}_0 B + C}\right)\left(\frac{\tilde{n}_0 B - C}{\tilde{n}_0 B + C}\right)^* \quad 2.30$$

$$T_N = \frac{4\tilde{n}_0\ Re(\tilde{n}_m)}{(\tilde{n}_0 B + C)(\tilde{n}_0 + BC)^*} \quad 2.31$$

$$\alpha_N = \frac{4\tilde{n}_0\ Re(BC^* - \tilde{n}_m)}{(\tilde{n}_0 B + C)(\tilde{n}_0 + BC)^*} \quad 2.32$$

The numerical calculations for the optical constants n and k governed by this system of matrices form were performed by SCOUT software, as it will be presented in chapter 3. It uses the experimental transmittance (T_{exp}) and reflectance (R_{exp}) spectra of the single layers to calculate the spectral optical constants n and k. The simulation should be good enough to minimize the error between simulated spectral transmittance T(n,k,λ) and reflectance R(n,k,λ) and their experimental measurements' $T_{exp}(\lambda)$ and $R_{exp}(\lambda)$, respectively, i.e. $\left|T(n,k,\lambda) - T_{exp}(\lambda)\right|$ and $\left|R(n,k,\lambda) - R_{exp}(\lambda)\right|$ are minimum [74]. This algorithm is exactly the backward matrix algorithm described above.

The anti-reflection layer (AR) is required for all selective solar thermal absorbers to reduce the light reflection from their surfaces and to increase its transmittance allowing light to pass through to inner layers. The reflection light beams cancellation occurs at the upper and lower

boundaries of the anti-reflection layer when they have the same beams light amplitude. Any anti-reflection layer should have a refraction index (n) that gives zero reflection and highest transmittance. Any anti-reflection layer is efficient, if its refractive index (n) is equal to the square root of the refractive index (n) of the substrate, which can be derived from the coefficient of Fresnel model and taking in the account the two conditions; the relative phase shift should be out of phase 180° (the phase difference $(\delta) = n\pi/2$), with an even integer n, and the optical thickness (nd, where d is the film thickness) should be 1/4 the beams wavelength (λ). The phase difference (δ) is given by:

$$\delta = 2\pi nd \cos(\theta/\lambda) \qquad 2.33$$

where θ is the incident light angle, which is equal to 0 in the case of normal incidence. So, the normal reflectance (R_N) is [72]:

$$R_N = \left(\frac{n_0\, n_{sub} - n_{Anti}^2}{n_0\, n_{sub} + n_{Anti}^2}\right)^2 \qquad 2.34$$

where, n_0, n_{sub} and n_{Anti} are the refractive indexes of the air, substrate (or underlying layer) and antirefrection layer (AR), respectively. To minimize the reflectance, R, eq (2.34), should be zero, implying that:

$$0 = n_0\, n_{sub} - n_{Anti}^2$$

$$\Rightarrow n_{Anti} = \sqrt{n_0\, n_{sub}} = \sqrt{n_{sub}} \qquad 2.35$$

This analysis was performed for single layer of anti-reflection later (AR), but it can be easily generalized for multi-layer cases as the case of selective thermal absorbers by using the mathematical matrix form [71,72].

2.4 Characterization of solar selective surfaces.

Solar selective surfaces are characterized by their absorptance and thermal emittance. Thus, highly efficient solar absorber surfaces must meet the two important conditions in addition of being thermally stable, as shown in Fig. 5 [27]:

- High absorptance (α_{sol}) or low reflectance ($R \approx 0$) in the visible and near infrared (IR) region (wavelength range of 0.3- 2.0 μm) at the operational temperature.
- Low thermal emittance in IR region, wavelength range greater than 2.0 μm, (high reflectance ($R \approx 1$) at $\lambda \geq 2\mu m$). Low thermal emittance in IR region is a vital condition because the efficiency decreases as the temperature increases due to the thermal radiation loss and the overlapping between the incident solar radiation wavelength range and the re-emission thermal spectra, as shown in Fig. 5.

In the ideal case, an absorber tandems should have an emittance of 1 at short wavelengths and 0 at long wavelengths and the solar absorptance should be 1 in the wavelength range of 0.3- 2.0 μm, with a sharp transition between the two regimes. The wavelength where the transition occurs is called critical or cut-off wavelength and it should be where the blackbody intensity begins to exceed the solar intensity in the wavelength between 1.8 and 3 μm depending on the operating temperature and on concentration ratio. For examples, at high temperature, the ideal transition wavelength will shift to shorter wavelengths, and at lower operating temperature, it will shift to longer wavelengths [27,31,66]. So, one way to get an efficient selective solar thermal absorber is to utilize the interference effect of thin film and optical trap to increase the absorptance and using an infrared reflector layer to reduce thermal emission [67].

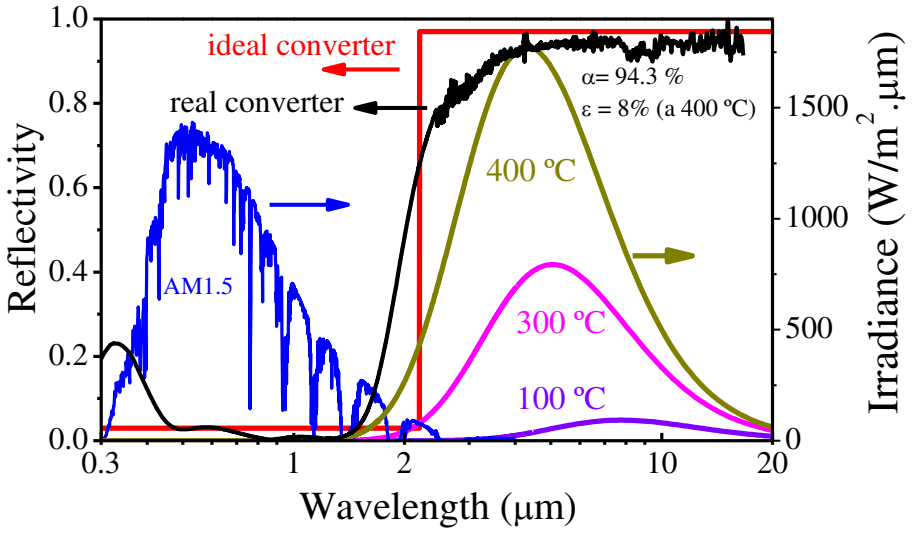

Figure 5: Spectral performance of an ideal selective solar thermal absorber.

The performance of a solar selective absorber is basically characterized by solar thermal absorption and thermal emittance. The thermal emittance (ε) is a surface property that depends on the surface conditions of the material, such as surface roughness. It is a function of the incident angle (θ) and temperature (T) and it can be calculated based on the reflectance spectrum (R) and Plank's black body radiation $E_{b\lambda}(T, \lambda)$, especially in the long wavelength (λ) region [27]. The efficiency of the solar photothermal conversion is given by:

$$\eta = \alpha_{sol} - \left(\frac{\sigma \varepsilon T^4}{C.\, I_{solar}}\right) \qquad 2.36$$

where α_{sol} is the solar absorptance, ε is the thermal emittance of the selective absorber coating at a temperature T, σ is Stefan-Boltzmann constant, C is the solar concentration ratio and I_{solar} is the solar flux intensity. The above equation shows why those conditions for selective coatings are necessary conditions, especially for higher operating temperature.

Usually, the solar reflectance is measured at near-normal angle of incidence (θ=0) in the wavelength range 0.3-2.5 μm [27]. The normal solar absorptance (α_{sol}) is the ratio of the total absorbed solar radiation to the incident radiation and it is determined from the calculated or the experimental spectral reflectance data $R(\lambda)$ and ASTM AM1.5D solar spectral irradiance, $I_s(\lambda)$, at the wavelength range of 0.3 – 2.5 μm by:

$$\alpha_{sol} = \frac{\int_{0.3\mu m}^{2.5\mu m} I_s(\lambda)[1-R(\lambda)]\, d\lambda}{\int_{0.3\mu m}^{2.5\mu m} I_s(\lambda)\, d\lambda} \qquad 2.37$$

According to the Kirchoff's law of thermal radiation, for an arbitrary body emitting and absorbing thermal radiation in thermodynamic equilibrium, the emissivity is equal to the absorptivity [75].

$$\text{Emissivity } (\varepsilon) = \text{Absorptivity } (\alpha) \qquad 2.38$$

In the case of opaque materials, the transmittance is zero and eq (2.37) can be rewritten as:

$$\varepsilon(\lambda, \mathrm{T}) = \alpha(\lambda, \theta) = 1 - \mathrm{R}(\lambda, \theta) \qquad 2.39$$

where $R(\lambda, \theta)$ is the spectral reflectance of incident radiation at the incident angle of light (θ) and T is the given temperature.

The emissivity of a surface depends on the surface temperature (T), wavelength (λ) and direction. It is defined at specific temperature(T) as [61]

$$\text{Emissivity } (\varepsilon) = \frac{\text{Surface total emissive power (E)}}{\text{Blackbody total emissive power } (E_b)} \qquad 2.40$$

with total or hemispherical emissivity given by [76]:

$$\varepsilon_b = \frac{E(T)}{E_b(T)} = \frac{\int_0^{\infty} \varepsilon_\lambda(T_0) E_{b\lambda} d\lambda}{\sigma T^4}$$

$$= \frac{\int_{1.6\mu m}^{25\mu m} E_{b\lambda}(\mathrm{T},\lambda)[1-R(\lambda,T)]\, d\lambda}{\int_{1.6\mu m}^{25\mu m} E_{b\lambda}(T,\lambda)\, d\lambda} \qquad 2.41$$

where $E_{b\lambda}(T, \lambda)$ is the temperature dependent spectral blackbody emissive power and $R(\lambda, T)$ is the spectral reflectance measured in the wavelength range of 1.6 – 25 μm. The maximum usage of high temperature occurs when the thermal emission of the absorbed surface is low because of the thermal losses by emission increase proportionally by the fourth power of temperature. The emittance also depends on the roughness of the substrate in case of multi-layer selective coatings, which govern the reflectance as [50,77]:

$$R_r = R_p exp\left(-\frac{4\pi\sigma_\varepsilon}{\lambda}\right)^2 \qquad 2.42$$

where R_r, R_p and σ_ε are the reflectance of a rough surface, the reflectance of a polished surface and the root mean-square (rms) of the surface roughness, respectively.

2.5 Spectral selective coating surfaces for solar thermal absorption.

The different designs of all selective solar absorbers have been developed are classified to six types: intrinsic, semiconductor-metal tandems, multilayer absorbers, multi-dielectric composite coatings, textured surfaces, and selectively solar-transmitting coating on a black body like-absorber [27], as shown schematically in Fig. 6.

a) **Intrinsic absorbers (Mass absorbers):** one of the straight forward ways of selective coating production, intrinsic absorbers consist of materials with intrinsic properties formed in the wanted spectral selectivity (absorptive in the solar spectrum and reflective in the far-infrared region). These absorbers are structurally stable but with lower efficiency when compared with other types and can be metallic such as tungsten W [78], or as Si doped with B, CaF_2, ZrB_2 and HfC [78,79].

   Intrinsic absorber materials are not ideal for solar applications and the materials need special re-structure, which justify why such kinds of absorbers have not been very productive.

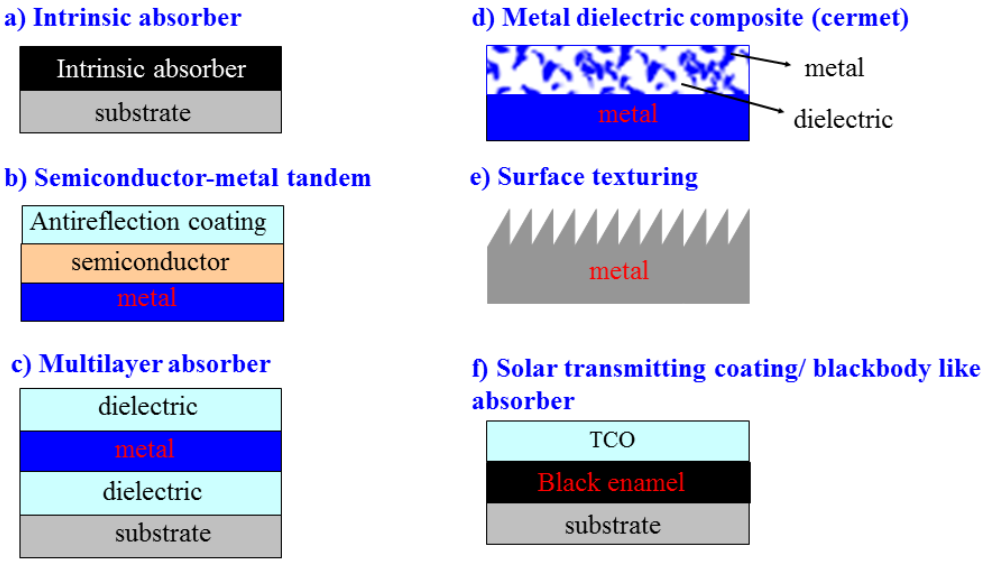

Figure 6: Schematic designs of the six types of coating and surfaces for the solar selective absorbers.

b) **Semiconductor-metal tandems:** due to the band gap (0.5 – 1.26) eV of these kind of materials, they can absorb light with short wavelength and most of semiconductor- metal tandems show low emittance due to the metal layers of those designs. So, they are mainly consisted of underlying metal layer, designed to reduce the thermal emission from heated substrates and semiconductors with forbidden band gaps about 0.4–1.5 eV. The most common used semiconductors are silicon Si (1.1 eV), germanium Ge (0.7 eV) and lead sulphilde PbS (0.4 eV) [78]. To reduce the reflectance losses of the high refractive indices in the semiconductors absorber layers, an anti-reflection layer should be included [67].

c) **Multilayer absorbers:** consist on several reflection layers that manage to absorb light with high efficiency. Usually, multilayer absorbers have high solar absorption, low thermal emittance and depending of the used materials, can have good thermal stability at high temperatures. The metals (e.g. Cr, W, Ti, Mo, Ag, Cu, Ni) are sandwiched between the dielectric layers such as Al_2O_3

d) **Metal-dielectric composite coating (Cermets):** Cermets-based absorbers are the most common solutions used for high temperature applications, they consist of

metal particles embedded in a dielectric or ceramic material (matrix). The cermet layer is transparent in the thermal IR region and strongly absorbs in the solar region. This is because of the inter-band transition in the metal and the resonance of the small particles of cermet due to the plasmonic effect. The solar selectivity of these kinds of absorbers can be adjusted by choosing a proper coating thickness, particles concentration, size, orientations and shape. It can be measured by the response of the absorbing particles [80]. The role of the metallic particles of cermet is to:

- Increase the solar absorption, due to the interband transitions in the metal.
- Reduce the absorption in the IR- region due to the small particle size.
- Reduce the rate of oxidation; because of the ceramic matrix.

e) **Textured surfaces:** they may be used for high solar absorbance by multiple reflection among needle-like dendritic or porous micro-structure [78,81]. The textured surfaces are rough, absorb the solar energy and work like a highly reflective mirror in the IR region, and the emittance of such tandems can be controlled by modifying the microstructure of coatings.

f) **Solar transmitting coating/blackbody-like absorber:** a highly doped semi-conductor, such as SnO_2:F, SnO_2:Sb, In_2SO_3:Sn, and ZnO:Al, that can be used for low-temperature flat-plate collectors [27].

There are two main groups of spectrally selective solar thermal absorber coatings for high temperature applications > 400 ºC. The first, is a multilayer structure based on transition metal nitrides and oxynitrides. The most suitable transition metals candidates are: Ti [50,82-84], Cr [3,85,86], Nb [45,87],W [4,88], Al [26], Zr [89,90], Mo [87]. They have a core role in such designs because they have an ideal forbidden bandwidth and after doping with oxygen and nitrogen, they become an excellent absorbing materials [67], in addition to their high thermal stability, high oxidation resistance, good diffusion barrier and excellent selectivity. Most of these absorbers show a good selectivity and an excellent thermal stability after annealing in air or vacuum.

The second group of the available tandems in the market are the cermets-based spectrally selective solar absorbers. These absorbers are being used in the concentrated solar power (CSP) technology for electricity generation. Cermets-based absorbers mainly consists of fine metal

particles and dielectric matrix. The most used dielectric matrix are Al_2O_3 [41,91], $SiAlO_x$ [5], Si_3N_4 [92], AlN [93], MgO [94], MgF_2 [95], TiC [96], CrON [97] and HfO_x[98]. All absorbers of this group are formed by a multilayer consisting in a IR-reflective metallic base layer such as tungsten or molybdenum, a double interference absorption structure layers (high absorber (HA) and low absorber (LA) layers) and a ceramic anti-reflection (AR) surface layer [26]. With this selection of materials, it is easy to tune the optical properties and the optical constants of the different layers by varying the metal volume fraction of ceramic layers and optimizing the absorptance according to the double interference theory of absorption [99]. However, such coatings have limited durability at higher temperature due to oxidation or diffusion of the metal component in the dielectric matrix, which limit their applications at those high temperatures [10].

However, most of the available designs about the two kind of optical stacks suffer from poor thermal stability and from elemental diffusion between their layers, when subjected to high temperatures. For example, Coa et al. reported the diffusion of iron atoms from the stainless-steel into the cermet layer forming a $FeWO_4$ phase [100]. Zhang et al. clearly observed the elemental diffusion of Cr, N and O between the absorbing layer and Al substrate and some microstructure defects appeared [101]. This occurred in a sub-stoichiometric amorphous chromium nitride deposited on an aluminium substrate. Liang et al. confirmed the existence of the element diffusion close to the interface region, in interfaces SiO_2/CrO_x and CrO_x/CrN_x, and copper elemental diffusion from substrate throughout all the stacked layers [102]. Kotilainen et al. studied the influence of temperature-induced copper diffusion on the degradation of selective chromium oxynitride solar absorber coating. They recorded a diffusion of copper from the substrate into the coating and through the coating to the surface [103]. Wang et al. claimed that they improved the thermal stability of W-Al_2O_3 by adding Ti nano-particles as WTi -Al_2O_3, which revealed that the surface segregation of solute Ti atoms from the parent alloyed nano-particles and their partial oxidation to form protective layer restrain outward diffusion of W element [41].

Also, in most studies reported in the literature, there is a small change in the reflectance curve of the stacks after the first step of annealing in air or vacuum, but for further steps of

annealing, it looks more stable. Despite extensive studies on the design and the structure of thermal solar absorber tandems, oxidation resistance and the diffusion process are still difficult to understand.

This thesis presents and discusses three kinds of designs of solar thermal absorbers. The first two are based on nitrides and oxynitrides with structures ($W/CrAlSiN_x/CrAlSiO_yN_x/SiAlO_x$) [1-3] and $W/WSiAlN_x/WSiAlO_yN_x/SiAlO_x$ for high temperature applications [4]. While, the third is coatings based on $AlSiO_x$:W cermets [5].

Chapter 3 Methodology for the design of solar selective absorbing coatings

3.1 Simulation

All designs presented in this research were previously simulated with the help of SCOUT software [104] creating a multilayer model based on transmittance and reflectance spectra of individual thin layers deposited on glass substrates. SCOUT is a windows software developed for the analysis of optical spectra by computer simulation based on well-known physical optical models and adjustments of the model parameters to fit the measured data, resulting a realistic simulation of optical spectra.

Dielectric function or its square root, the complex refractive index (spectral optical constants) of materials are the key parameters to extract microscopic quantities from optical spectroscopy, such as the resonance frequencies of the oscillating atoms, the impurity concentrations or the thin film thicknesses from macroscopic experiments. Using the experimental transmittance (T) and reflectance (R) of thin film layers deposited on glass substrate [74], SCOUT allows to perform a standard spectrum simulation employing the Fresnel equations together with appropriate models for the frequency dependent of relative complex dielectric function ($\tilde{\varepsilon}_r = \varepsilon_1 + i\varepsilon_2$), considering the sum of several contributions of frequencies as shown previously in equation (2.17) [61,105]. All those models use causal quantities to describe the dielectric function, including the OJL model (proposed by O'Leary, Johnson and Lim) that is specifically modified in the SCOUT software to ensure the Kramers-Kronig compatibility between the real and imaginary parts of the dielectric function.

The used harmonic Lorentz oscillators model describes the microscopic vibrations involving the motion of the atomic nuclei that usually have their resonance frequencies in the infrared region. Their frequencies depend on the oscillating masses and the strength of the bonding. So, it can be used for material identification, as an example, silicon important impurities like carbon and oxygen can be identified by their characteristic vibrational modes

and their susceptibilities (χ) describing microscopic vibrations can be modeled by harmonic oscillator terms [61,104]:

$$\chi_{Harmonic\ oscillator} = \frac{\Omega_P^2}{\Omega^2 - \tilde{\nu}^2 - i\tilde{\nu}\Omega_\tau} \qquad 3.1$$

where, $\tilde{\nu}, \Omega_\tau$, Ω and Ω_P are the light frequency, the damping oscillator strength, the resonance position and the plasma frequencies, respectively. Ω_P is given by $\Omega_P^2 = \frac{n^2 e}{\varepsilon_0 m}$, where ε_0, e, m, n are the permittivity of free space, the electron charge, the effective mass of electron and the number of density electrons, respectively.

The Drude model of electrical conduction was proposed in 1897 [106], it describes the free carriers contribution (e.g. doped semiconductors) and it is mostly used to explain the transparency of the metallic thin films as a simple expression of the susceptibility (χ) of free carriers as:

$$\chi_{Drude}(\tilde{\nu}) = -\frac{\Omega_P^2}{\tilde{\nu}^2 + i\tilde{\nu}\Omega_\tau} \qquad 3.2$$

With SCOUT it is also possible to use the extended Drude model for situations where the damping of free carriers exhibits a characteristic dependence on frequency [61,104,107].

The OJL model for interband transitions describes the optical transition from the valence band to the conduction band and was proposed by O'Leary and al. in 1997 [105] to model the band gap transitions of amorphous silicon. It is an elementary empirical model for the distribution of electronic states of an amorphous semiconductor, that determines the functional form of the optical absorption spectrum, in particular the joint density of states function. It has four parameters: the band gap, the decay energy to describe an exponential tail extending into the band gap and two amplitudes [104,105] as shown in Fig. 7.

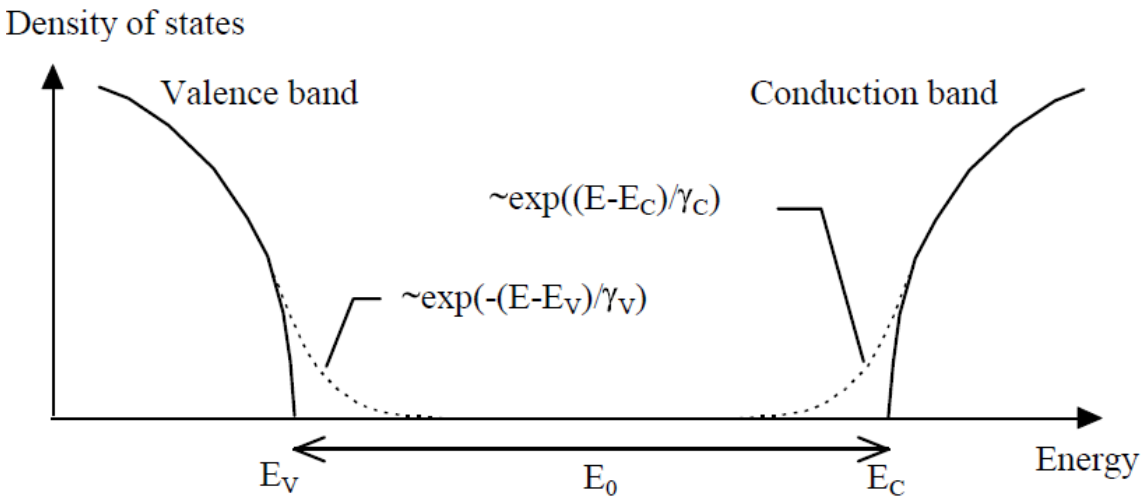

Figure 7: Conduction (γ_C) and valence (γ_V) bands of OJL model as a function of energy [104].

Our layers are amorphous, and this model yield a good fit. The simulation methodology used in this research for building of the multilayer solar selective absorber stacks is summarized in Fig. 8, the starting point is building up a model and performing the theoretical analysis of experimental spectra of transmittance (T) and reflectance (R) of individual thin films deposited on glass substrates. Then, obtaining the optical constants, thicknesses and deposition rates of each films. Finally, using the models of individual layers, the final stacks for any solar selective absorber can be optimized by the addition of adequate layers and the effect of each layer can be briefly studied to improve the final design.

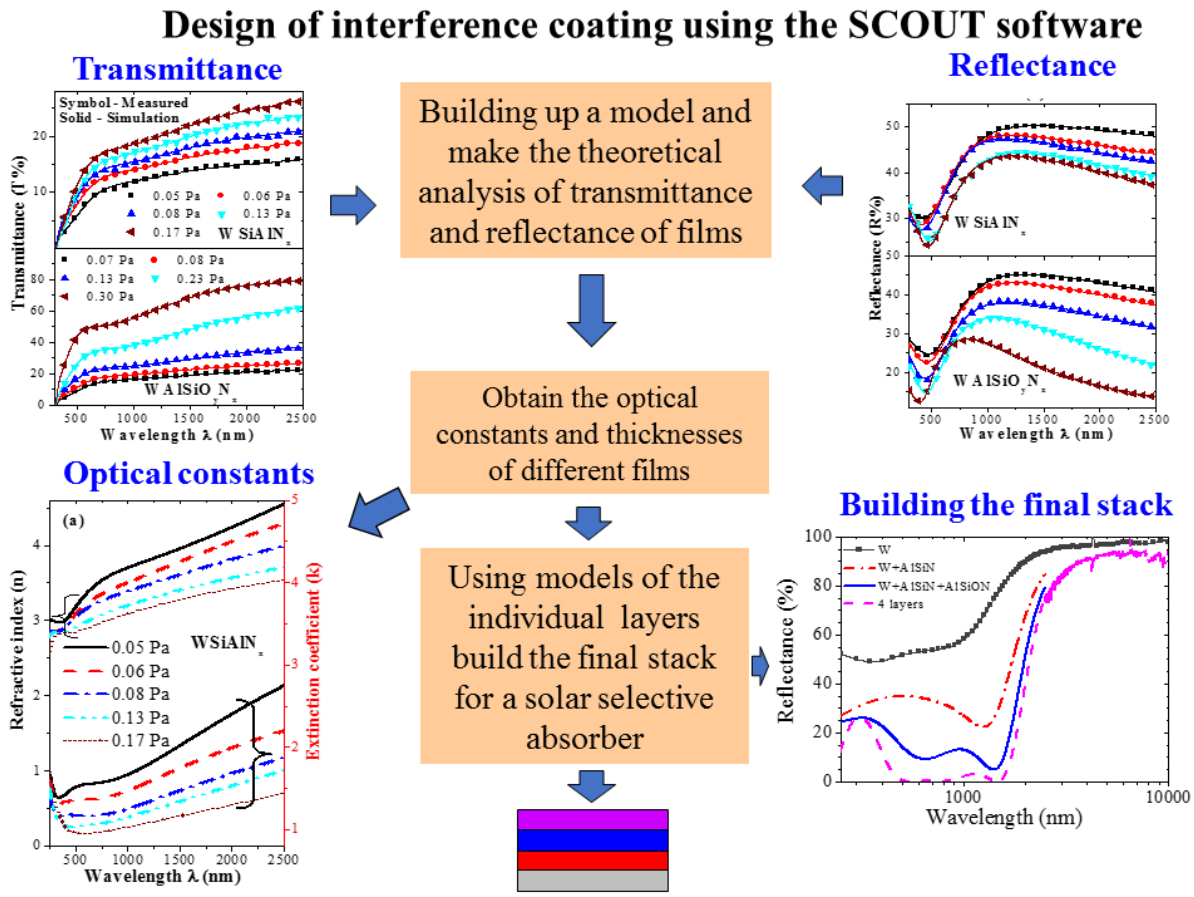

Figure 8: Schematic diagram of the methodology of the simulation of multilayer optical stacks as obtained by SCOUT.

3.2 Materials and Methods

In this section, materials and all experimental preparation and characterizations conditions are presented.

3.2.1 Deposition method

All films were deposited by the DC magnetron sputtering method. Fig. 9 shows the chamber used for coatings deposition. It is equipped with a vacuum pumping system allowing to reach a base pressure of 2×10^{-4} Pa, a closed water cooling system, several lines of reactive gases (N_2, O_2, and a mixture of N_2/O_2 (85/15%)) and working gases (Ar and He), two sputtering magnetrons, several power sources and bias source connected to the substrate holder, that can work in static or rotation mode. The chamber walls are rolled with high resistance material that can heat it during vacuuming to improve the degassing process. The main door is supported with manual hydraulic system to open and close the chamber.

Figure 9: The used DC sputtering chamber for coatings deposition.

For the first two solar selective absorber tandems presented in this work, the depositions were performed using a substrate holder placed 9 cm above the target and working in static mode. All layers were deposited in similar conditions by DC magnetron sputtering (P_{Ar}=0.37 Pa, current density 6.4 mA/cm^2, pulsed bias of -60 V, f =90 kHz, room temperature and base

pressure 2×10^{-4} Pa), except in tungsten layer case, in which the current density was 12.7 mA/cm^2. The different layers were deposited varying the partial pressures of reactive gases, in order to obtain films with different optical properties.

All back-reflector tungsten layers were deposited using a tungsten target (99.99%) with a diameter of 10 cm. Then, for $WSiAlN_x$ and $WSiAlO_yN_x$ layers, the same target was used, by adding 9 silicon pellets with a diameter of 10 mm and 9 squares of aluminium pieces with 1 cm × 1 cm on the target erosion zone. For the deposition of $CrAlSiN_x$ and $CrAlSiN_xO_y$ layers, a 10 cm diameter target of Cr70 Al30 at% was used with 9 silicon pellets with a diameter of 10 mm on the target erosion zone. For the $SiAlO_x$ antireflection oxide layer, a Si80 Al20 at% target was used, with oxygen as a reactive gas (P_O= 0.06 Pa), as shown in Fig. 10.

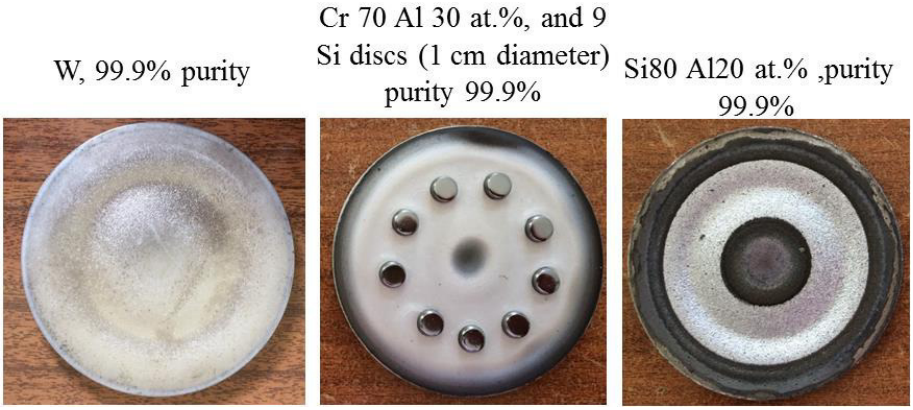

Figure 10: Some targets used in the coatings.

The $AlSiO_x$:W cermets coatings were deposited by simultaneous sputtering from pure metal W and Al targets, the latter with 9 small silicon disc pellets (1 cm in diameter) distributed uniformly on the erosion zone. The 10 cm in diameter circular targets were placed horizontally, while the substrate holder rotated with a constant speed over them. The $AlSiO_x$:W cermet films with varying W volume fraction were obtained by maintaining constant the sputter current for the $AlSi_x$ target (6.4 mA/cm^2) and O_2 flow (5 sccm) and varying the current of the W target from 0.15 A to 0.75 A (from 1.9 mA/cm^2 to 9.6 mA/cm^2). Two series were prepared using different substrate holder rotation speeds, 7 and 15 rpm. The same Al target with the 9 small silicon disc pellets was used to deposit the anti-reflection oxide layer of this stack, as will see in Ch. 6.

Three types of substrates were used in this work:

- Polished stainless-steel (AISI304) substrates

Stainless-steel is a based iron alloys containing at least 10.5% chromium and other metals with different percentage. Alloy AISI304 is a general purpose austenitic stainless-steel with a face centred cubic structure. It has a lower carbon content, which improve their corrosion resistance in welded structures. These substrates were selected to support high temperatures annealing ~ 600 ºC. Stainless-steel substrates have the drawback of a relatively high emissivity. So, it is necessary to use a metallic tungsten layer, which has good oxidation resistance and high electrical conductivity to minimize the emissivity.

- Si (100) wafer substrates.

Single side polished silicon wafers, with crystal orientation <100>, were used for the study of some physical properties including grain size, morphology, surface texture and crystallinity. Also, they were used in the identification of chemical composition and chemical bonding of some samples.

- Glass substrates.

Microscope slides ISO 8037 76 x 26 mm and thickness of 1 mm, corners 45° glass substrates were used in the optical spectroscopy to measure the transmittance (T) and the reflectance (R) of the individual thin layers.

The silicon and stainless-steel substrates were always ultra sound cleaned in acetone for 15 - 20 minutes, and ion etched prior the deposition, while, the glass substrates were always cleaned with alcohol.

3.2.2 Thermal treatments

For testing the thermal stabilities and oxidation resistance of the final absorber stacks, the optical stacks deposited on stainless-steel substrates were subjected to annealing tests in air at 400 ºC or 450 ºC and in vacuum at 600 ºC or 580 ºC for different periods of time (usually more than 200 h divided into several steps). In the case of vacuum annealing, the furnace was

evacuated to the base pressure of 5.0 mPa and annealing was performed for many steps, after each step, the vacuum was broken, and the reflectance was measured to evaluate the absorptance and the emissivity. The used furnaces (vacuum and air) are shown in Fig. 11.

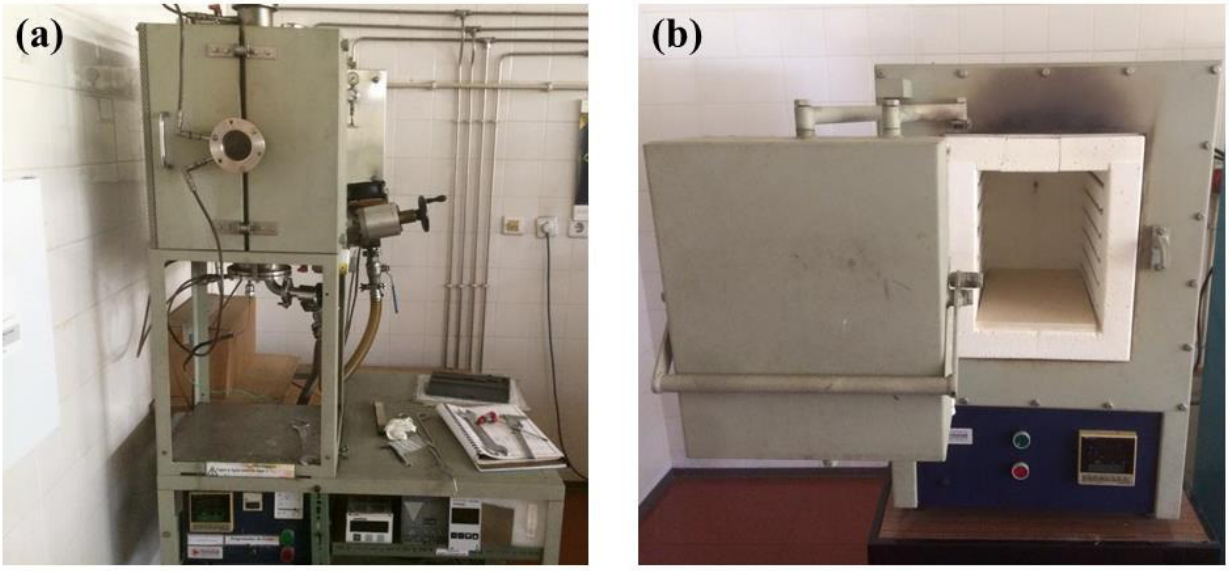

Figure 11: The furnaces (a) vacuum and (b) air used in annealing.

3.3 Characterization techniques

In most cases, the individual and the final multilayer coatings were characterized by UV–VIS–NIR spectroscopy, Scanning Electron Microscopy (SEM), Energy Dispersive X-ray Spectroscopy (EDS), Rutherford Backscattering Spectrometry (RBS), Nanoindentation, X-ray diffraction (XRD), X-Ray Photoelectron Spectroscopy (XPS), Raman Spectroscopy, Time-of-flight Elastic Recoil Detection Analysis (TOF-ERDA) and Fourier-transform Infrared Spectroscopy (FTIR). In the following subsections are presented a brief experimental description and performance parameters for each one.

3.3.1 UV–VIS–NIR spectroscopy

The transmittance (T) and the reflectance (R) of individual thin layers of W, $CrAlSiN_x$, $CrAlSiN_xO_y$, $WSiAlN_x$, $WSiAlO_yN_x$, $AlSiO_x$:W and $SiAlO_x$, deposited on glass substrates were measured by using a Shimadzu PC3100 spectrophotometer shown in Fig. 12, in the wavelength range of 0.25 – 2.5 μm with a scan step of 1 nm. The equipment is supported with an integrating sphere for reflectance measurements. The reflectance data were obtained at quasi-normal incidence (angle of incidence of 8º) using an Al mirror as reference, and the reflectance of final stacks deposited in stainless-steel substrates was also measured in the same procedure to evaluate the solar thermal absorbance (α_{sol}).

Figure 12: The Shimadzu PC3100 spectrophotometer used for transmittance (T) and the reflectance (R).

To calculate the normal thermal emittance (ε_{th}), the infrared specular reflectance spectra were measured in the wavelength range of 2–25 μm (wavenumber range 5000 – 400 cm^{-1}) at near normal incidence (angle of incidence $\alpha \approx 11º$) with a Fourier Transform Infrared spectrometer Bruker IFS 66V equipped with a globar source, a KBr beam-splitter and a DTGS detector. The measurements were performed in vacuum at room temperature and the spectra were recorded at 4 cm^{-1} resolution with 16 scans. Before the sample measurement, a background reference was performed with an aluminium mirror placed at the same position as the sample.

Because of the used measurement configuration doesn't allow to measure the absolute reflectance, the original spectra are slightly overestimated (the reference Al mirror reflects less than 100%). The procedure to correct the data was to measure the reflectance of polished copper in the same conditions and determine the multiplying factor that gives room temperature emittance of 3%. Then, all spectra were corrected by using the same multiplying constant. The emittance was also measured (at 80 ºC) with an emissometer AE-AD3, from Devices & Service Company to compare the two methods of measurements at 80 ºC.

3.3.2 Scanning Electron Microscopy and Energy Dispersive X-ray Spectroscopy

The microscope shown in Fig. 13 was used for all Scanning Electron Microscopy (SEM) analysis for W, $CrAlSiN_x$, $CrAlSiN_xO_y$, $WSiAlN_x$, $WSiAlO_yN_x$, $AlSiO_x$:W, $SiAlO_x$ and $AlSiO_x$ and their corresponding multi-layers. It allows to analyze conductive, semi-conductive and non-conductive samples including any type of polymer, metal, ceramic or organic material, and has an ultra-high resolution (<1.8 nm both at high and low vacuum) and particularly developed to characterize nanomaterials, such as: diamond coatings, thin films, carbon nanotubes, nanoparticles, semiconductors, polymers, porous materials, glass substrates, organic materials or others. The detectors of the microscope are: Through-lens (TLD) (high vacuum) (SE and BSE mode), Everhardt Thornley (ETD) (high vacuum) (SE and BSE mode), Low Vacuum (LVD) (SE and BSE mode), Backscattered Electron Detector (BSED) (high vacuum) (BSE mode). Scanning transmitted electron microscopy (STEM) (transmitted electrons mode) and Infrared CCD camera (CCD) (high and low vacuum) (light mode and infrared) with 284 mm diameter chamber.

The Nova NanoSEM 200 possess unique ultra-high-resolution characterization capabilities in low vacuum, an environment that suppresses the charge on non-conducting materials or components and cancels self-contamination of the sample or contamination induced by the electron beam. In our analysis it is used to determine the coatings thickness and morphology.

Figure 13: The Scanning Electron Microscope [108].

The microscope is integrated with Energy Dispersive X-ray Spectroscopy (EDS) and with electron backscatter diffraction pattern detection and analysis system (EBSD). In this work, the EDS was used to performed on randomly selected regions of samples surface with an acceleration voltage of ranged between 7-10 keV. By X-ray, it was able to obtain profiles maps of elements and perform sequence analysis of particles and regions in a sample.

3.3.3 Rutherford Backscattering Spectrometry

Rutherford Backscattering Spectrometry (RBS) was used to study the chemical composition of single layers and, in some cases, to study the thermal stability of the optical stacks, such as the diffusion of Cr and W after annealing in air and vacuum for first optical stack, or to study the diffusion of the W nanoparticles from inner absorption layers towards the anti-reflection layer in the third optical stack. The measurements were carried out at the CTN/IST Van de Graaff accelerator with detectors placed at 165º or 140º to the beam direction depending on the samples conditions, the Van de Graaff accelerator is shown in Fig. 14. Spectra were collected with a 2 MeV $^{4}He^{+}$ beam. Normal incidence was used in the experiments and the obtained data were analyzed with the IBA Data Furnace [109].

Figure 14: A 2,5 MV Van de Graaff accelerator with three experimental beam lines, with all the relevant ion beam techniques available: RBS, PIXE, NRA, Channelling, ERDA and NRB [110].

The collected data were fitted with the help of NDF Software, which is a DOS code dedicated to the analysis of RBS, ERDA, PIXE, non-resonant NRA and NDP data for any ion, any target, any geometry, and number of spectra [111].

3.3.4 X-Ray Diffraction

The crystalline structure of all absorbers coating and all their corresponding individual layers were studied using the X-ray diffraction (XRD) employing a Bruker AXS Discover D8, operating with $Cu_{K\alpha}$ radiation shown in Fig. 15. With this equipment, several types of analysis can be performed with high equality, such as, the high-resolution conventional X-ray diffraction of bulk (powder or thin film samples), phase analysis, environmental diffractometry, from -190 ºC to 1200 ºC, grazing incidence (GIXD) and residual stresses evaluation (sin (2ψ)) and reflectometry.

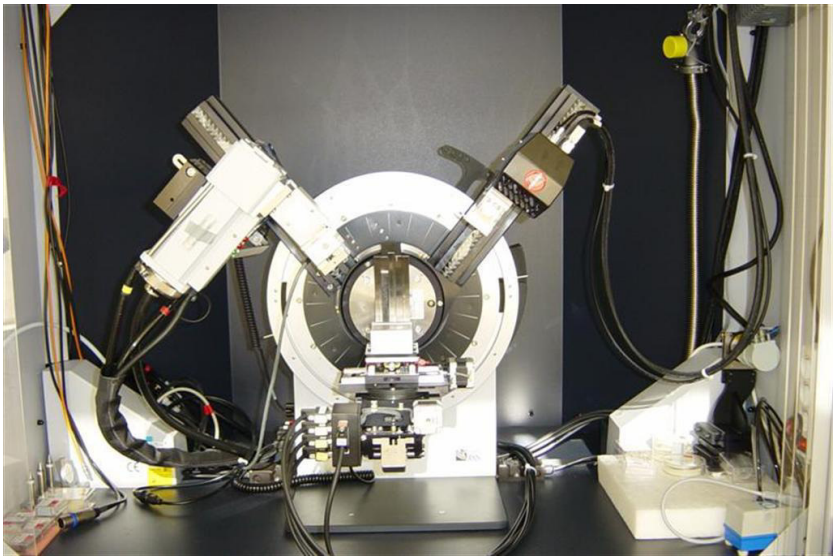

Figure 15: High angles diffraction system and high-resolution reflectometry [108].

For each optical stack, three samples were used to study structural stability, namely as-deposited, after vacuum and air annealing were analyzed by using a 3º incidence angle. The grain size of our samples was evaluated using the width of their peaks and the Scherrer equation [112]:

$$\Gamma = \frac{J\lambda}{\beta \cos\vartheta} \qquad 3.3$$

where, Γ is the mean size of the ordered (crystalline) domains, J is the mean size of the ordered (crystalline) domains, which may be smaller or equal to the grain size, β is the line broadening at half the maximum intensity (FWHM), ϑ is the Bragg angle and λ is the X-ray wavelength.

3.3.5 X-ray Photoelectron Spectroscopy

The chemical bonding state of single layers of $CrAlSiN_x$, $CrAlSiO_yN_x$, WSiAlNx, WSiAlOyNx, $AlSiO_x$:W and $SiAlO_x$ deposited with same parameters as those used in multilayer stacks was evaluated using X-ray Photoelectron Spectroscopy (XPS) analysis. Also, it was used to study the thermal stability of the third optical stacks. The XPS measurements were carried out using a Kratos AXIS Ultra HAS X-ray Photoelectron Spectroscopy system from Centro de Materiais da Universidade do Porto (CEMUP), shown in Fig. 16, using an Al K_α (1486.7 eV) X-ray source, with a 40 eV pass energy.

Figure 16: System of analysis of surfaces by electron spectroscopy: XPS (Kratos Axis Ultra HAS) [113].

The C1s line at 285.0 eV was used to calibrate the binding energies and the XPS spectra were analyzed in CasaXPS software, with all peaks were fitted using a Shirley background and GL (30) line shape, where GL (p): Gaussian/Lorentzian product formula where the mixing is determined by m = p/100, GL (100) is a pure Lorentzian whereas GL (0) is pure Gaussian [114].

3.3.6 Time-of- Flight Elastic Recoil Detection Analysis

Atomic composition and depth profiles of all elements present in Cr based optical stack samples were determined using Time-of- Flight Elastic Recoil Detection Analysis (TOF-ERDA). The measurements were performed using a 6 MV Tandem Van de Graaff accelerator located at Ruđer Bošković Institute, in Croatia, shown in Fig. 17. TOF-ERDA is a spectroscopic technique for elemental concentrations and their depth profiles measurements in unknown samples up to the 400 nm depths. Using ionic heavy beam (e.g. Cl, I or Au) with energies of 0.5 MeV/A to recoil atomic nuclei from the target surface layers in forward directions. Energy and time of flight of the recoiled nuclei are measured in coincidence,

enabling separation of all elements by energy and mass. Then, the time-energy spectra are converted to depth profiles.

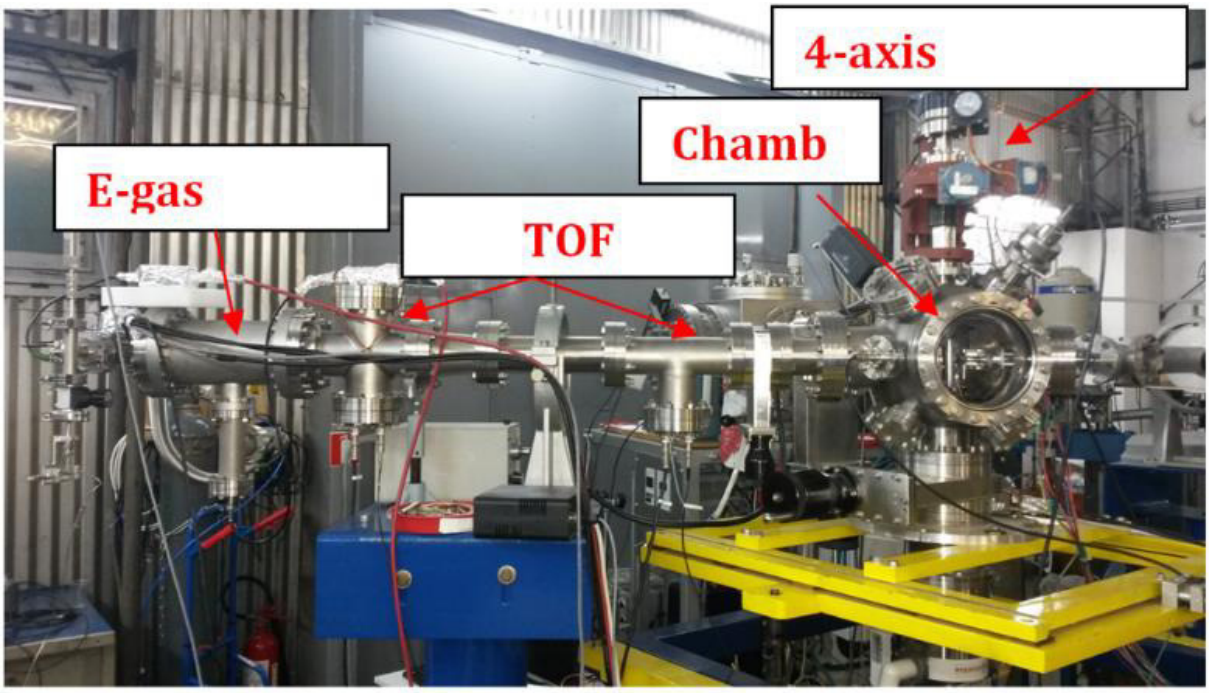

Figure 17: The configuration of the TOF-ERDA equipment system (Ruđer Bošković Institute) [115].

With TOF-ERDA all elements are separated and analyzed in a single step and the depth resolution is in nm range at the surface, with mass resolution of the TOF-ERDA system about 1 amu up to mass of 50 amu and with 10×10 mm^2 limited samples size [116].

For our samples the measurements were carried out using 20 MeV $^{127}I^{6+}$ ions with 20° incidence angle towards the sample surface and the TOF-ERDA spectrometer positioned at angle of 37.5° towards the beam direction were used. The Analysis of TOF-ERDA spectra was done using program Potku [117] and MCERD [118].

3.3.7 Raman Spectroscopy

Raman spectroscopy was used to have more information about the structure of $CrAlSiN_x$, $CrAlSiO_yN_x$ single layers, but it was not so efficient because those layers are amorphous and it difficult to identify the structures. The Raman scattering measurements were performed only for the single thick layers of $CrAlSiN_x$, $CrAlSiO_yN_x$, deposited with different reactive oxygen

and nitrogen partial gases pressure. The measurements were carried out on alpha 300 R confocal Raman microscope (WITec) using a 532 nm Nd: YAG laser for excitation. The system was operated with an output laser power of 2.5 mW. The laser beam was focused on the sample by a ×50 lens (Zeiss), and the spectra were collected with a 600 groove/mm grating using 5 acquisitions with a 2 s acquisition time.

3.3.8 Fourier-Transform Infrared Spectroscopy

Fourier-Transform Infrared Spectroscopy (FTIR) measurements were carried out for the oxide anti-reflection layer and Cr based on optical stack samples to study their thermal stability. They were performed in the wavenumber range of 400 cm^{-1} – 5000 cm^{-1} with a Fourier Transform Infrared spectrometer Bruker IFS 66V equipped with a Globar source, a KBr beam-splitter and a DTGS detector with KBr window. The measurements were performed in vacuum at room temperature and with *p*-polarized light (polarization parallel to the incidence plane) at oblique-incidence (45º) used in the reflectance measurements and the spectra were recorded using 128 scans.

3.3.9 Nanoindentation

The nanoindentation measurements have been carried out for thick individual layers of $CrAlSiN_x$, $CrAlSiO_yN_x$, with different reactive oxygen and nitrogen partial gases pressure deposited on polished stainless-steel substrates using nano/ microindentation-Micro Materials equipment shown in Fig. 18.

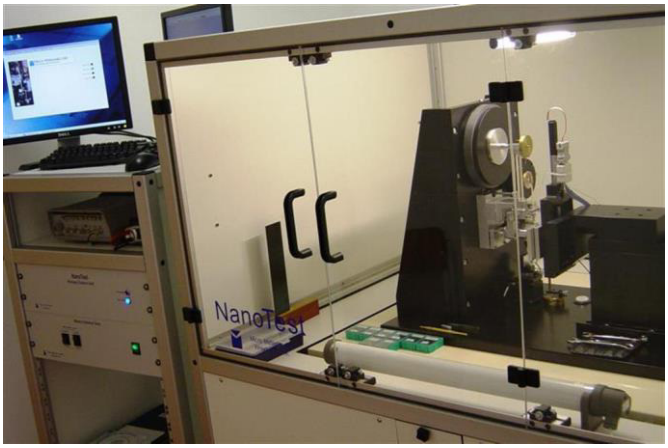

Figure 18: Nanoindentation equipment [108].

The equipment technical specifications are: theoretical depth resolution: < 0.025 nm, load range up to 500 mN for nano-hardness and up to 20 N for microhardness, load resolution: 50 nN, depth range 0-50 mm, contact force: < 5 mN, 50 mm x 5 mm inspectable area, samples manipulation with computer controlled high precision motorized table, X, Y, Z resolution/ travel: 0.05 mm/50 mm, optical image magnified up to at least 500 x, repositioning accuracy in the field of view: 2 mm, environmental cabinet with internal antivibration mounting and comprehensive Windows based on software package for instrument control, calibration and data collection

For our samples the nanoindentation tests were applied with maximum loads ranged between 6 and 8 mN, in order to have an indentation depth below of 10% of the layer thickness. Then, hardness and elastic modulus data were obtained using the method proposed by Oliver and Pharr [118]. For each sample the measurements were repeated five times and the mean of the measurement was calculated.

Chapter 4 Solar selective absorbing coatings based on $CrAlSiN_x$ /$CrAlSiN_xO_y$

4.1 Deposition and Characterization of $CrAlSiN_x$ /$CrAlSiN_xO_y$ single layers

CrAlSiNx and CrAlSiOyNx are examples of multi-elemental thin films. Recently, increasing studies and technological efforts have been devoted to the research on those kinds of materials, due to their excellent properties and numerous industrial applications. Chromium nitrides, oxides and oxy-nitrides generally have high oxidation resistance [52,120-125] , chemical and thermal stability at high temperature [126-131], good thermal diffusion barrier [132], good corrosion resistance [133] and high hardness [134-137]. The numerous applications are divided into two main groups. First one is the optical and electrical applications such as, optical detectors, sensors, optical filters, lenses, emitting diodes, on concentrating solar power (CSP) [46,138-141] and phase shifting masks [142,143]. The second group is for plastic metal molds, cutting and drilling tools [144,145], due to their high hardness and wear resistance. This section devoted to study the influence of varying nitrogen and oxygen partial pressures on microstructure, mechanical and optical properties of sputtered CrAlSiNx and CrAlSiOyNx coatings in the sub-stoichiometric range, where the ratio (O+N)/(Cr+Al+Si) is lower than 1. In literature [146,147], it is found that hard nano-composite coatings based of nc-CrN/a-SiNx are optically opaque. This would be enough for a coating with high solar absorption, but not enough to have a coating with low emissivity. On the other hand, adding aluminium to Cr-Si-N changes the grain size, the composition and the mechanical properties of those materials, and tend to be amorphous and more transparent. This leads to an improvement of oxidation resistance properties and opens the possibility to tune the optical properties. Moreover, oxygen content in films affect the whole coating properties, as an example, if oxygen content in oxynitrides increase, then films will be more transparent with lower refractive index, because they tend to lose their metallic behaviour. Also, hardness values

of such coatings remain low (12–13 GPa) in the range of oxygen ratio [O]/[O+N] of 20%–50% in films as reported by Karimi et al. [125]. So, adjusting oxygen and nitrogen contents enables to control the optical, chemical, mechanical and electrical properties of CrAlSiNx and CrAlSiOyNx coatings within a wide range.

4.1.1 Experimental

A series of thin individual layers of CrAlSiNx and CrAlSiOyNx were deposited on glass substrates with different nitrogen and oxygen partial pressures as reactive gases, as shown in Table 1. These thin layers were used to track the influence of varying those partial pressures upon the optical properties of sputtered CrAlSiNx and CrAlSiOyNx.

Table 1:Oxygen and nitrogen partial pressures of reactive gases in deposition for thin single layers (<100 nm) used to track the optical properties of sputtered CrAlSiNx and CrAlSiOyNx. Deposition rates were calculated from thicknesses obtained using SCOUT software.

Nitride Layer	N_2 Partial pressure (Pa)*	Deposition rate [nm/min]	Oxynitride Layer	N_2/O_2 (85:15) Partial pressure (Pa)*	Deposition rate [nm/min]
1	0.037	47.0	1	0.046	45.9
2	0.051	37.6	2	0.064	42.1
3	0.056	35.9	3	0.068	40.6
4	0.060	33.7	4	0.075	38.8
5	0.071	31.0	5	0.092	28.7
6	0.15	17.3	6	0.21	18.6

* P_{NO} will be used in instead of N_2 /O_2 (85:15) partial pressure and P_N instead of N_2 partial pressure.

For morphology, chemical composition, crystalline structure and mechanical properties studies, thicker samples were deposited on (100)-oriented silicon wafer (used for SEM, XRD,

XPS and RBS analysis) and polished stainless-steel substrates (used for nanoindentation tests) with same parameters as thinner ones, as presented in Table 2.

Table 2: Oxygen and nitrogen partial pressures of reactive gases in of deposition individual thick layers (> 1 µm) used for morphology, chemical composition and microstructure characterization of CrAlSiNx and CrAlSiOyNx. Deposition rates were calculated using thicknesses measured by SEM.

Nitride Layer	N_2 Partial pressure (Pa)	Thickness SEM (µm)	Deposition rate [nm/min]	Oxynitride Layer	N_2/O_2 (85:15) Partial pressure (Pa)	Thickness SEM (µm)	Deposition rate [nm/min]
1	0.033	1.46	48.8	1	0.046	1.29	43.0
2	0.040	1.36	45.2	2	0.053	1.26	42.0
3	0.051	1.26	42.1	3	0.064	1.17	39.0
4	0.056	1.25	41.8	4	0.075	1.08	36.0
5	0.060	1.19	39.6	5	0.092	1.06	35.5
6	0.15	0.52	17.3	6	0.21	0.56	18.7

4.1.2 Optical properties

Fig. 19 shows the transmittance (T) and the reflectance (R) spectra of CrAlSiNx deposited with different N_2 partial pressure, from 0.037 Pa to 0.15 Pa and of CrAlSiOyNx films deposited with different N_2/O_2 partial pressure, from 0.046 Pa to 0.21 Pa. The results presented in the figure show that the CrAlSiNx and CrAlSiOyNx layers become more transparent and lose their metallic behavior as the nitrogen and oxygen partial pressures increase. This is mainly due the presence of to Al and Si nitrides and oxides, which are transparent. In accordance with this, the reflectance in the same wavelength range decreases with increasing nitrogen and oxygen partial pressures.

The optical constants, refractive index (n) and extinction coefficient (k), and layers thicknesses were determined from T and R [61] curves by using the optical simulation program SCOUT [104].

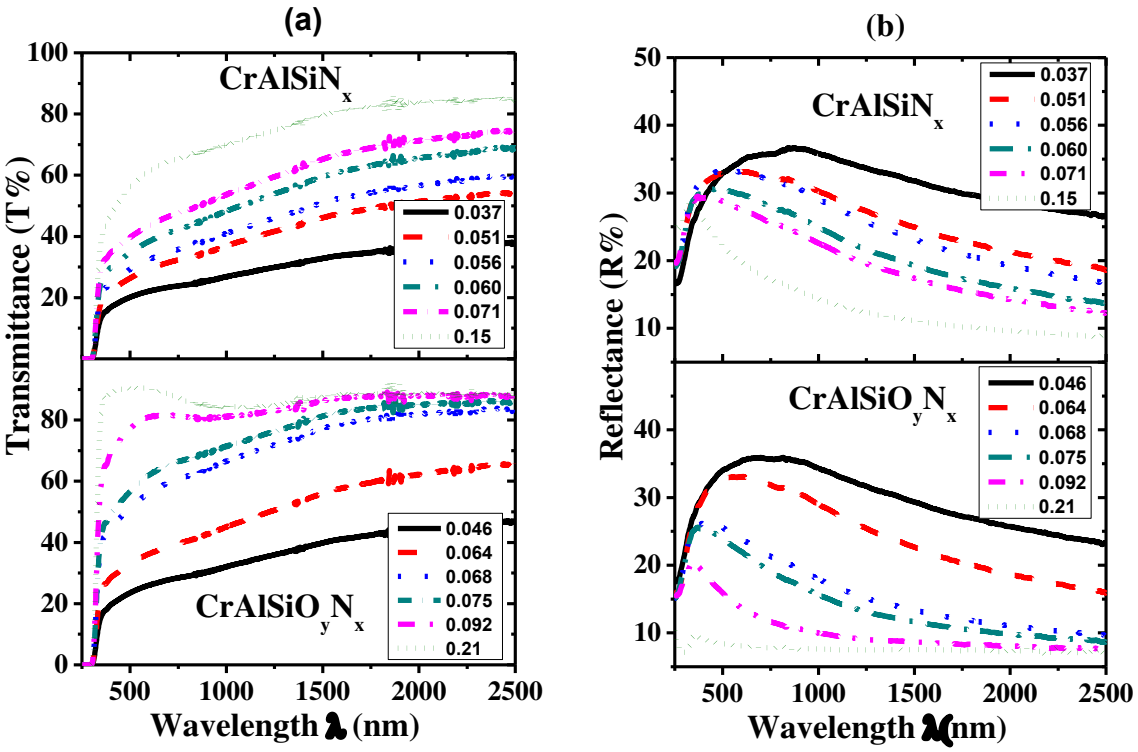

Figure 19: Transmittance (a) and Reflectance (b) of CrAlSiNx and CrAlSiOyNx as a function of oxygen and nitrogen partial pressures.

These thicknesses were used to calculate the deposition rates shown in Table 1, which are slightly lower than those calculated by using the thicknesses of thicker samples, measured by SEM and shown in Table 2. Fig. 20 shows the spectral optical constants, refractive index (n) and extinction coefficient (k), as a function of the wavelength in the range of 250– 2500 nm, which were obtained from the modelling of experimental T and R spectra. The results shown in the figure indicate a general behavior of n and k with a decrease as increasing the gases partial pressures for both nitride and oxynitride layers, which is due to the decrement of the metallic character. Increasing oxygen and nitrogen amount in films caused an increment of the metal-N and metal-O bonds. Moreover, it is seen that the refractive indices for the CrAlSiNx layers increase in the wavelength range 300–1000 nm, which make these layers appropriate materials for selective absorption of solar radiation and other optical applications because it contributes to the solar absorption enhancing through the interference effect, as discussed in section 2.2. The refractive index of CrAlSiOyNx layers also shows a similar behavior with wavelength, but for higher gases partial pressures it becomes almost constant.

The oxygen induces a decrease in both, refractive index and extinction coefficient, for the values that is not possible to get with nitride. For example, the minimum refractive index for nitrides is higher than 2.5, while with oxynitrides it is possible to tune it down to 1.6. A similar effect can be seen for the extinction coefficient, where in oxynitrides can be tuned down to zero, while in nitrides is always higher than 0.2. This behavior is also related with the Cr amount, which cannot be below a certain value in order to have the adequate extinction coefficient for the high absorption layer. As represented in Tables 1 and 2, the deposition rate decreases with increasing oxygen and nitrogen partial pressures due to the formation of nitrides and oxynitrides bonds in the target surface during the film growth (known as target poisoning) [148], resulting in a reduction of sputtered materials and consequently of the deposition rate.

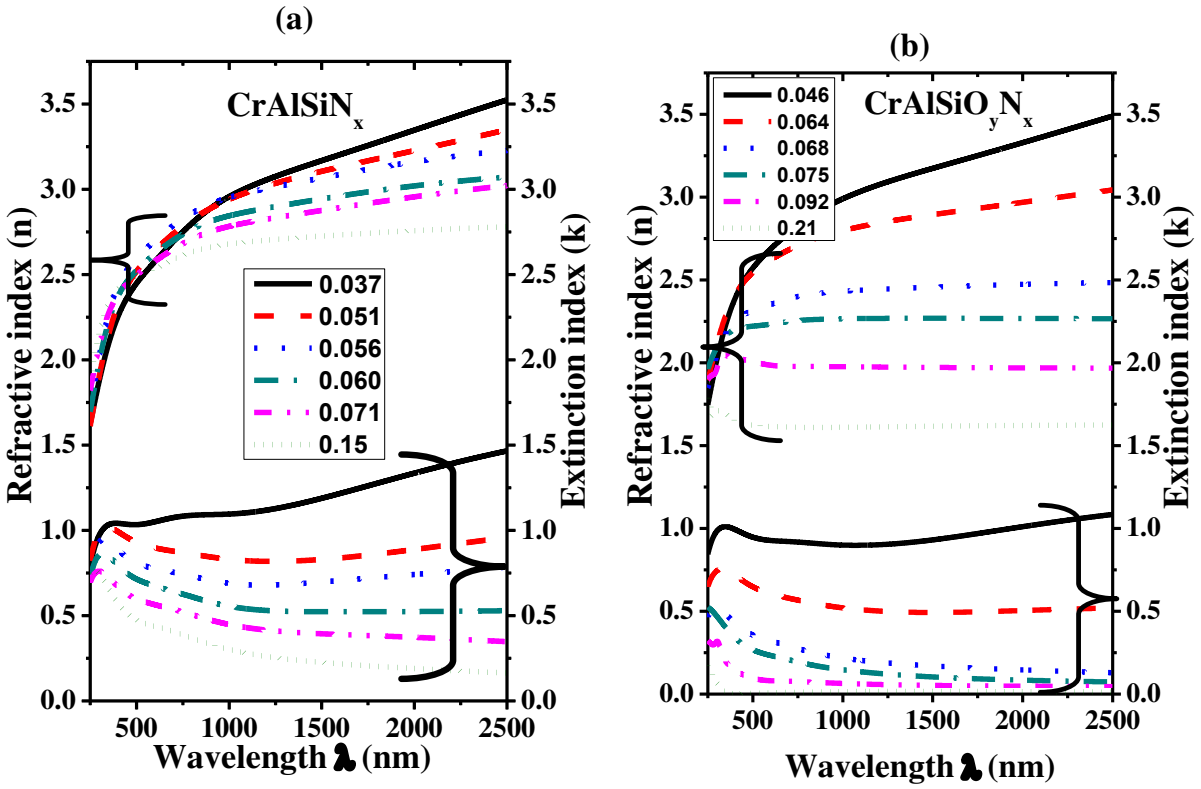

Figure 20: Refractive index (n) and extinction coefficient (k) as a function of wavelength of: (a) CrAlSiNx, prepared with increasing nitrogen partial pressures. (b) CrAlSiOyNx as a function of wavelength, prepared with increasing nitrogen and oxygen partial pressures.

4.1.3 Chemical composition of $CrAlSiN_x$ and $CrAlSiOyN_x$ single layers

As far as Rutherford backscattering spectrometry (RBS) is suitable for analysis of compositional depth profiles of amorphous structures, it was used to analyze the samples' elemental compositions. Fig. 21 shows three typical RBS spectra, namely one of a nitride layer (Fig. 21a) and the other two of oxynitrides layers (Fig. 21b).

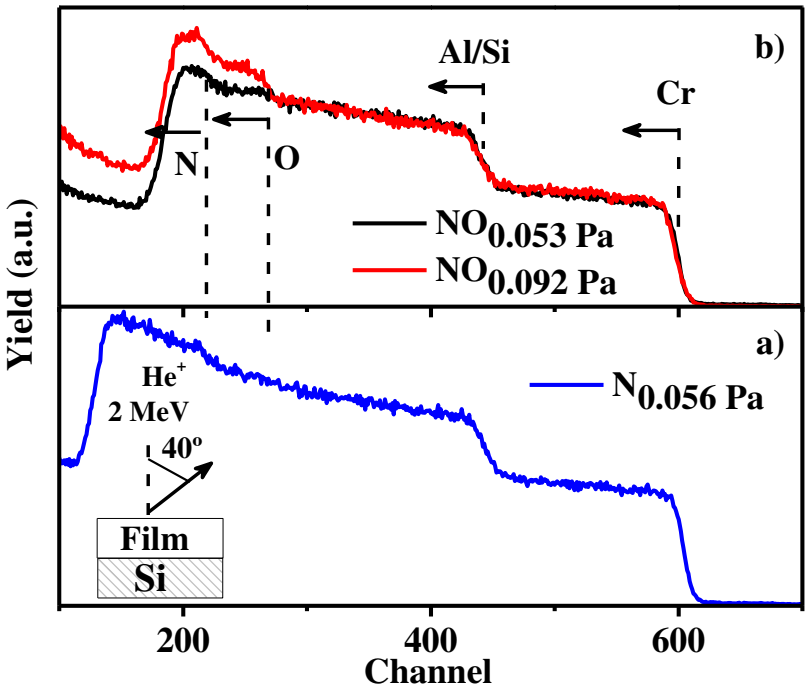

Figure 21: RBS spectra of: (a) nitride layer and (b) two different oxynitride layers.

Since the signals from the different elements overlap, the composition has to be determined from the front edges of the elements, which are indicated in the figure. The relative heights of those front edges are correlated with the relative concentrations of the different elements, and by the analysis of all samples it was verified that the (Al +Si) / Cr composition ratio is about 2 and similar for different samples, as presented in Fig. 22 for all the nitride and oxynitride samples.

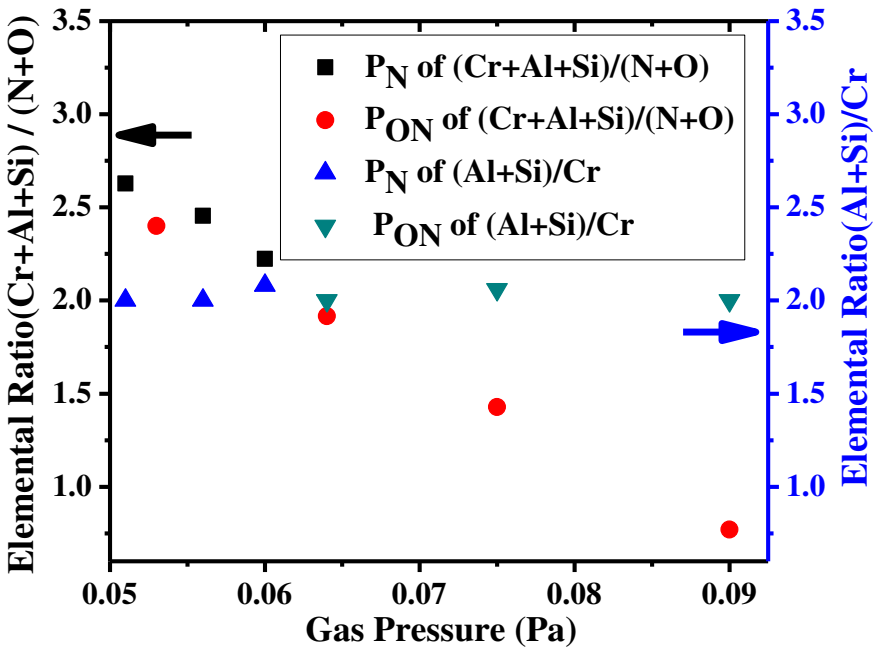

Figure 22: Elemental composition ratios (Cr+Al+Si) / (N+O) and (Si+Al)/Cr in films as a function of P_N for CrAlSiNx and P_{ON} for CrAlSiOyNx films as evaluated by RBS.

With the used conditions, RBS technique is not adequate to have an enough separation between Al and Si front edges. So, EDS technique was used to measure the Al/Si ratio, which is in average 1.5. This means that the Cr: Al: Si ratio composition is 1.25:1.5:1. Fig. 22 also represents the chemical composition ratio (Cr + Al + Si) / (N + O) as a function of the reactive gases partial pressure, P_N in CrAlSiNx samples and P_{ON} in CrAlSiOyNx samples. In both cases, the compositional ratio decreases with increasing the reactive gasses pressures, as expected, which means, an increase of the nitrogen and oxygen contents. Moreover, a small amount of oxygen was detected in the pure nitride's samples. In most samples, the composition ratio (Cr+Al+Si)/(N+O) is higher than 1, which means the films are sub-stoichiometric. Only the oxynitride deposited with reactive gases partial pressure of 0.09 Pa has ratio below one. The layers used in the optical stack coating are sub-stoichiometric.

For more details about the chemical structure, three samples: (A) $CrAlSiN_x$ with P_N =0.056 Pa, (B) $CrAlSiOyN_x$ with P_{ON}=0.046 Pa and (C) $CrAlSiOyN_x$ with P_{ON}=0.075 Pa have been chosen for XPS analysis. Fig. 23 shows the evaluated XPS spectra of the Cr 2p3/2, Al 2p, Si 2p, N 1s and O 1s core levels, while in Table 3 the Casa software the fitting parameters and the identification of core levels binding energies are represented.

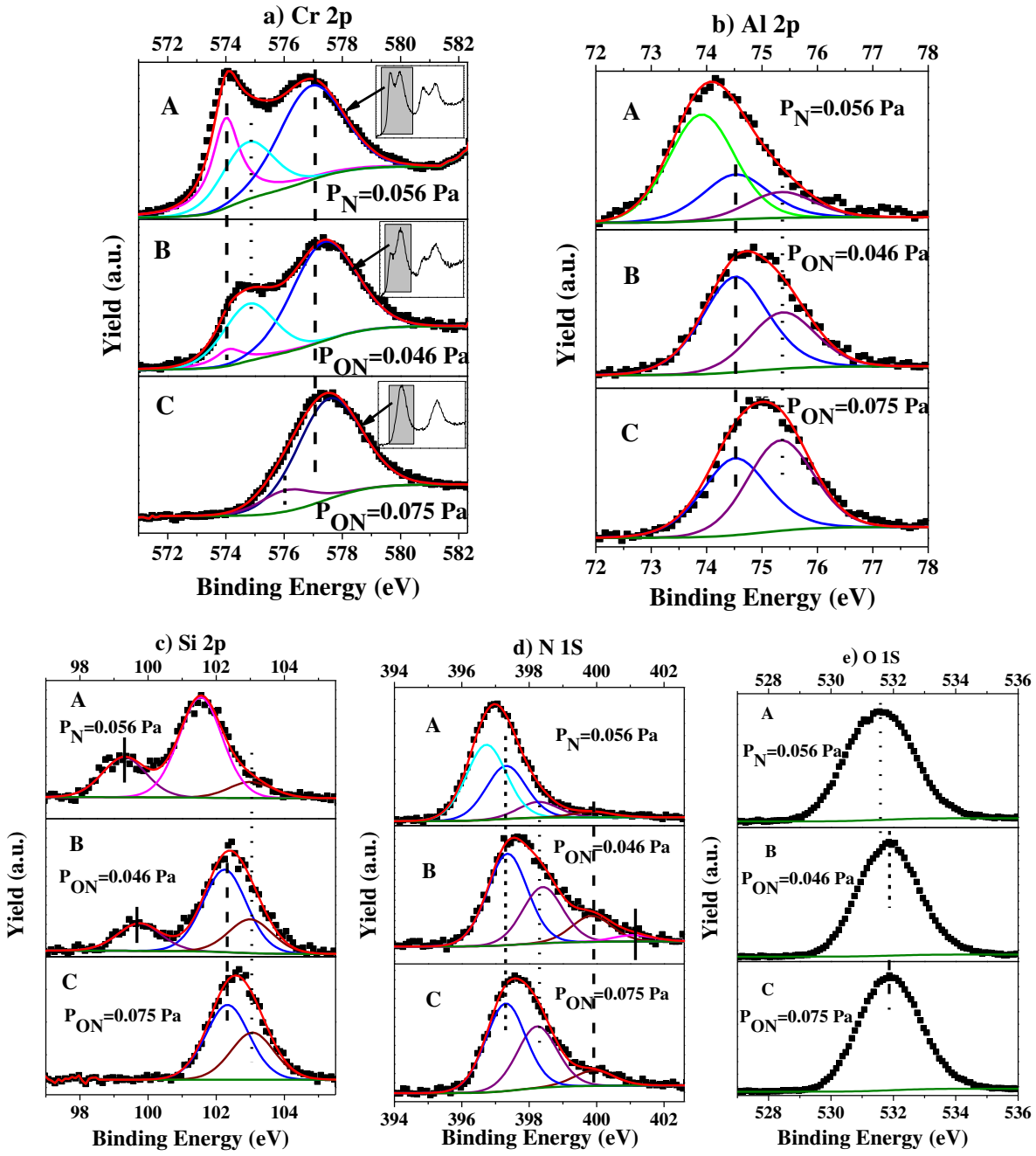

Figure 23: XPS spectra of: (a) Cr 2p3/2, (b) Al 2p, (c) Si 2p, (d) N 1s and (e) O 1s electrons for the three samples: A, B and C. The green curve represents the background correction.

As shown in Fig. 23a, the XPS spectra of Cr $2p_{3/2}$ binding energy (the entire Cr 2p core level peaks are shown in the insert) can be deconvoluted into three sub-peaks, in the case of samples A and B. The respective energies of 574.1 eV, 574.8 eV and 577.4 eV are corresponded to the metallic Cr, CrN and Cr_2O_3, respectively [124,149-153]. For higher partial

pressure of P_{ON}, as in sample C, the peaks corresponding to the metallic Cr and CrN were not observed and a new peak centred at 576.1 eV appears, which may be an overlap between Cr-O and Cr_2N. Moreover, the Cr $2p_{3/2}$ doublet shifts towards higher binding energy with increasing oxygen content in the films, which indicates an increment of oxidation bonds in films [136].

For the Al 2p spectra, the oxynitride samples revealed two peaks located at 74.5 and 75.4 eV, as shown in Fig. 23b, whereas for the nitrides another peak is seen, centred at 73.9 eV due to higher content of nitrogen in the film. The peaks at 74.5 eV and 75.4 eV are considered as $Al(OH)_3$ and Al_2O_3 compounds, respectively [48], and the third peak, at 73.9 eV, is recognized as AlN [52,130,134].

Fig. 23c shows the Si 2p core level spectra, and it is seen that the peaks of samples A and B correspond to the contribution of three distinct components, while the peak of sample C only has two components. The peak centred at 103.0 eV in all three samples is recognized as silicon oxides in the form of Si(Al)-SiO_3 or SiO_4 bonds [26,154], considering a silicon-centred tetrahedrons, in which silicon, oxygen and nitrogen atoms are bonded in the form of any of the four tetrahedral sites of $Si–Si_{4-(m+n)}O_mN_n$ (where $m+n\leq4$; m,n=0-4) and the chemical shift of Si 2p level for each of the four tetrahedral is proportional to the partial charge on the Si atom [155]. The 99.3 eV component that appears in sample A and B could be Si-Si(Al) [130]. The last peak of sample A located at 101.5 eV is recognized as Si_3N_4 bond [120,124,130,135], and the peak at 102.3 in sample B and C is related to the formation of silicon oxynitrides Si-N_3O or Si(Al)-SiO_2N bonds [26,156].

As shown in Fig. 23d, the XPS spectra of N 1s core level can be deconvoluted into five peaks. The peaks at energies 397.3, 398.2 and 399.9 eV can be associated to Si_3N_4 [19,46], chromium oxynitride [157] and Si(Al)-O_2N_2 [152] bonds, respectively. The fourth chemical component that appears only in sample A is located at 396.7 eV, and it describes Al -N bonds [26,135,157,158]. The peak in sample B located at 401.1 eV is related to CH=N-CH surface contamination.

Table 3: Casa software fitting parameters and identification of core level binding energies.

Core Peak	FWHM (eV)	BE (eV) sample A	BE (eV) sample B	BE (eV) sample C	Compound
Cr2 p3/2	1.2	574	574.1	-	Cr- Cr
	2.6	574.8	574.8	-	Cr-N
	2.1	576.9	577.4	577.5	Cr-O; Cr-$(OH)_3$
	2.1	-	-	576.1	Cr-O; Cr_2N
Al 2p	1.4	73.9	-	-	Al-N
	1.4	74.5	74.5	74.5	Al-(OH)
	1.4	75.4	75.4	75.3	Al-O
Si 1s	1.5	99.3	99.7		Si-Si (Al)
	1.5	101.5	-		Si_3N_4
	1.5	-	102.3	102.3	Si(Al)-Si_2O_2 ; Si(Al)-SiO_2N
	1.5	103.0	103.0	103.0	Si(Al)-SiO_3; Si-O_4
N 1s	1.4	396.7	-	-	Al-N
	1.4	397.3	397.4	397.3	Si_3N_4
	1.4	398.3	398.4	398.2	chromium oxynitride
	1.4	399.9	399.9	399.9	N-(C=O); Si (Al)-O_2N_2
	1.4	-	401.1	-	CH=N-CH

Fig. 23e shows the O1s spectra, which were not fitted into its components' peaks because it is difficult to identify their bonding energy. However, it should contain several peaks that can describe the chemical composition of samples. It is worthy to mention that the position of the oxygen peak shifts to higher energies with increasing the percentage of oxygen in films due to formation of oxides and oxynitrides, in accordance with what was reported in the literature [136]. From the corresponding core-level intensities and tabulated atomic sensitivity factors, the relative atomic concentrations were calculated. Due to the surface contamination, the oxygen is significantly larger than those measured by RBS and EDS. Additionally, the average (Al+Si)/Cr composition ratio for these 3 samples is now 4.1, two times higher than the bulk composition ratio obtained by RBS and EDS, and the Al/Si ratio also revealed an increase (1.9 instead of 1.5, in average). Considering that XPS measures the elements and the quantity of

those elements that are present within the top 1-10 nm of the sample surface, this means that surface contamination led to an Al surface enrichment and a significant Cr depletion.

4.1.4 The crystalline structure of $CrAlSiN_x$ and $CrAlSiOyN_x$ single layers

Thick layers of $CrAlSiN_x$ and $CrAlSiOyN_x$ deposited on silicon wafer substrates were used for the X-ray diffraction, that are shown in Fig. 24. In the diffractograms of $CrAlSiN_x$ and $CrAlSiOyN_x$ films in the ranges of P_N =0.037 - 0.071 Pa and P_{NO} =0.046 - 0.091 Pa, respectively, no strong peaks were observed, which means they are amorphous. For higher nitrogen and oxygen partial pressures, XRD results revealed that the two samples $CrAlSiN_x$ with P_N =0.15 Pa and $CrAlSiOyN_x$ with P_{NO} =0.21 Pa are polycrystalline with cubic (fcc-B_1) structure, with CrN peaks (111), (200), (220) and (222) at expected position as shown in Fig. 24 [159,160]. The chemical composition of these samples was not measured with RBS, but from data shown in Fig. 22, it can be expected a composition ratio (Cr+Al+Si)/(N+O) below one, which means those films should be stoichiometric, which should be the main reason for some microstructure changes.

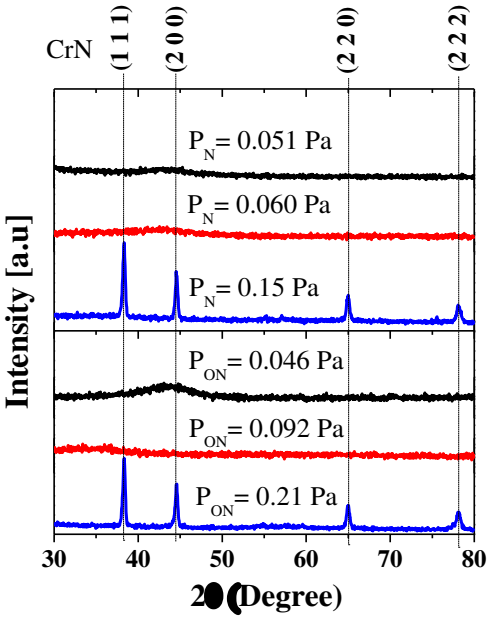

Figure 24: XRD difractograms of CrAlSiNx and CrAlSiOyNx films for different nitrogen and oxygen partial pressures.

Fig. 25 represents SEM cross-sectional micrographs of several films that show the morphology and the thickness as varying reactive gases partial pressure. The amorphous structure of the films is mainly due to the high amount of aluminium and silicon in the films, and due to the sub-stoichiometry of the films [(O+N)/(Cr+Al+Si) <1]. In oxynitride case, it can be due to the fact that the mobility of oxygen in the growth surface of amorphous films is not sufficient to form oxide lattice [159], although for those partial pressures the films are still sub-stoichiometric, as shown in Fig. 22.

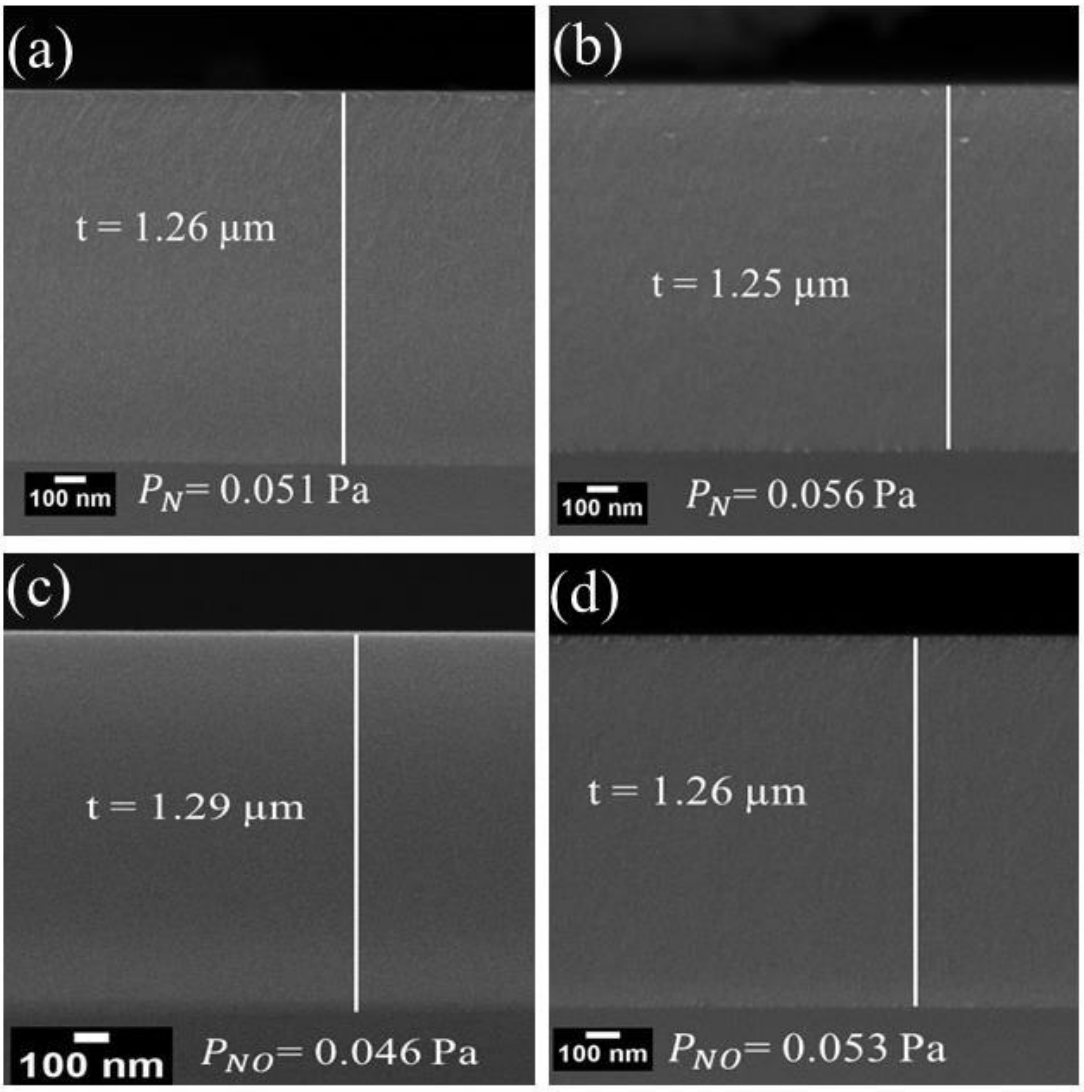

Figure 25: Cross-sectional micrographs show a featureless morphology compatible with an amorphous structure of CrAlSiNx and CrAlSiOyNx films for different nitrogen and oxygen partial pressures.

Several $CrAlSiO_yN_x$ thick single layers deposited on silicon were characterized by Raman spectroscopy and their correspondent spectra are shown in Fig. 26. All measured samples were amorphous, and due to that reason, the signal from their elemental vibrational modes was very weak with used incident power conditions (very low laser incidence power) [157,161,162], as shown in the figure.

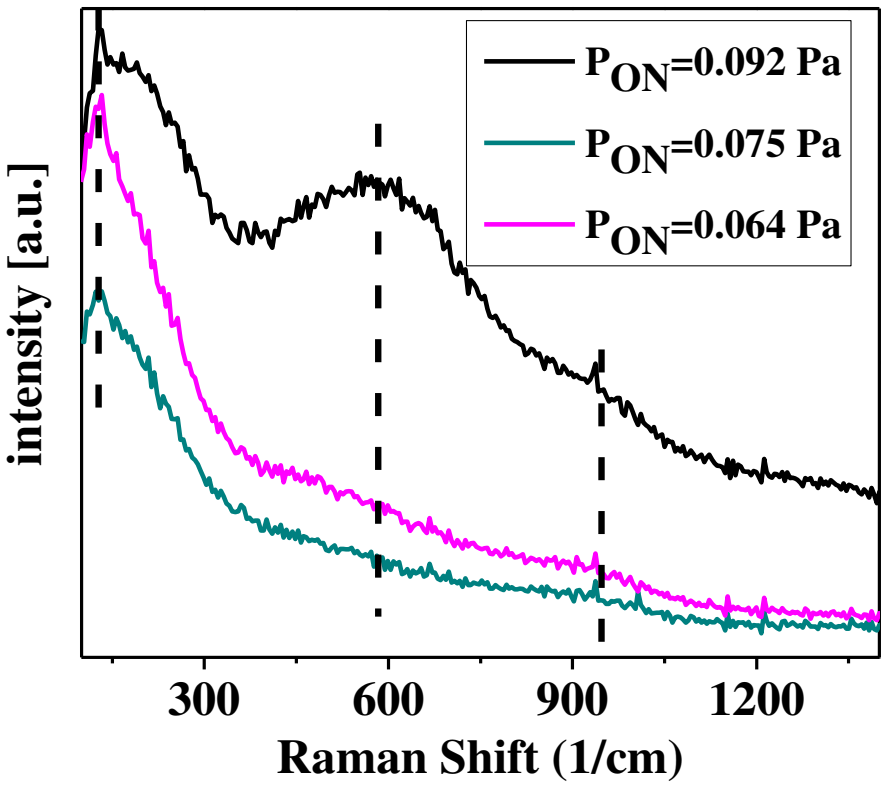

Figure 26: Raman spectra of chosen CrAlSiON samples.

All samples show two broad bands at approximately 190 cm^{-1} and 250 cm^{-1}, with intensity ratio between the 190 cm^{-1} and 260 cm^{-1} ranging from 1.3 (P_{ON}=0.075 Pa) to 1.8 (P_{ON}=0.046 Pa). This low intensity ratio indicates that the presence of oxygen in the layer is not favourable to the formation of wurtzite structure.

4.1.5 Mechanical properties of $CrAlSiN_x$ and $CrAlSiOyN_x$ single layers

To probe the mechanical properties, such as the hardness and the elastic modulus, a nanoindentation method has been applied to the thick samples deposited on polished stainless-steel substrates. The maximum load was selected in order to have the indenter penetration depth lower than 10% of the coating thickness, and therefore the maximum load is below 8 mN, as shown in Fig. 27a and Fig. 27b, where the load depth curves are represented for one measurement of each sample.

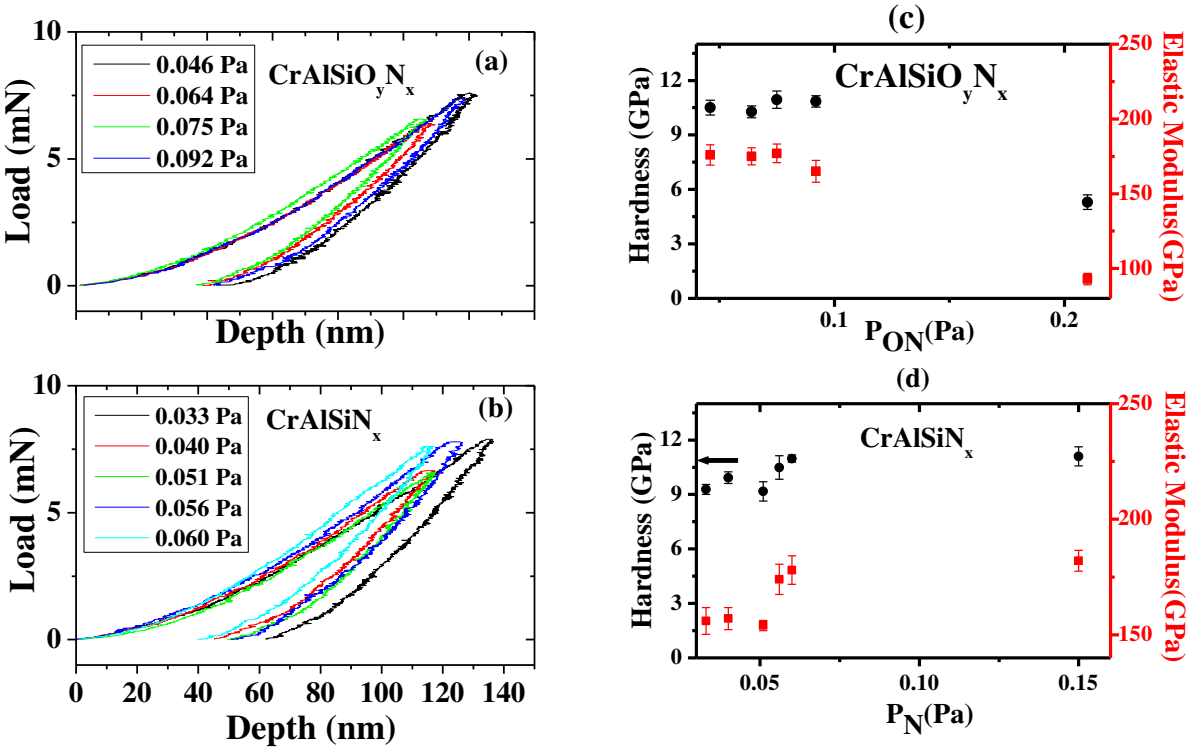

Figure 27: (a) and (b) load – depth curves of CrAlSiOyNx and CrAlSiNx, respectively. (c) and (d) hardness and elastic modulus of CrAlSiOyNx and CrAlSiNx as varying P_{ON} varying P_N, respectively.

The evaluation of hardness and elastic modulus with increasing P_N and P_{ON} are presented in Fig. 27. With increasing P_{ON} from 0.046 Pa to 0.092 Pa, no significant changes were seen in the hardness values (Fig. 27c). On the other hand, a notable decrement was seen in the hardness and elastic modulus values when P_{ON} increased to 0.21 Pa. For nitrides films, the hardness was

slightly increased with increasing P_N from 0.051 Pa to 0.15 Pa. The highest obtained value was 11.1 GPa at 0.15 Pa, as shown in Fig. 27d. the hardness values are relatively low, but it is in the same range of magnitudes obtained by Karimi et al. [159][125] with oxygen ratio [O]/[O+N] in films up to 20% . In those studies, the ratio (Al+Si)/Cr ~1 while in this case (Al+Si)/Cr ~2, which has a strong influence on the film properties. The sub-stoichiometry and the amorphous phase fraction can be considered as other factors contributing for poor hardness.

Depending on the results discussed in previous section, the variation of nitrogen and oxygen partial pressures induces an increase of those elements in sample composition, as expected, which also result in a strong variation of films' optical properties. However, the hardness is almost insensitive to the variation of those partial pressures, mainly due to the elemental Cr: Al: Si composition ratio of 1.25:1.5:1. The optical constants of $CrAlSiN_x$ and $CrAlSiO_yN_x$ samples are very sensitive to nitrogen and oxygen partial pressures. The most appropriate ranges of P_N and P_{ON} for selective solar absorber stacks are 0.037- 0.06 Pa and 0.046- 0.07 Pa, respectively.

4.2 Antireflection $SiAlO_x$ oxide layer

Recently, insulating SiO_2, Al_2O_3 and $SiAlO_x$ oxide layers have been used extensively in selective solar thermal absorbers coatings for high temperature applications. Using $SiAlO_x$ instead of SiO_2 or Al_2O_3 enable to have a combination between the properties of SiO_2 and Al_2O_3 properties, which may improve the fracture toughness, corrosion and oxidation resistance, and silicon addition to Al_2O_3 films provides an optimal combination of breakdown field strength, band off set and dielectric constant [163]. $SiAlO_x$ antireflection oxide layer was used in designs presented in this research because it enables to control the optical properties of the film by controlling its silicon composition. The addition of silicon provides the possibility of controlling their dielectric constant to have the desired optical properties, which make them good candidates for insulating films for the selective solar thermal absorbers [164].

The antireflection $SiAlO_x$ oxide layer also protects the other inner layers of solar selective thermal absorber tandems against oxidation.

$SiAlO_x$ anti-reflection layer was deposited by DC magnetron sputtering on Si (100) wafer (used for SEM analyses), glass (used for tracing the optical properties of films) and stainless-steel (AISI304) substrates (used for EDS, XRD and FTIR analyses). It was deposited using a Si80Al20 at% target in the case of the nitride/oxynitride based optical stacks in static mode and Al target with the 9 small silicon disc pellets for the AlSiOx:W cermet optical stack in a rotation mode, with oxygen as reactive gas.

In order to obtain transparent and dielectric coatings, it is necessary to guarantee that the deposition parameters allow to obtain an adequate metal/oxygen ratio. In this sense, the first step was the determination of the hysteresis curve as a function of oxygen to evaluate if transparent coatings were being obtained.

The hysteresis curves indicate that the variation of target voltage with reactive gas flow, which allows to monitor the target surface condition. The target can operate either in metallic mode for low reactive gas flows, in transition mode, and in reactive or in poisoned mode for higher reactive gas flows, which will determine the coatings chemical composition as well as the deposition rate, since the oxidized target surfaces show a lower sputtering yield in relation to metallic targets, which leads to lower deposition rates in reactive mode. The oxygen partial pressure was determined to be 0.06 Pa, in case of a current density of 6.4 mA/cm^2, for all antireflection layers presented in this thesis.

4.2.1 Chemical composition and structure of the $SiAlO_x$ oxide layer

The coating's chemical composition of $SiAlO_x$ (in static mode during the deposition) and $AlSiO_x$ (in rotation mode during the deposition) was assessed by means of EDS and it is presented in Table 4.

Table 4: Chemical composition of $SiAlO_x$ and $AlSiO_x$ thick layer obtained by EDS analysis.

Layer	O At%	Al at%	Si at%	Ar at%
SiAlOx	61	12	26	1
AlSiOx	61	13	25	1

The grazing incident X-ray diffractograms of the antireflection layer is shown in Fig. 28a. The spectra indicate that the coatings are amorphous, which agrees with the SEM cross-sectional micrographs shown in Fig. 28b, where is seen a featureless morphology, typical of amorphous coatings.

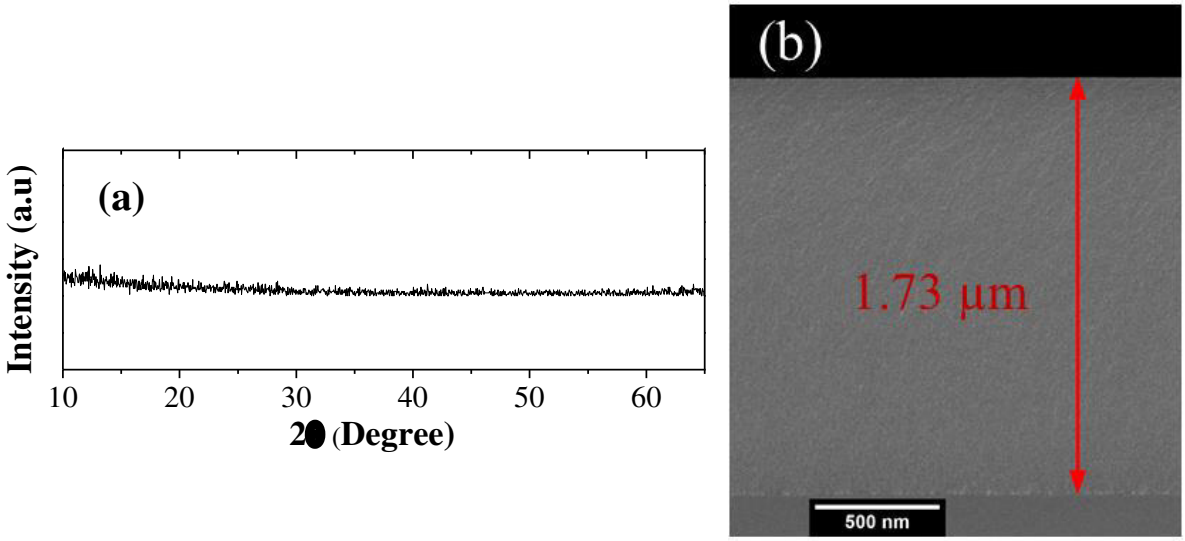

Figure 28: (a) XRD diffractograms of the $SiAlO_x$ anti-reflection layer, (b) Cross-sectional micrograph shows the compact featureless morphology of thick $SiAlO_x$ antireflection layer deposited on silicon.

4.2.2 Optical properties of $SiAlO_x$ antireflection layers

The optical properties of the SiAlOx oxides layers are very important due to their high transmittance and low reflectance. This is associated with low refractive index and almost zero extinction coefficient, which allow their use as antireflection layer in several applications. All samples show a high transmittance and low reflectance for all coatings. To compare the refractive indices and extinction coefficients of SiO_2, Al_2O_3 and $SiAlO_x$ oxide layers, three samples deposited on glass were used to trace the optical constants by SCOUT as shown in Fig. 29, where the SiAlOx layer has a refractive index of 1.52. This behavior was expected since the refractive index of silicon oxide and aluminum oxide are 1.48 and 1.67, respectively, and only a small Al content was added.

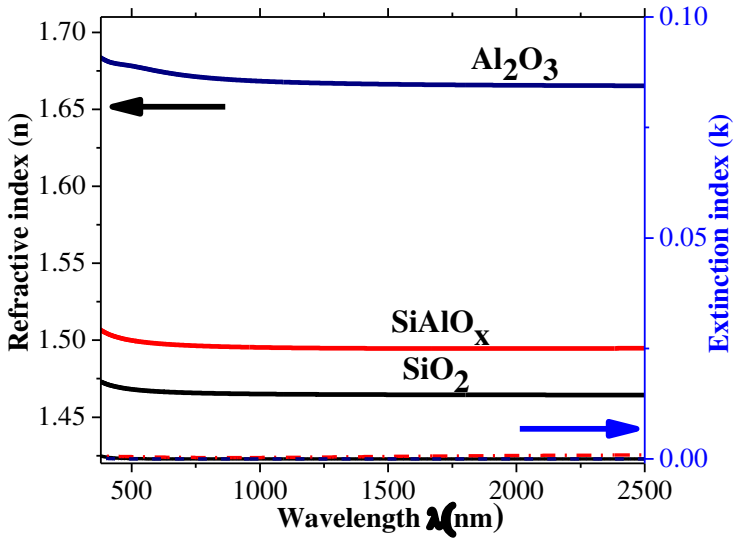

Figure 29: Refractive index (n) and extinction coefficient (k) of Al_2O_3, $SiAlO_x$ and SiO_2 deposited on glass substrates as a function of wavelenght (λ).

4.3 Tungsten back-reflector layer

Elemental tungsten (W) is a good candidate for the back-reflector layer in selective thermal absorber tandems, due to its high temperature melting point and due to the high reflectance in IR region of radiation (R% = 94.6 at λ > 2.5 μm) as shown in Fig. 30a. High reflectivity of W

in IR region decreases the whole emissivity of optical stacks. In addition, W also contributes in the energy absorption at solar radiation region, due to its reflectance in visible region. As mentioned in the general experimental description in Ch. 3, tungsten was deposited with higher current density than other layers to have structure with α- phase and less contaminants, because such conditions affect the stability and reflectance of W IR wavelength region. Even that, most of W coatings showed a combination of both α- and β- phase of growth, the α-phase is the dominant and is polycrystalline with (1 1 0) orientation (2θ=40°) as shown in Fig. 30b. The formation of β- phase depends on the partial pressure of oxygen (or base pressure) of the chamber, the film thickness, substrate bias and deposition rate/deposition power [165-167].

Indeed, the SEM cross sectional micrographs of thick tungsten single layer are completely agreeing with the XRD analysis, as shown in Fig. 30c. Table 5 presents some general physical and chemical properties.

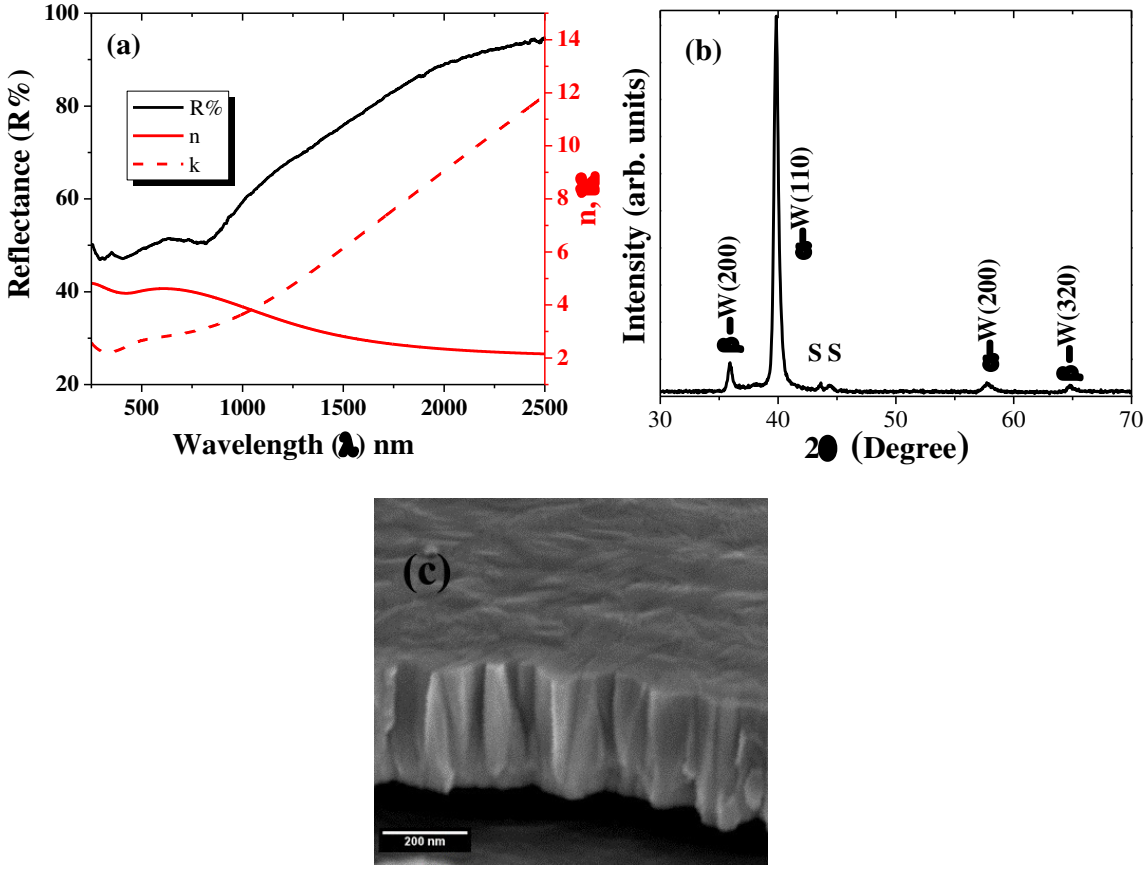

Figure 30: (a) Reflectance, n and k of tungsten deposited on polished stainless steel, (b) XRD pattern of W single layer, deposited on stainless steel (S), performed with fixed incidence angle of 3°and (c) Cross-sectional SEM micrographs of tungsten (W) layer.

Table 5: Some general physical and chemical properties of elemental tungsten (W).

Property	Details
Atomic number (Z)	74
Element category	Transition metal
Free electron configuration	$4f^{14}\,5d^{4}\,6s^{2}$
Phase	solid
Melting point	3422 °C
Boiling point	5930 °C
Density	19.3 g/cm^3
Oxidation states	6, 5, 4, 3, 2, 1, 0, −1, −2, −4
Thermal conductivity	173 W/ (m.K)
Electrical resistivity	52.8 nΩ.m (at 20 °C)
Sputtering yield	600 eV

4.4 Multilayer coatings

4.4.1 Design: simulation and experimental

Beginning with the individual thin layers deposited on glass and with the help of SCOUT software, the final tandem is obtained with a layer's structure, thicknesses and simulated reflectance curve, as shown in Fig. 31. The layers and respective spectral optical constants used in the simulation are those described in sections 4.1 ($CrAlSiN_x$ and $CrAlSiO_yN_x$ layers), in section 4.2 ($SiAlO_x$ layer) and section 4.3 (W layer). It is very important to ensure again that efficient selective absorber can be achieved if it has a graded refractive index and extinction coefficient that decrease from back-reflector W-layer towards the antireflection layer. In ideal case, at the front of the antireflection layer, n and k should be 1 and 0, respectively [168,169].

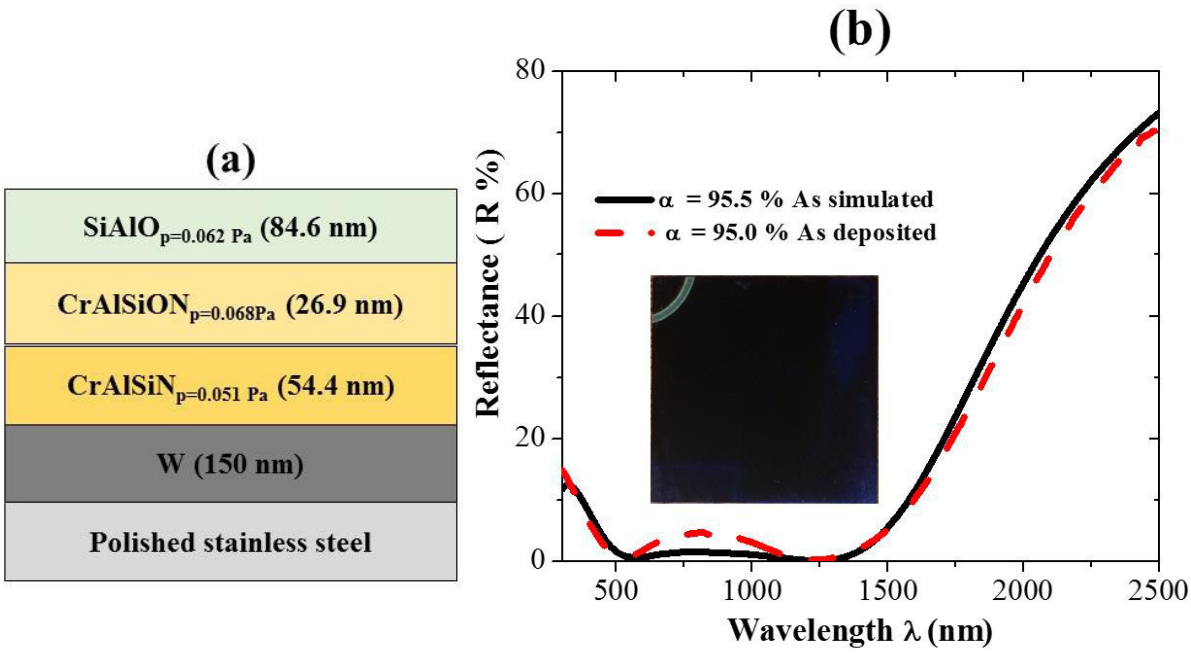

Figure 31: (a) Schematic diagram of the simulated multilayer as obtained by SCOUT. (b) Simulated and experimental reflectance curves of the absorber design.

As shown in Fig. 31a, the optical stack is composed of four layers, the first is a back-reflector tungsten layer, which is followed by two absorption layers based on $CrAlSiN_x$/ $CrAlSiO_yN_x$ structure for phase interference. The final layer is an antireflection layer, that consists of $SiAlO_x$. The total simulated thickness of the whole multilayer's absorber ($W/CrAlSiN_x/CrAlSiO_yN_x/SiAlO_x$) is ~ 316 nm. In the figure are indicated the thicknesses of different layers and the reactive gases partial pressures of the layers used in the simulation. More about the experimental details of the complete design are presented in Table 6. The reflectance of as-deposited multilayer shows good agreement with simulated one except small differences in the reflectance curves and absorption value, as shown in Fig. 31b. This is due to the parameters of reactive sputtering deposition, where small variations can happen, such as target poisoning, chamber base pressure and outgassing during deposition. The final design shows simultaneously high solar absorbance in average α_{sol}= 95.2 % and low emissivity ε= 9.8 % (at 400 ºC).

Table 6: The experimental details of the multilayer stack, deposited in static mode.

Layer	Target [1]	Deposition time	Target Current density (A/cm^2)	Reactive gas partial pressure (Pa) [2]
W	W	2 min & 30 s	12.7	-
$CrAlSiN_x$	70-30 at% Cr-Al and 9 Si pellets	1 min & 27 s	6.4	$P_N = 0.051$
$CrAlSiO_yNx$	70-30 at% Cr-Al and 9 Si pellets	46 s	6.4	$P_{ON} = 0.068$
$SiAlO_x$	80-20 at% of Si-Al	1 min & 38 s	6.4	$P_O = 0.062$

[1]The diameter of the targets: W, Cr-Al and Si-Al is 10 cm, and the diameter of Si pellets is 1cm placed on the Cr-Al target erosion zone.

[2] P_N, P_{ON} and P_O are the nitrogen, nitrogen/oxygen (85%:15%), and oxygen partial pressures of reactive gases, respectively.

In accordance to that, Fig. 32 shows a cross-sectional SEM micrograph of the optical stack, deposited on silicon substrate. The tungsten (W) layer shows a typical morphology of a columnar growth type, whereas the remaining layers reveal a featureless morphology that completely agrees with XRD analysis, where they revealed as being XRD amorphous.

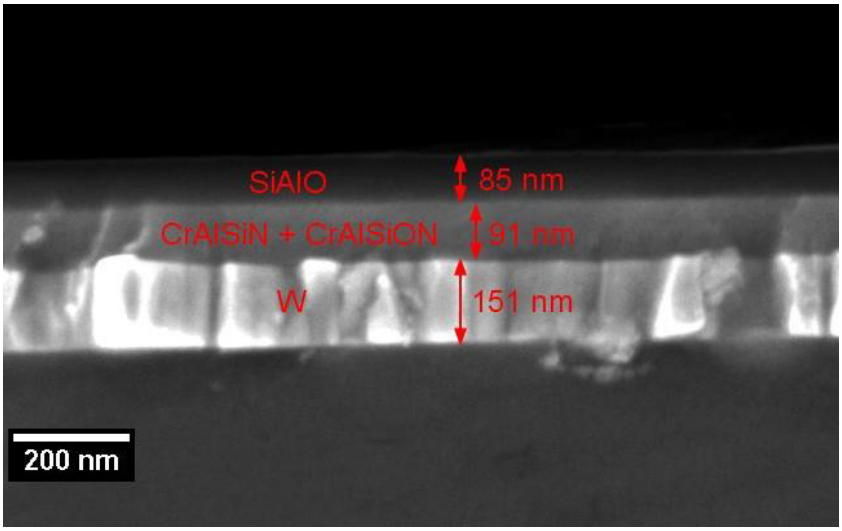

Figure 32: Cross-sectional SEM micrograph of the optical stack, deposited on silicon substrate.

4.4.2 Thermal stability

For long lifetime, selective solar absorber stack should have good resistance against oxidation and it should be thermally and chemically stable. So, the optical stack was subjected to annealing tests in air, at 400 ºC, and in vacuum, at 600 ºC, for 650 h. Then, the solar absorbance (α_{sol}) was measured after each annealing step, and the emittance (ε) was calculated from IR reflectance for each sample in as deposited state and after the last step of thermal annealing. Fig. 33a represents the reflectance curves of a sample in as deposited state, and after 350h and 650h of air annealing. There is a very small shift in the step of the reflectance curve towards lower wavelength. As a result, the solar absorptance was improved a bit and the absorber stack shows good thermal stability. Fig. 33b shows the reflectance curves of a sample in as deposited state, and after a vacuum annealing for 50h, 350h and 650h. Now, the shift towards lower wavelength was higher than air annealing case, especially after the first step of annealing (50 h).

After further steps of vacuum annealing the changes were small, demonstrating that the optical stack has very good thermal stability at this temperature. The shift caused a small decrease in solar absorptance (from 95.5 % to 95.0 % as shown in Figure 33b), but the emissivity improved (it decreased from 11.4% to 9.4% at 600 ºC). The changes in the wavelength range $\lambda<2000$ nm can be related with oxidation of some Si atoms not yet completely oxidized. Whereas, changes in wavelength range $\lambda> 3000$ nm can be due to tungsten phase changes, as will be discussed in the barrier layer section. The small changes in additional steps can also be related with the diffusion of layer elements, such as the diffusion of Cr towards surface as will see in RBS analysis, or to the diffusion of oxygen towards the oxynitride layer.

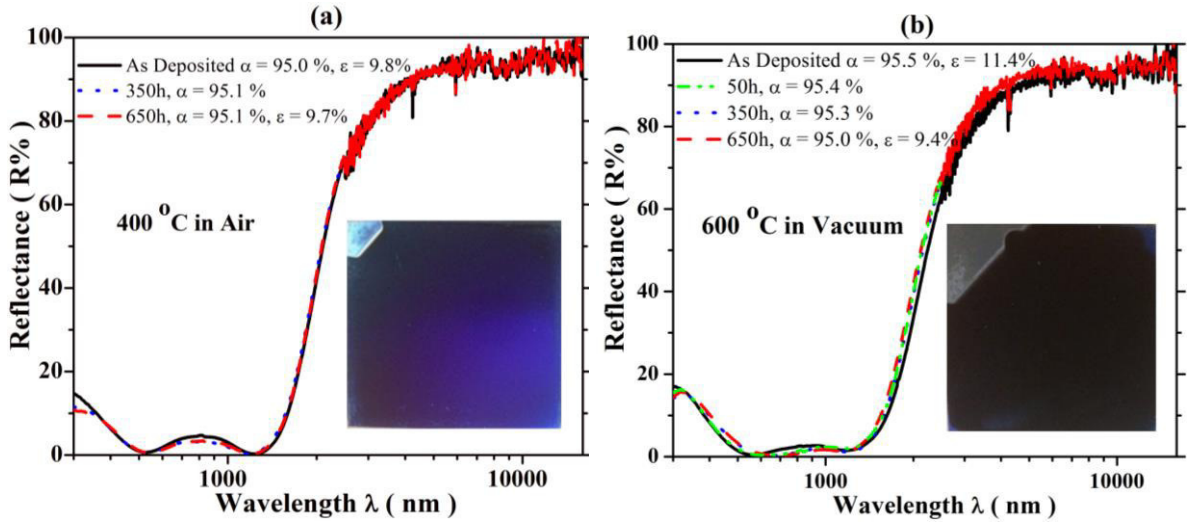

Figure 33: the reflectance of as deposited optical stack and after (a) air thermal annealing at 400 ºC (b) vacuum thermal annealing at 600 ºC, with measured value of the thermal absorptance (α) and the thermal emittance (ε) (for 400 ºC).

The elemental depth profiles of the absorber were studied by Rutherford back scattering (RBS). Fig. 34 shows the RBS spectra of three optical stacks deposited in same run and subjected to different thermal load, namely as deposited, after air annealing at 400 ºC for 650 h and after vacuum annealing at 600 ºC for 650 h. Since the signals from the different elements can overlap, the composition should be determined from the front edges of the elements, which are indicated in the figure. The relative heights of those front edges are correlated with the relative concentrations of the different elements. The position of the different elements, if located at surface sample, are indicated in the graph. It is difficult to distinguish between silicon and aluminium because of the small difference of their atomic mass. However, the analysis shows a small difference between as deposited and annealed samples. After air annealing a small change is seen in the stainless-steel substrate, which was not clearly identified. On the other hand, after the vacuum annealing at 600 ºC, it can be seen changes of W and Cr depth profiles (amplified in insert of Fig. 34), which are in accordance with the diffusion of small amount of tungsten towards the stainless-steel substrate and chromium, mainly from $CrAlSiO_yN_x$ layer, towards the surface. The general evaluation shows that there are no other significant changes occurred after the annealing in vacuum and air. So, a diffusion barrier layer should be added between stainless-steel substrate and tungsten layer to improve barrier diffusion between these layers.

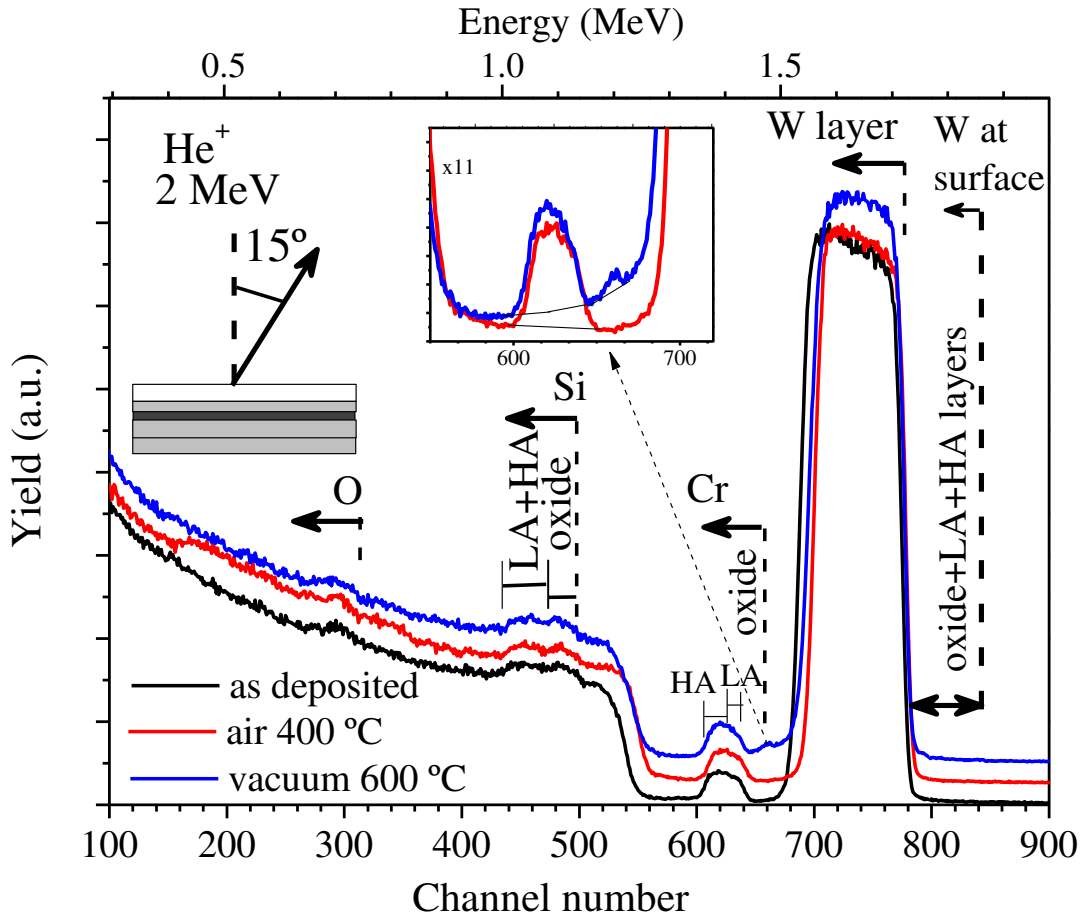

Figure 34: RBS spectra of the as deposited stack, after air annealing at 400 ºC and vacuum annealing at 600 ºC, both for 650 h. The spectra are shifted along vertical axis for clarity.

TOF-ERDA is also used to study the elemental diffusion and thermal stability. The measurements allowed to determine the concentration depth profiles of all the elements in the three samples. Monte Carlo (MC) simulations [116] were used to find the best fits between the elemental energy spectra extracted from TOF-ERDA measured data and the simulated energy spectra taking in the account all spectral details of the experimental setup and the multiple scattering effects in the recoiling process. Fig.35 shows an example of TOF-ERDA histogram data, experimental and simulated energy spectra for oxygen recoils and the corresponding depth profiles used in the simulations. All the observed elements (H, C, N, O, Al, Si, Cr, Ar, W, and Fe) were fitted with simulations in the same way, yielding the concentration profiles of all the elements in the three samples. The oxygen and chromium depth profiles allow the identification of the three outermost layers, $SiAlO_x$, $CrAlSiN_xO_y$ and $CrAlSiN_x$, as indicated in the Fig. 35. A small amount of Cr is also seen at the sample surface after the annealing in

vacuum (Fig. 36 bottom), which is in accordance with results obtained by RBS, with the same samples. In the as deposited samples, the (Al+Si)/Cr composition ratio is 1.3 for oxynitride layer and 1.7 for nitride layer. These values increased in the annealed samples, being more significant in the vacuum annealed samples, which increased to 1.6 and 2.1, respectively. These values correspond to a small decrease of Cr content in both layers, which suggests the Cr atoms at surface diffused from nitride and oxynitride layer. The amount of Cr atoms at the surface corresponds to 5.6% of all Cr atoms in the annealed sample. The Si/Al ratio in oxide layer, is 2.0 in average, 0.5 in the oxynitride and 0.8 in the nitride layers. The difference in Si/Al and (Al+Si)/Cr composition ratios in the oxynitride and the nitride layers is mainly because of target poisoning because those layers were deposited with different nitrogen and oxygen partial pressures, being higher in oxynitride layer. This reduces the sputtering rate of different elements and this effect is higher for Al and Si when compared to Cr, because Al and Si are more reactive than Cr. The consequence is the reduction of the (Al+Si)/Cr composition ratio when passing from nitride to oxynitride. However, this difference was not seen in RBS analysis of thick single layers (Fig. 22).

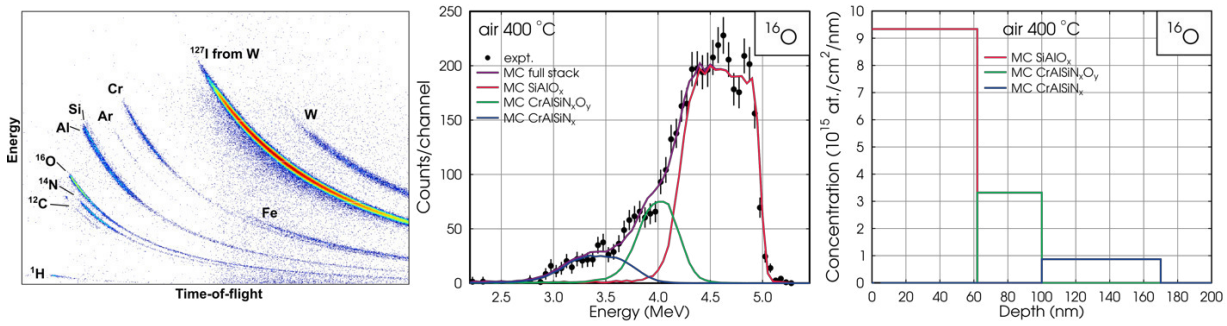

Figure 35: TOF–ERDA histogram (on the left) for the measurement of a sample annealed in air at 400 °C, experimental oxygen energy spectrum (in the middle) extracted from the measurement data and the MC simulated energy spectrum with contributions from the three absorber layers, and (on the right) the concentration profiles used in the MC simulations.

Small differences in the thicknesses of the layers were found, which can be due the positioning of the samples during the deposition. Hydrogen, carbon, and argon were observed as impurities in the three absorber layers. Their atomic concentrations were below 3% in all the layers in all the samples. Hydrogen and argon concentrations decreased significantly with the annealing treatments.

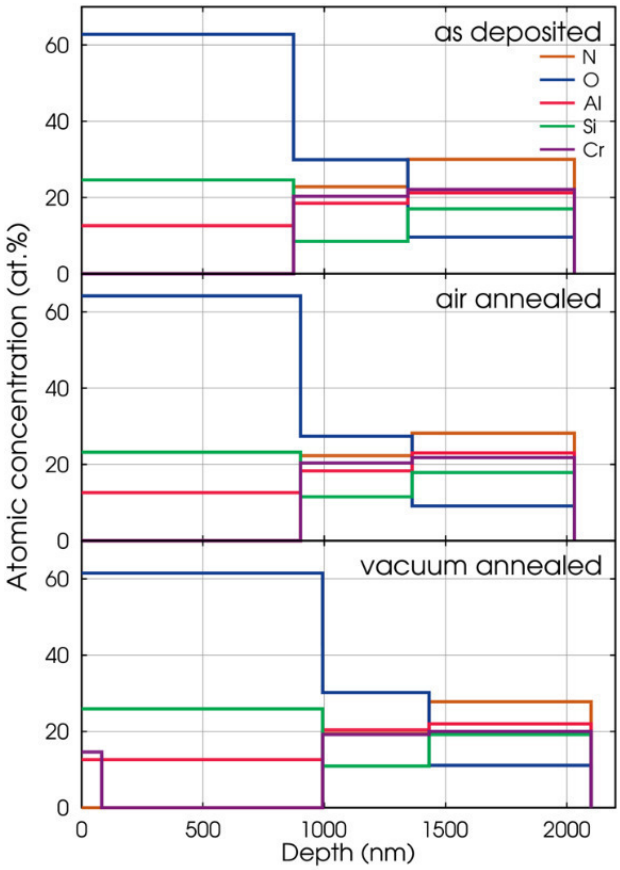

Figure 36: Elemental depth profiles determined from the TOF-ERDA measurements with MC simulations: as deposited stack (top), after air annealing at 400 ºC (middle) and after vacuum annealing at 600 ºC (bottom), both for 650 h.

4.5 Barrier layer between the back-reflector W and stainless-steel

The efficiency of any solar thermal absorber does not only depend on the high performance of selectivity, but also strongly depends on the thermal stability, corrosion resistance, oxidation resistance and elemental diffusion between layers [170]. Selectivity is the most crucial and essential condition for high performance and efficient tandems. On the other hand, the stack's high thermal stability, good diffusion barrier and high oxidation resistance after thermal ageing tests are essential factors for a long lifetime of absorber tandems for high temperature

applications, resulting in a high competition with other renewable energies, especially for electricity production [26,171]. In most cases, the efficiency of thermal absorber stacks is directly affected by the degradation of the optical properties of the absorber, which is mainly due to diffusion, corrosion resistance and oxidation of the metal back reflector layer and other metallic components. These issues become more important and present serious challenges at high temperature.

In section 4.4.2, the analysis of thermal stability of optical absorber stacks by RBS and TOF-ERDA, tungsten diffusion from the back-reflection layer towards stainless steel substrate was found. Although this did not affect the stability of optical properties with the performed annealing, in a long-term time scale, this can contribute to the coating degradation due to the possibility of the formation at the interface of the brittle intermetallic compounds (FeW and Fe_7W_6). In this section, a barrier layer between the stainless-steel substrate and the tungsten back-reflector layer was added and its influence upon the W diffusion was studied. Also, to avoid the Cr diffusion from inner layers to the coating surface, the effect of using higher nitrogen partial pressure in the deposition of nitride layer in the absorber stack is studied in detail. Additionally, the small change after the first annealing step was studied using Fourier-transform Infrared Spectroscopy (FTIR) analyses, in order to understand what is involved in those small changes, which do not happen in subsequent annealing steps.

To study these effects, four designs (A, B, C and D) were used (see details in Table 7): A is a solar absorber tandem without barrier layer between tungsten and stainless steel substrate, with structure based on stainless steel/W/$CrAlSiN_{P= 0.05\ Pa}$ /$CrAlSiON_{P= 0.07\ Pa}$ /$SiAlO_{P= 0.06\ Pa}$, B is the same as A, but with barrier layer included based on $CrAlSiN_{P= 0.11\ Pa}$, C is a multilayer stack with a nitride layer deposited with higher nitrogen partial pressure and with barrier layer included structure based on stainless steel/$CrAlSiN_{P= 0.11\ Pa}$/W/$CrAlSiN_{P= 0.08\ Pa}$/$SiAlO_{P= 0.06\ Pa}$ and D is a barrier layer with structure based on stainless steel/$CrAlSiN_{P= 0.11\ Pa}$/W/$SiAlO_{P= 0.06\ Pa}$.

Table 7: Deposition parameters of layers included in different designs (A, B, C and D).

Sample	Layer	Target	Deposition time min: s	Reactive gas partial pressure (Pa)	Target current density (mA/cm^2)
A (without barrier layer) **B** (with barrier layer)	CrAlSiN *(only in design B)*	CrAl+9 Si	2:30	N_2 0.11	6.4
	W	W	2:30	-	12.7
	CrAlSiNx	CrAl+9 Si	1: 46	N_2 0.05	6.4
	CrAlSiOyNx	CrAl+9 Si	1: 7	N_2/O_2 (85%/15%) 0.07	6.4
	SiAlOx	SiAl	1:38	O_2 0.06	6.4
C	CrAlSiN	CrAl+9 Si	2:30	N_2 0.11	6.4
	W	W	2:00	-	12.7
	CrAlSiNx	CrAl+9 Si	2:21	N_2 0.08	6.4
	SiAlOx	SiAl	1: 43	O_2 0.06	6.4
D	CrAlSiN	CrAl+9 Si	3:00	N_2 0.11	6.4
	W	W	2: 30	-	12.7
	SiAlOx	SiAl	1:30	O_2 0.06	6.4

4.5.1 Designs structure

The cross-section morphology analysis of the four samples described in Table 7 was performed by SEM, and the images are shown in Fig. 37. For clarity purpose, the different layers are identified as BL, RL, AL and AR, which are correspond to barrier, back reflector, absorption and antireflection layers, respectively. In Fig. 37a and Fig. 37b AL in comprised of 2 absorption layers, nitride and oxynitride, whereas in Fig. 37c is only the nitride layer. The tungsten layer (RL) shows a columnar growth in all designs, whereas the morphology of other layers -including the barrier layer- is not so clear.

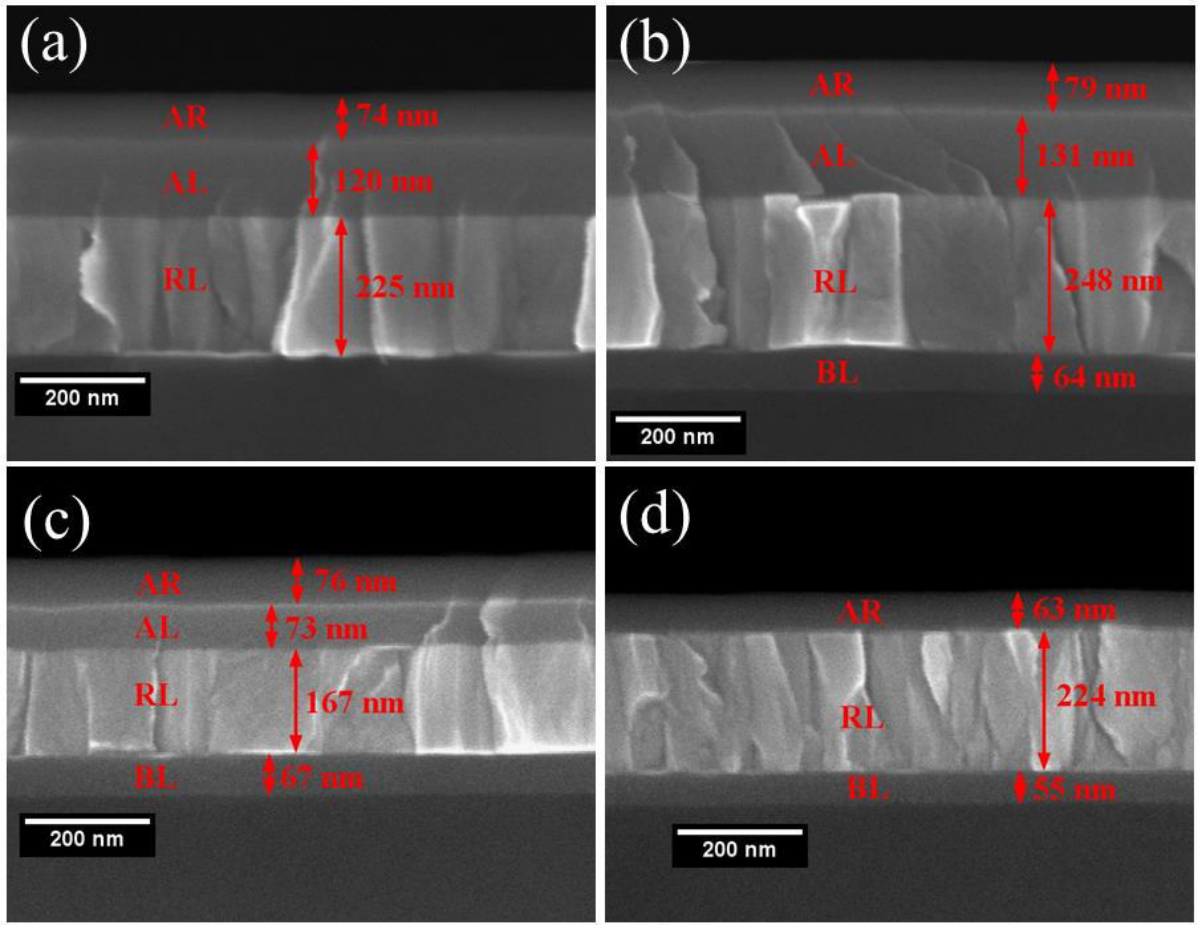

Figure 37: Cross-sectional SEM images of samples A, B, C and D showing the morphology and the thicknesses. (BL, RL, AL and AR stand for barrier, back reflector, absorption and antireflection layers, respectively). In (a) and (b) AL in comprised of 2 absorption layers, nitride and oxynitride, whereas in (c) is only the nitride layer).

So, to have more information about the structure of each sample, thicker single layers with the same coating parameters of barrier layers was analyzed by XRD, as shown in Fig. 38. The XRD spectrum of the barrier layer shows no peaks revealing its amorphous structure.

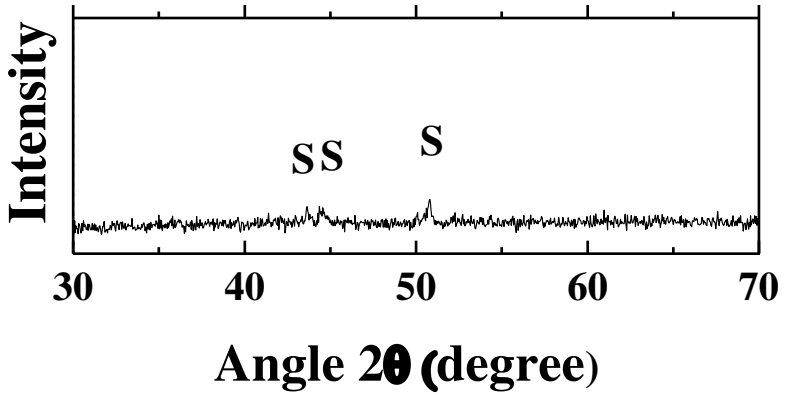

Figure 38: X-ray diffraction spectra of the single thick barrier layers deposited on stainless-steel.

4.5.2 Thermal stability

The thermal stability and elemental diffusion of stacks that were studied in previous sections are similar to sample A. The stacks revealed an excellent oxidation resistance and no elemental diffusion with the annealing in air, at 400 ºC, but in the case of vacuum annealing, at 600 ºC, a diffusion of W atoms towards the stainless-steel substrate and a diffusion of Cr atoms from absorption layers towards the surface were recorded. So, in this section we will study the effect of adding a barrier layer between the tungsten layer and the substrate (samples B, C, and D), when subjected to a vacuum annealing at 600 ºC. In addition, sample C was also used to study the influence of higher nitrogen partial pressure on the diffusion of Cr from inner layers towards the surface.

Fig. 39 shows the reflectance curves of the four samples measured in the as deposited state and after the vacuum annealing at 600 ºC. No noticeable changes are seen in the reflectance curves, solar absorptance (α_{sol}) and thermal emittance (ε) values for all samples. This implies a very good thermal and oxidation resistance for all stacks. However, small changes in the reflectance curves are observed. In all samples, a small increase of reflectance was found for wavelength higher than 3000 nm. Considering the excellent oxidation resistance and stability of the optical properties with the annealing, these small changes are likely to happen in the

back-reflector W layer. To test this, sample D was grown with the antireflection layer deposited directly over the W back reflector layer, allowing to follow any change in the oxide layer. With the absorption layers and the antireflection layer, FTIR analyses would integrate the signals from the three layers. Changes in the first annealing steps followed by steps without significant changes, with very good thermal stability, were reported in our studies and by other authors in coatings based on W-Al_2O_3 [42], Mo-SiO_2 [175] and W-SiO_2 [176] cermet composites. The changes were not similar in all cases: in most cases a small increase in reflectance in the IR range was observed, and a small decrease in the reflectance curves occurred in other cases.

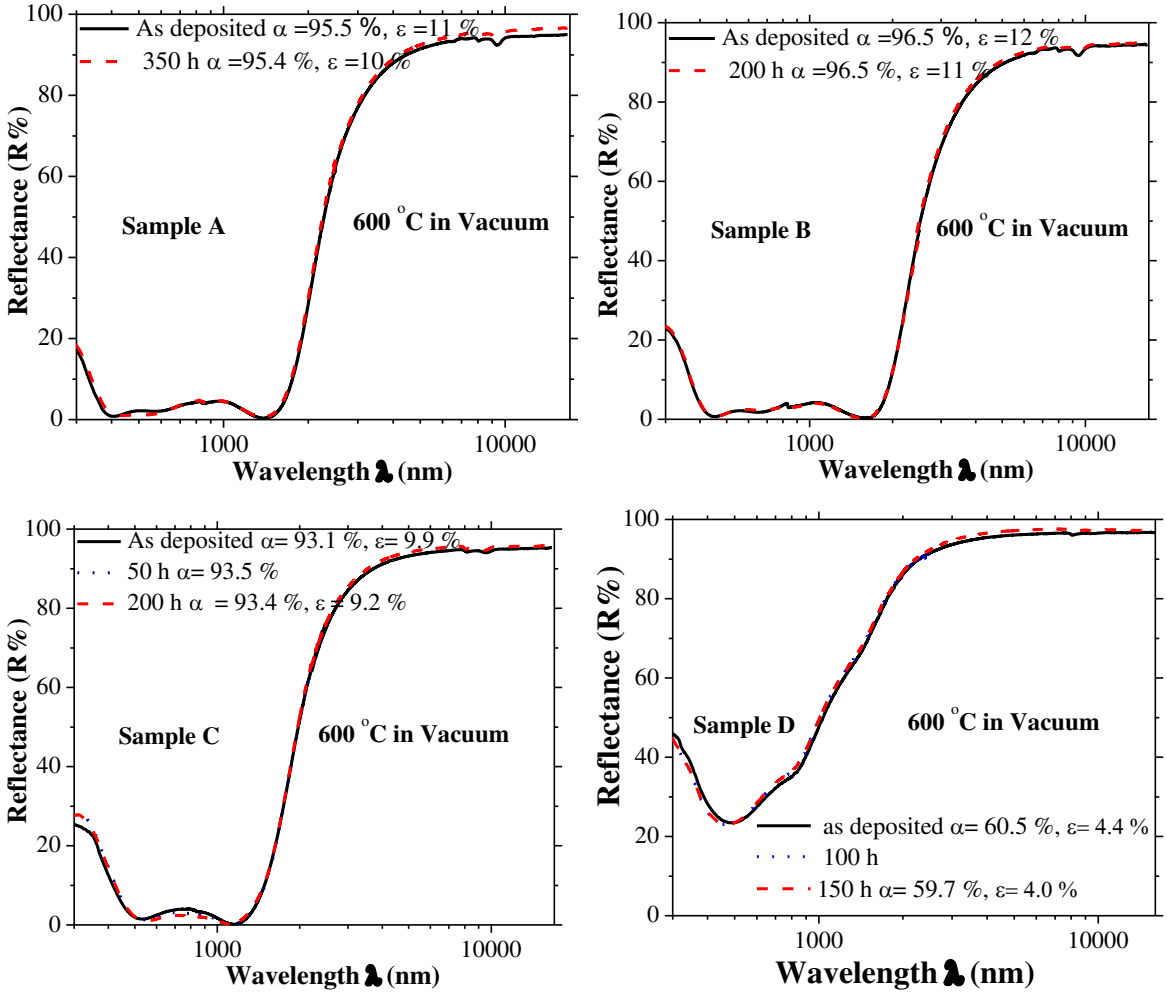

Figure 39: Reflectance curves of the four samples A, B, C and D, measured in as deposited state and after vacuum annealing at 600 ºC. The emissivity was calculated for 400 ºC.

The spectral reflectance shown in Fig. 39 exhibit some changes with the annealing in vacuum. A small increase in the reflectance was found, and this can be due to a W phase transformation during the annealing. A transformation from tungsten β- to α- phase was reported by Antonaia et al [42] with a small increase in the reflectance for wavelengths higher than 2 μm.

According to O'Keefe et al [177] differences in the oxygen concentration in the films induce variations in the transformation time and temperature for each sample. Films with higher oxygen concentration need higher temperature or longer time required for the transformation of A-15 β-W into bcc α-W. The authors reported a phase transformation at 600 ºC, with an annealing time of 1 minute, for samples with low oxygen concentration (1-2 at. % O). Samples with higher oxygen concentration transformed around 650 °C. This can be the reason of the small increase in the reflectance in IR range, which was not found for all samples. The decrease in the emissivity obtained with the vacuum annealing also supports this conclusion. The β-W phase has higher electrical resistivity than α-W phase [167,177], and the mentioned phase transformation contributes to the resistivity decrease of the W layer and consequent emissivity decrease.

The analyses of infrared bands of sample D show that the oxide layer undergoes small changes after annealing. Fig. 40 shows the experimental oblique-incidence reflectance for *p* polarized light of sample D as deposited and after vacuum annealing. The lowest frequency part of the spectra amplified in Fig. 40b, shows that after vacuum annealing the main modifications occur in the broad reflectance bands at around 850 cm^{-1} and 1240 cm^{-1}. The latter shifts to higher frequencies and the shape of the band at 850 cm^{-1} is clearly modified. These changes may be due to some local structural rearrangements, e.g., the increment of the oxidation state of some Si atoms. No important absorption is observed in the water absorption spectral region in both cases.

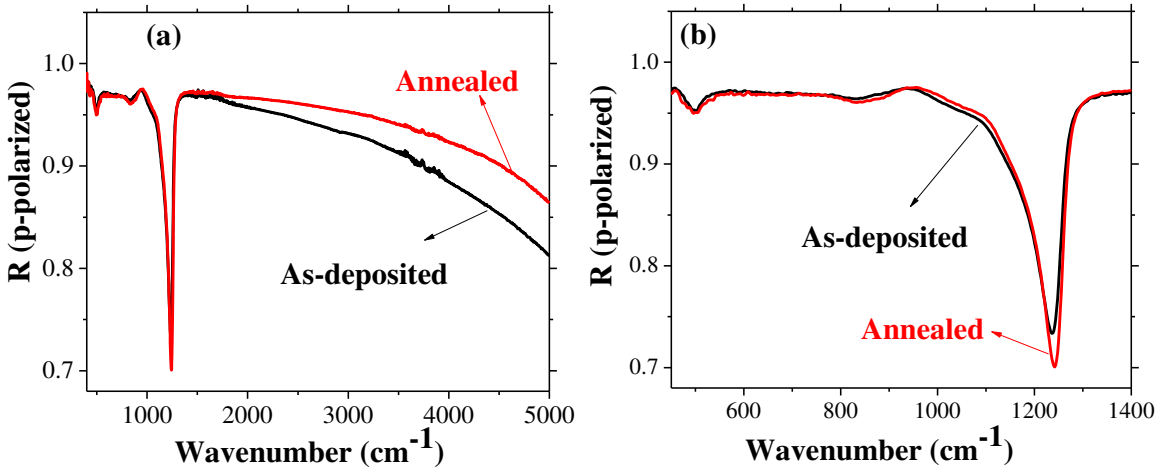

Figure 40: a) *p*-polarized reflectance spectra (angle of incidence of 45^0) of sample D as deposited and after vacuum annealing at 600 ºC. b) Amplification in the spectral range where absorption bands are present.

To access and identify the absorbing bands, the dielectric function was extracted by simulating the experimental spectra. The modelling was performed by use of Fresnel equations, considering the back medium (tungsten) as a conductor and the oxide layer as a dielectric with optical responses described by the Drude model and the factorized form of the dielectric function [178], respectively. For tungsten we used fixed parameters in the Drude model from the work of Ordal et al. [179]: plasma frequency - 51700 cm^{-1}; damping frequency - 467 cm^{-1}. For the oxide layers a high frequency dielectric constant $\varepsilon_\infty = n^2 = 2.31$ (where n is the refactive index in the visible spectral range) and the thickness of 63 nm. Fig. 41 shows the imaginary part of the dielectric function (ε_2) for both samples. The ε_2 spectra are roughly similar to the absorption spectrum of amorphous silica. The main three bands with maxima at about 480 cm^{-1}, 810 cm^{-1} and 1020 cm^{-1}/ 1036 cm^{-1}, can be attributed, respectively, to rocking (R), symmetrical stretching and asymmetrical stretching of Si-O bond [180-183]. The other minor bands are identified in Table 8. Notice that the shift of the asymmetrical stretching band, well known in the studies of amorphous silica, is usually connected to the increase of stoichiometry in SiO_x [184,185].

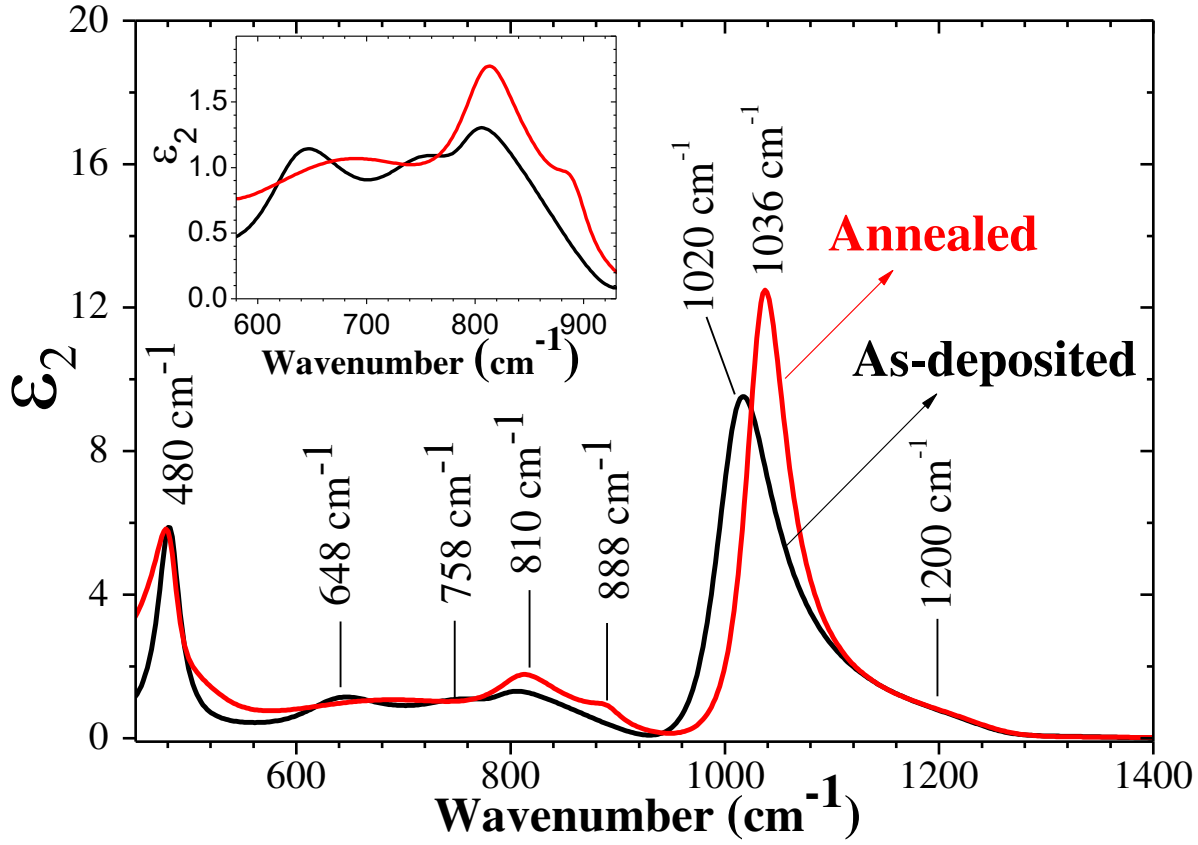

Figure 41: Imaginary part of the dielectric function of as-deposited and after vacuum annealing at 600 ºC of sample D. The inset is an amplification to show the detail of the weaker bands.

Table 8: Bands assignment of the FTIR spectra.

Band position (cm^{-1})	**Band assignment**	**Reference**
480	Si-O (rocking (R)), or Al–O–Al (bending in AlO_6)	[180-183,186,188]
648	Al–O–Al (bending in AlO_4)	[186-188]
758	T–O–T bending in mixed occupancy tetrahedral, (T = Si, Al)	[187,188]
810	Si-O symmetrical stretching	[187,188]
888	Al–O stretching in AlO_4	[187,188]
1020/1036	Si-O asymmetrical stretching (AS_1)	[180-183,186,188]
1200	Si-O asymmetrical stretching (AS_2)	[180]

Although local structural re-arrangements in the oxide layer can give rise to small changes in its high frequency refractive index, these changes will not induce the reflectance modifications with the annealing shown in Fig. 39 at the wavelength range higher than 2000 nm. For wavelengths higher than 550 nm, the refractive index of the as deposited oxide layer is 1.52. The simulated reflectance curves of the oxide layer deposited on tungsten varying the refractive index (n) of the oxide layer are shown in Fig. 42. The expected variations of n are smaller than those simulated in Fig. 42, but with these, it is easier to demonstrate the effect. The simulation shows no changes in reflectance spectra for wavelength greater than 2000 nm due to changes in the refractive index of the oxide layer.

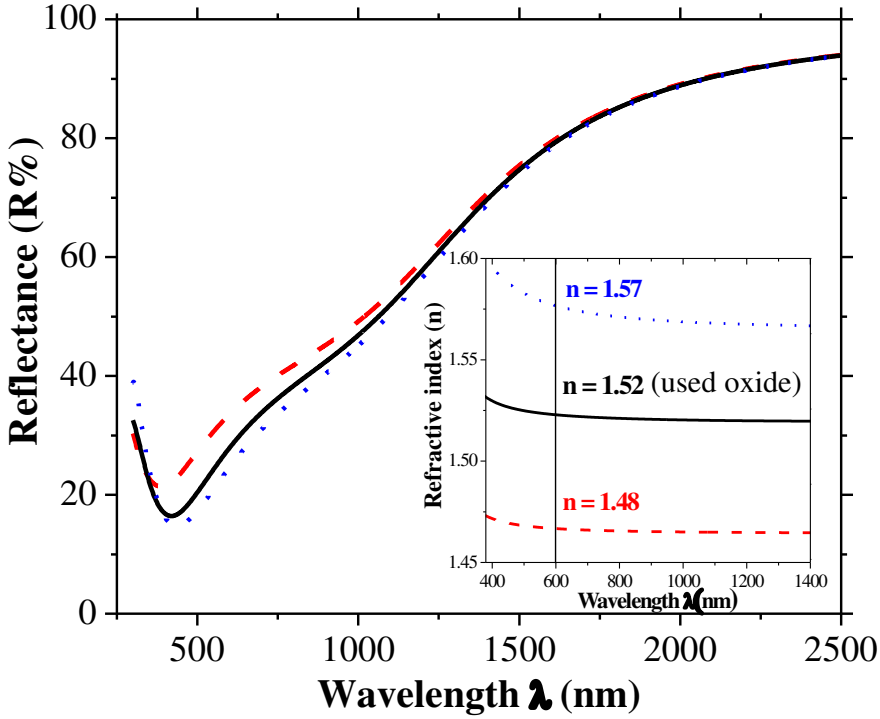

Figure 42: Simulated reflectance curves of an antireflection oxide layer on tungsten as varying its refractive index (*n*) as shown in the insert.

To obtain more information about oxidation resistance after annealing, all samples were studied by XRD and no changes were seen in the XRD spectra after annealing, as shown in Fig. 43 for sample B. No W phase transformation was clearly observed in our samples, since XRD peaks associated with both phases continue to have similar intensity before and after annealing. However, the peak located at about 37º showed a small variation of the width and

the peak located at 40º revealed a small decrease in the width and a shift to higher angles with a small increase in intensity. This can be associated with an increase of W grain size and out diffusion of contaminants from W layer, inducing also a W phase transformation contributing to the small increase of the reflectance in infrared wavelength region, as shown in Fig. 39.

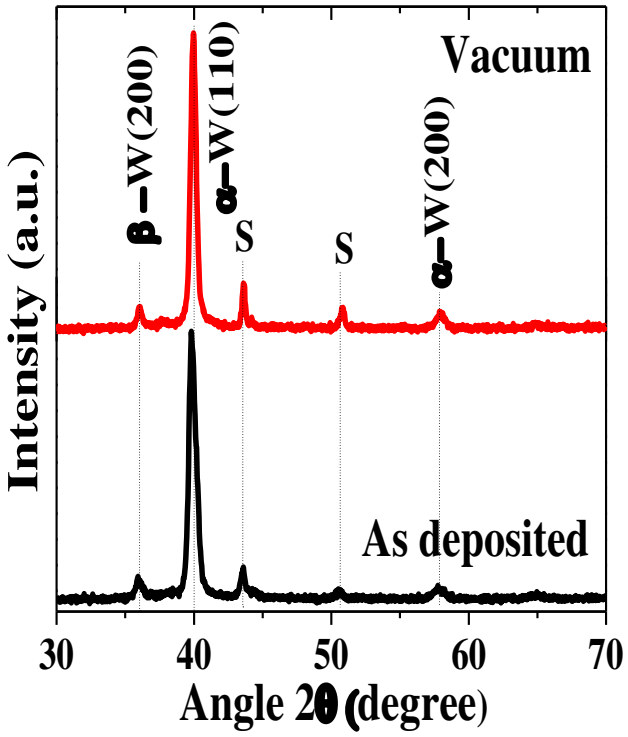

Figure 43: X-ray diffraction patterns of sample B as deposited and after vacuum annealing at 600 ºC.

The evaluation of elemental diffusion was studied by RBS. Fig. 44 shows RBS spectra of the four samples A, B, C and D deposited in the same run, namely as deposited and after vacuum annealing at 600 ºC for 200 h. Since the signals from the different elements can overlap, the composition should be determined from the front edges of the elements, which are indicated in figures for better understanding.

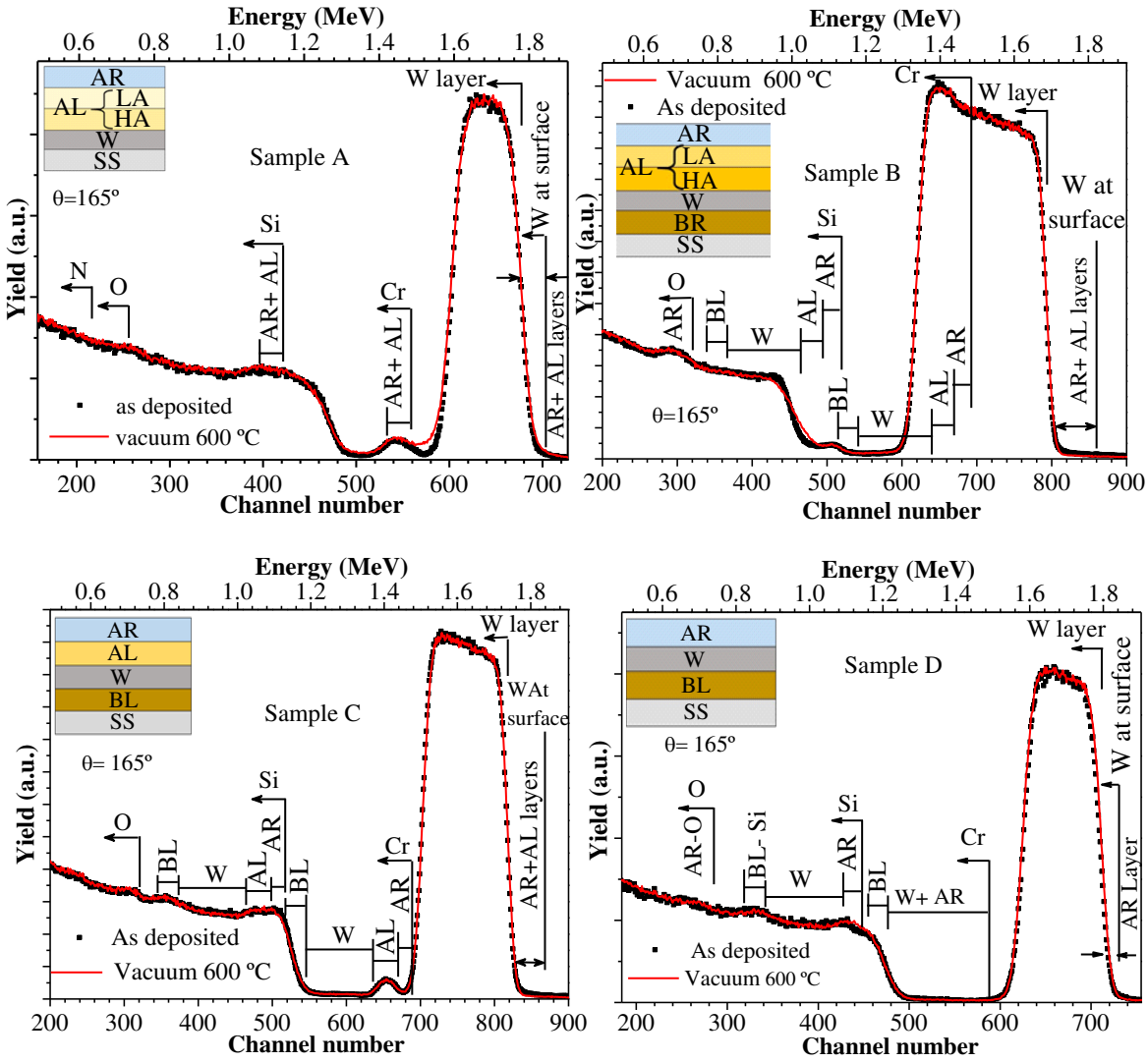

Figure 44: RBS spectra of the samples A, B, C and D as deposited and after vacuum annealing at 600 ºC for 200 h.

Sample A, which is a stack without a barrier layer, has a structure similar to the one used in the previous studies [2,3] and presented in previous sections. The analysis emphasized small differences between as deposited and annealed sample. The difference between those spectra is in the region of channel numbers 560-580, which is related with the depth profile of W element and corresponds to a tail elongation of the back side of W layer. These differences are in accordance with the diffusion of a small amount of tungsten towards the stainless-steel substrate. The general evaluation shows that no other significant changes occurred after annealing in vacuum. However, in sample B a diffusion barrier layer was added between

stainless-steel substrate and tungsten layer to avoid the W diffusion towards the substrate. As seen in the figure, there are no changes in the W depth profile after 200 h of vacuum annealing, which demonstrates the improvement of the stack diffusion without any recorded W atoms diffused towards the stainless-steel substrate. To make sure that the barrier layer works as expected, the barrier layer was also included in samples C and D and the same results were obtained. So, the barrier layer is very effective in preventing the diffusion. In the case of sample C, the stack is composed of the barrier layer, tungsten layer, nitride absorbing layer, which was deposited with higher nitrogen partial pressure, and antireflection oxide layer. This sample was used to study both diffusion cases: Cr towards the surface and W towards the substrate. In both cases, the design shows excellent thermal stability and no diffused elements between layers were recorded. Thus, using higher nitrogen partial pressure in nitride and oxynitride layers can control the diffusion of Cr atoms towards surface because the resulting films are stoichiometric and more stable.

In summary, this optical stack coating showed simultaneously high solar absorbance α_{sol} = 95.2 % and low emissivity ε= 9.8% (calculated for 400 ºC) together with high thermal stability at 400 ºC, in air, and 600 ºC in vacuum for 650 h. The addition of a $CrAlSiN_{P= 0.11\ Pa}$ barrier layer between tungsten and stainless-steel substrate proved to be a good solution to control the diffusion of W atoms towards the substrate, whereas using higher nitrogen partial pressure in the high and the low absorption layers reduce the diffusion of Cr from those layers to the surface (stoichiometric chemical composition of absorber layers is preferable).

The HA layer used in first design revealed that parts of Cr atoms are in the metallic oxidation state [124,172]. The increase of N_2 partial pressure during deposition decreases the amount of Cr in metallic oxidation state. Additionally, the presence of Si, allows the formation of a nanocomposite in the form of n-CrAlN/a-SiNx, which improves the barrier diffusion properties [173,174].

Chapter 5 Solar selective absorbing coatings based on $WSiAlN_x$/ $WSiAlO_yN_x$

In this chapter, a design based on $WSiAlN_x/WSiAlO_yN_x$ of a multilayer solar selective absorber coating for high temperature applications is presented. The optical tandem is composed of four layers, the first is a back-reflector tungsten layer, which is followed by the two absorption layers based on $WSiAlN_x/WSiAlO_yN_x$ structure for phase interference and the final layer is an antireflection layer of $SiAlO_x$. The design was conducted with the help of SCOUT software creating a multilayer model based on spectral optical constants (calculated from transmittance and reflectance spectra) of individual thin layers deposited on glass substrates. The final design shows simultaneously high solar absorptance α_{sol}= 96.0 % and low emissivity ε= 10.5% (calculated at 400 ºC) together with high thermal stability at 450 ºC, in air, and 600 ºC in vacuum for 400 h and 300 h, respectively.

In the previous chapter, a design of solar absorber tandem based on nitride/oxynitride layers ($W/CrAlSiN_x/CrAlSiO_yN_x/SiAlO_x$) were studied and fully illustrated. The final design showed simultaneously a high solar absorbance $\alpha_{sol}\approx$ 95 % and low emissivity ε= 10 % (at 400 ºC) together with high thermal stability at 450 ºC, in air, 600 ºC in vacuum, respectively. This absorber coatings also based on nitride/oxynitride structure, the only difference in this chapter is the transition metal Cr replaced with tungsten W.

Following the same procedure described in previous chapters, a set of individual layers was deposited and their spectral optical constants and thicknesses (consequently the deposition rates) were calculated. With these data the final multilayer coatings were simulated and deposition was performed with parameters obtained from simulation. Thick single layers (~μm) like those used in the multilayer stack were deposited on stainless-steel and silicon substrates to study them in detail. The antireflection layer and back-reflector tungsten layers were deposited with same parameters of previous designs, except the thicknesses.

5.1 Characterization of WSiAlNx and WSiAlOyNx single layers

5.1.1 Optical properties of single layers

A series of individual thin layers based on $WSiAlN_x$ and $WSiAlO_yN_x$ were deposited with different nitrogen and oxygen partial pressures as reactive gases for 1 min on glass. Fig. 45 presents the measured and the simulated transmittance (T) and reflectance (R) of $WSiAlN_x$ and $WSiAlOyN_x$ layers. These layers have the same behavior as $CrAlSiN_x$/$CrAlSiO_yN_x$, that they become more transparent and lose their metallic behavior with increasing of nitrogen and oxygen partial pressure, but higher partial pressure of reactive gases was needed because tungsten W is less reactive than chromium Cr. In accordance with this, the reflectance in the same wavelength range decreases with increasing nitrogen and oxygen partial pressures.

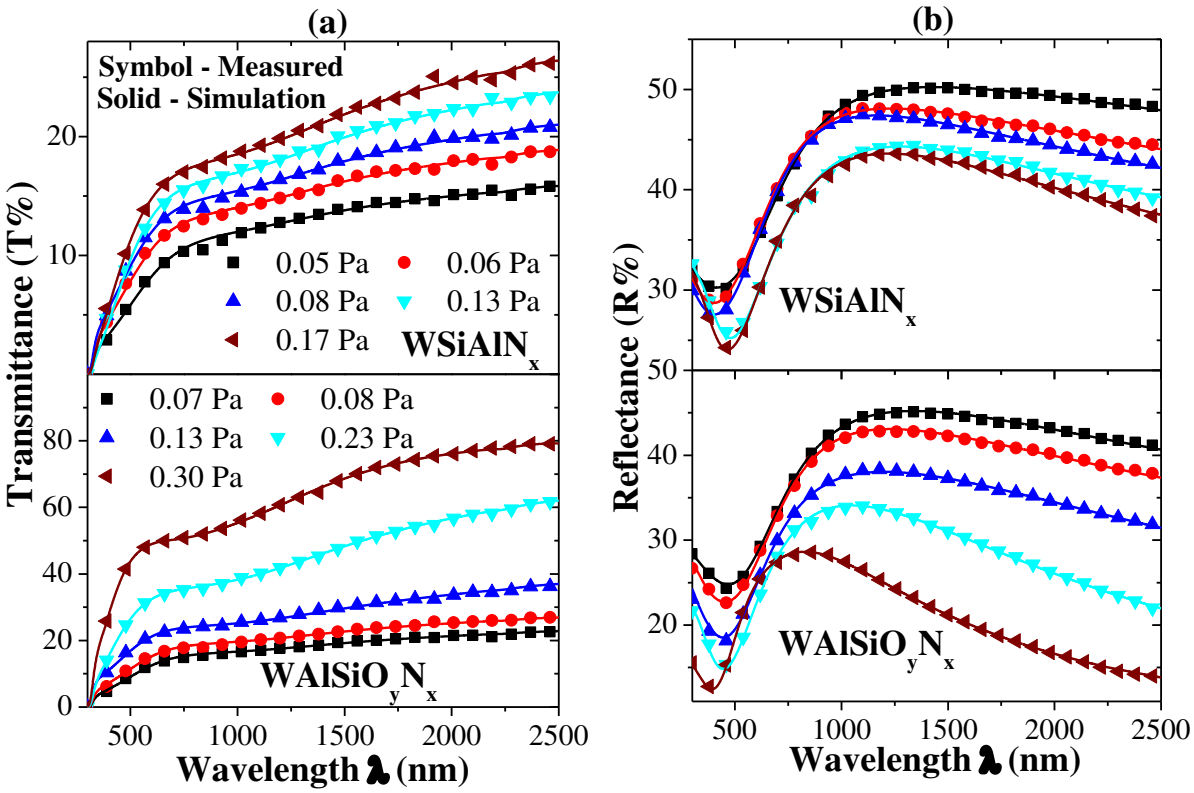

Figure 45: Measured and simulated (a) Transmittance (T) and (b) Reflectance (R) of WSiAlNx and WSiAlOyNx as a function of wavelength, prepared with increasing nitrogen and oxygen partial pressures (indicated in the legend).

Fig. 46 shows the optical constants, refractive index (n) and extinction coefficient (k), as a function of wavelength in the range of 300 – 2500 nm, obtained from modelling of the experimental T and R spectra for different partial pressures of reactive gases, as indicated in the legend of the figure. It shows the general behavior of n and k with a decrease as partial pressures of reactive gases increase for both nitride and oxynitride layers. Moreover, it is seen that the refractive indices for the $WSiAlN_x$ layers increase with the wavelength, which make these layers appropriate materials for selective absorption of solar radiation and other optical applications, because they can be used to enhance the solar absorption through the interference effect.

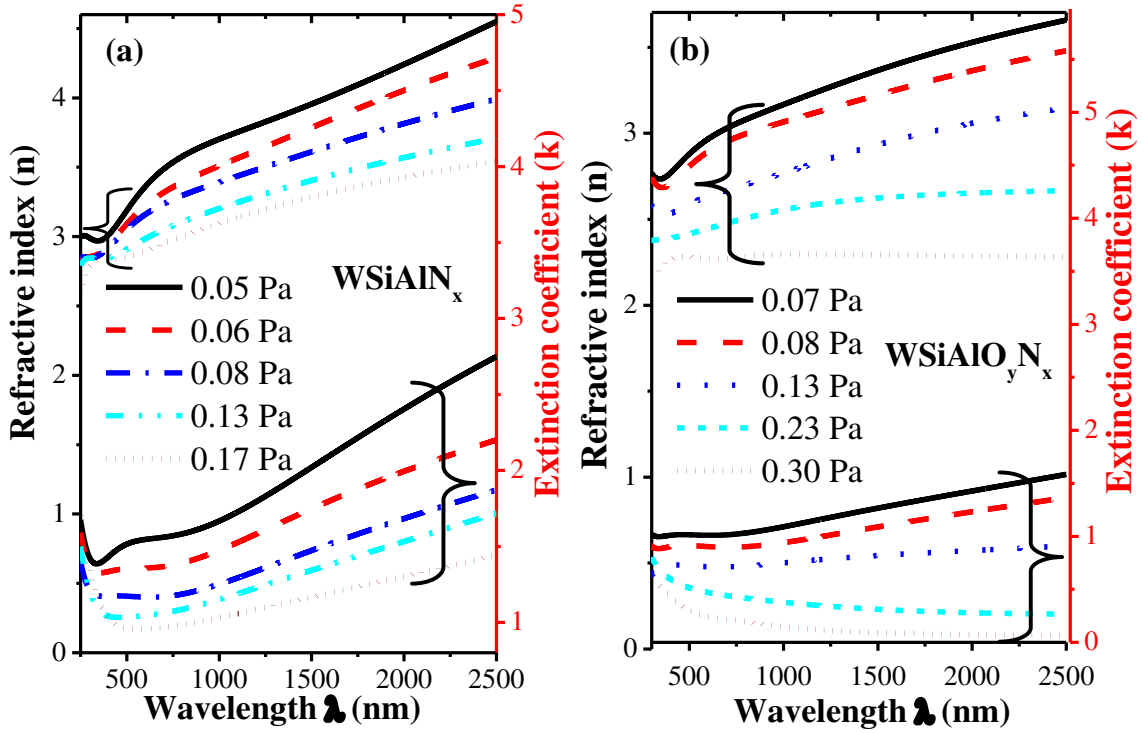

Figure 46: Refractive index (n) and extinction coefficient (k) as a function of wavelength of: (a) $WSiAlN_x$, prepared with increasing nitrogen partial pressure. (b) $WSiAlO_yN_x$ as a function of wavelength, prepared with increasing nitrogen and oxygen partial pressures.

Refractive indices and thicknesses of the bilayer structure should be chosen to obtain destructive interference at wavelengths around 0.5 μm and 1.3 μm, as introduced in ch.1. The refractive index of $WSiAlO_yN_x$ layers also shows a similar behavior with wavelength, but for high partial pressures of working gases it becomes almost constant.

As also seen in Fig. 46, $WSiAlN_x$ has higher n and k than $WSiAlO_yN_x$ because it has stronger metallic character. The increase of oxygen content leads to the oxide formation, which have lower refractive index and extinction coefficient.

5.1.2 Chemical composition of the single layers

The chemical composition of $WSiAlNx_{P= 0.17\ Pa}$ and $WSiAlOyNx_{P= 0.30\ Pa}$ thick layers, prepared in same conditions of those used in the solar thermal absorber tandem are shown in Table 9. EDS measurements were performed for two randomly chosen different positions for each sample and the average was calculated. A strong decrease of nitrogen and aluminum at% is seen in $WSiAlOyNx_{P= 0.30\ Pa}$ coating comparing with $WSiAlNx_{P= 0.17\ Pa}$. Both are related with the oxygen addition as reactive gas. The induced target poisoning has a stronger effect on Al, decreasing its sputtering yield, which resulted in a decrease on Al content. These differences explain the decrement of $WSiAlOyNx_{P= 0.30\ Pa}$ optical constants, the refractive index and extinction coefficient, n and k.

Table 9: Chemical composition of $WSiAlNx_{P= 0.17\ Pa}$ and $WSiAlOyNx_{P= 0.30\ Pa}$ thick layers obtained by EDS analysis.

Layer	N at%	O At%	Al at%	Si at%	W at%	Ar at%
$WAlSiNx_{P=0.17\ Pa}$	29	3	13	20	33	2
$WAlSiOyNx_{P=0.30\ Pa}$	25	27	3	16	29	-

To assess the chemical states and bonding information of the films, the two single layers $WSiAlNx_{P= 0.17\ Pa}$ and $WSiAlOyNx_{P= 0.30\ Pa}$ were prepared with the same parameters as those used in the multilayer stack and were analyzed by XPS. The C 1s line at 285.0 eV was used to calibrate the binding energies. The XPS spectra were analyzed with CasaXPS software [114], and all peaks were fitted using a Shirley background and GL (30) line shape. For W 4f core level, fittings were done assuming the peak doublets with spin-orbit separation (ΔE_P) $4f_{5/2}$ – $4f_{7/2}$ = 2.18 eV and with peaks intensity ratio $I_{W\ 4f_{5/2}} / I_{W\ 4f_{7/2}} = 0.75$. In some cases, it was

necessary to involve $W\ 5p_{3/2}$ at higher binding energy (BE) side of $4f_{5/2}$ with $BE_{W\ 5p_{3/2}} = BE_{W\ 4f_{7/2}} + 5.8$ and $I_{W\ 5p_{5/2}} / I_{W\ 4f_{7/2}} = 0.08$ [189].

The cores level spectra corresponding to W 4f, N 1s, Si 2p and Al 2s are shown in Fig. 47, whereas in Table 10 the Casa software fitting parameters and identification of core levels binding energies are represented. Fig. 47a shows the W 4f core level spectra, where it is evident the presence of peaks of different tungsten oxidation states. Those peaks were deconvoluted into four doublet components corresponding to W $4f_{5/2}$ and W $4f_{7/2}$. The peaks centered at 32.1, 33.1, 34.6, and 35.8 eV can be considered as W^{x+} (the intermediate W^{1+}, W^{2+} and W^{3+} oxidation states especially W-N bonds in WN or W_2N compounds [190-193]), W^{4+}, W^{5+} and W^{6+} oxidation states of W $4f_{7/2}$, respectively. The same peaks corresponding to W $4f_{5/2}$ have an energy 2.18 eV higher, the assumed doublet spin-orbit separation. In nitride sample ($WSiAlNx_{P= 0.17\ Pa}$), elemental tungsten W $4f_{7/2}$ peak (W^0) appears at 31.1 [189,194-197]. Elemental tungsten contributes to the solar radiation absorption in the visible wavelength range, which improve the absorption of whole stack.

As shown in Fig. 47b, the XPS spectra of N 1s core level can be deconvoluted into four peaks in both samples. The peaks centered at energies 397.0, 398.2 and 399.9 eV can be associated to W-N bonds, as in WN or W_2N compounds [190,191,193,198], N-Si [150,199, 200] and Si-O_3N or C = N [1,199,155], respectively. The fourth peak, at 401.9 eV, is considered as N – C = O surface contamination [1,201].

Fig. 47c shows the Si 2p core level spectra, where the sample $WSiAlNx_{P= 0.17\ Pa}$ has a contribution of three distinct components, whereas the $WSiAlOyNx_{P= 0.30\ Pa}$ sample has two components. The two samples share peaks centred at 101.4 and 102.4 eV, recognized as Si - SiN_3 [193,200] and Si – N_3O or Si(Al) – SiO_2N [1,155], respectively. The third peak that appears at 103.2 eV in sample $WSiAlNx_{P= 0.17\ Pa}$ is recognized as Si – O_3N as studied in more detail in [155].

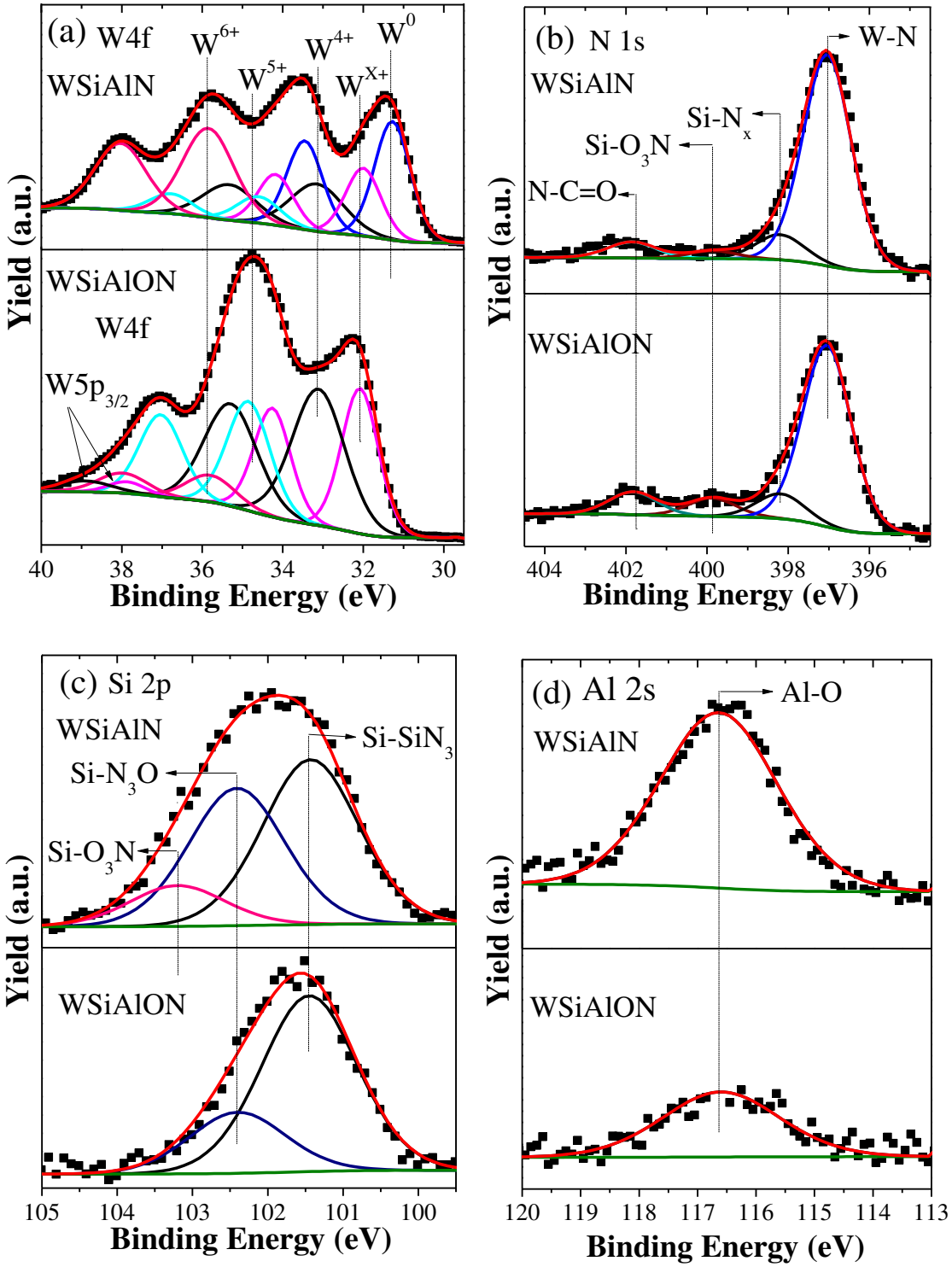

Figure 47: XPS spectra of: (a) W 4f, (b) N 1s, (c) Si 2p, (d) Al 2s core level electrons for $WSiAlN_{x\,P=0.17\,Pa}$ and $WSiAlO_yN_{x\,P=0.30\,Pa}$ single layers. The green curve represents the background correction.

The Al 2s core level was used to obtain information from Al oxidation states, instead of Al 2p, because of the overlapping between W 5s and Al 2p core levels. Fig. 47d shows the fitted Al 2s core level from both samples, which have one component centered at 116.6 eV considered as Al – O bond energy [202].

Table 10: Casa software fitting parameters and identification of core level binding energies.

Core Peak	**FWHM (eV)**	**BE (eV)** $WSiAlNx_{P= 0.17\ Pa}$	**BE (eV)** $WSiAlOyNx_{P= 0.30\ Pa}$	**Compound or oxidation state**
W $4f_{7/2}$	1.1	31.1	-	W^0
	1.1	32.1	32.1	W^{x+}
	1.6	33.1	33.1	W^{4+}
	1.3	34.6	34.8	W^{5+}
	1.5	35.8	35.8	W^{6+}
N 1s	1.4	397.0	397.0	W-N
	1.4	398.2	398.2	N -Si
	1.4	399.9	399.9	Si-O_3N, C =N
	1.4	401.9	401.8	N-C =O
Si 2p	1.5	101.4	101.5	Si - SiN_3
	1.5	102.4	102.4	Si – N_3O or Si(Al)-SiO2N
	1.5	103.2	-	Si-O_3N
Al 2s	2.4	116.6	116.6	Al-O

In terms of composition, results obtained from XPS are very consistent with EDS analyses, especially the decrement in the amount of Al, Si and N in $WSiAlOyNx_{P= 0.30\ Pa}$ sample comparing with $WSiAlNx_{P= 0.17\ Pa}$. However, more oxygen was found in $WSiAlNx_{P= 0.17\ Pa}$ sample analyzed by XPS than the reported by EDS, which is normal because XPS is a surface analysis method (~ 5 nm) and there are more chances for surface contamination.

The nitride has 27% of W atoms in the metallic oxidation state, 16 % in the W^{x+}, that can be associated to WN or W_2N, and 29 % in the W^{6+} oxidation state, whereas the oxynitride does not have W atoms in the metallic oxidation state, 29 % in the W^{x+} and only 7 % in the W^{6+} oxidation state. The amount of W^{6+} oxidation state in the nitride suggests its surface oxidation

after the deposition, whereas the atoms in the metallic state are due to the low nitrogen partial pressure. The oxynitride was obtained increasing simultaneously the partial pressures of nitrogen and oxygen (ratio 85%: 15%), which justify the increase of the amount of W atoms in the oxidation state that can be addressed to WN or W_2N, and the decrease of W atoms in the metallic oxidation state. The oxygen partial pressure is still not enough to oxidize the W atoms in a high percentage.

5.1.3 Morphology and crystalline structure of the single layers

The XRD was performed for the single layers used in the absorber stack, as shown in Fig. 48, the diffractograms of $WSiAlNx_{P= 0.17\ Pa}$, and $WSiAlOyNx_{P= 0.30\ Pa}$ layers show broad peaks, which is typical of materials with small grain size. The diffractogram of $WSiAlNx_{P= 0.17\ Pa}$ shows a broad peak centred at the position of (110) plane of W α-phase (bcc), whereas the diffractogram of $WSiAlOyNx_{P= 0.30\ Pa}$ shows a broad peak centred at the position of (200) plane of W β- phase (A15 cubic).

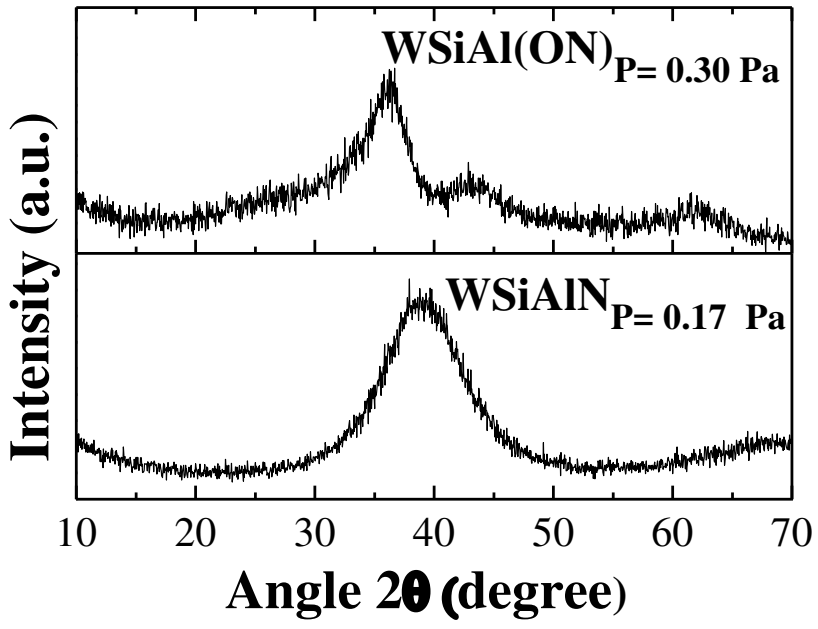

Figure 48: XRD patterns of $WSiAlNx_{P= 0.17\ Pa}$ and $WSiAlOyNx_{P= 0.30\ Pa}$ single layers deposited on stainless-steel substrate.

Indeed, SEM cross sectional micrographs of thick single layers are completely agreeing with the XRD analysis, as shown in Fig. 49, the micrographs of $WSiAlNx_{P=\ 0.17\ Pa}$ and $WSiAlOyNx_{P=\ 0.30\ Pa}$ layers show a featureless morphology.

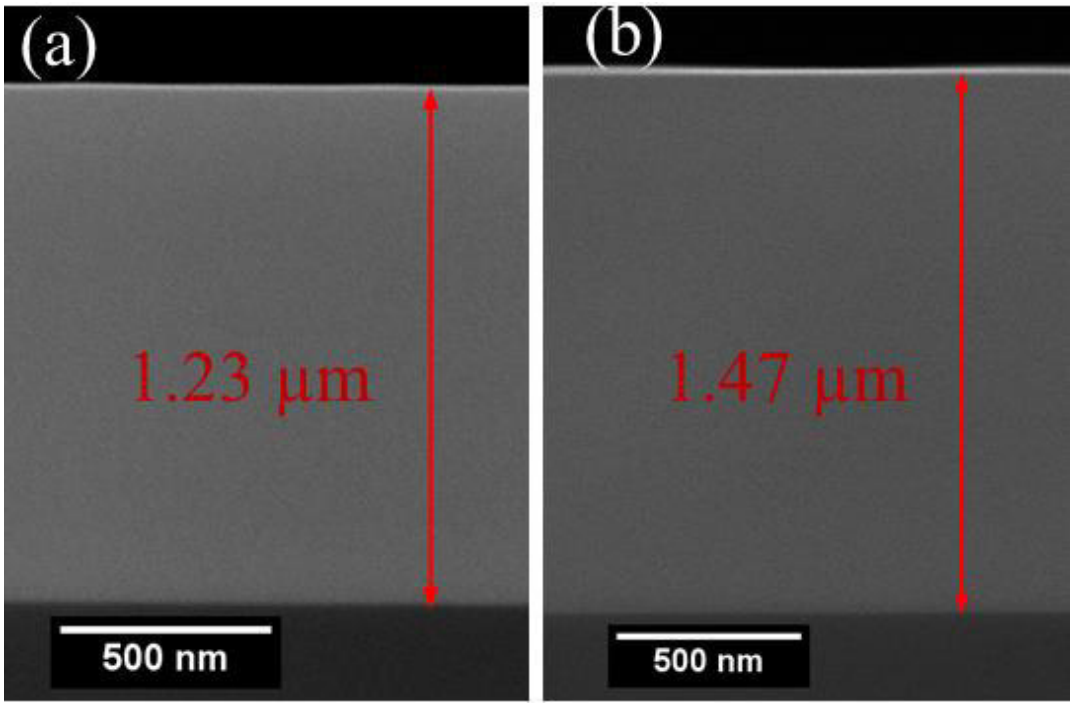

Figure 49: Cross-sectional SEM micrographs of (a) $WSiAlN_{P=\ 0.17\ Pa}$ and (b) $WSiAl\ (ON)_{P=\ 0.30\ Pa}$, thick single layers.

5.2 Design of the multilayer.

Based on the data obtained from transmittance and reflectance of individual thin single layers in the previous sections, the multilayer was designed, modelled and optimized with SCOUT software. Table 11 presents the deposition parameters.

The thickness of the simulated layers of the optical stack, together with their corresponding partial pressures are shown in the schematic diagram of Fig. 50a. The designed layers have a graded decreasing n and k from back-reflector W layer towards the antireflection layer, as requested for efficient absorbers.

Table 11: Experimental details of the multilayer stack coatings.

Layer	Target	Deposition time min: s	Working pressure (Pa)	Reactive gas Partial pressure (Pa)	Target current density (mA/cm^2)
Tungsten	W	2:30	0.37	-	12.7
WSiAlNx	W+9Al+9 Si*	0:42	0.41	N_2 0.17	6.4
WSiAlOyNx	W+9Al + 9 Si	0:32	0.45	N_2 - O_2 (85% 15%) 0.30	6.4
SiAlOx	Si80Al20	1:36	0.37	O_2 0.06	6.4

* 9 silicon pellets with a diameter of 10 mm and 9 squares of aluminum pieces with 1 cm ×1 cm distributed uniformly on the W target erosion zone

In Fig. 50b, it is shown how the whole stack was optimized by the addition of layers one by one. It is obvious that addition of multilayers results in an improvement upon the reflectance curve of the stack and upon the solar selectivity. This ensures that multilayers are adequate and essential for more efficient solar absorbers.

As shown in Fig. 50a, the optical stack is composed of four layers, the first is a back-reflector tungsten layer, that is followed by the two absorption layers based on $WAlSiN_x$/ $WAlSiO_yN_x$ structure for phase interference. The final layer is an antireflection layer, which consists of $SiAlO_x$. The total simulated thickness of the whole multilayer's absorber ($W/WAlSiN_x/WAlSiO_yN_x/SiAlO_x$) is ~ 372 nm. Fig. 50b also displays the reflectance curve of as deposited sample, that shows a good agreement with simulation, as expected. The final design shows simultaneously high solar absorptance, in average α_{sol}= 96.2 %, and low emissivity, ε= 8.0 % (measured by emissometer at 80 ºC) and 10.5% calculated for 400 ºC using the IR reflectance in equation (2.41). Moreover, Fig. 51 shows a cross-sectional SEM micrograph of the optical stack, deposited on silicon substrate. W layer shows a typical morphology of a columnar growth type, whereas the remaining layers reveal a featureless morphology that completely agrees with XRD analysis of single layers. The total SEM

thickness of as deposited tandem is about 367 nm, which is very close to simulated thickness taking into the account the measurements error.

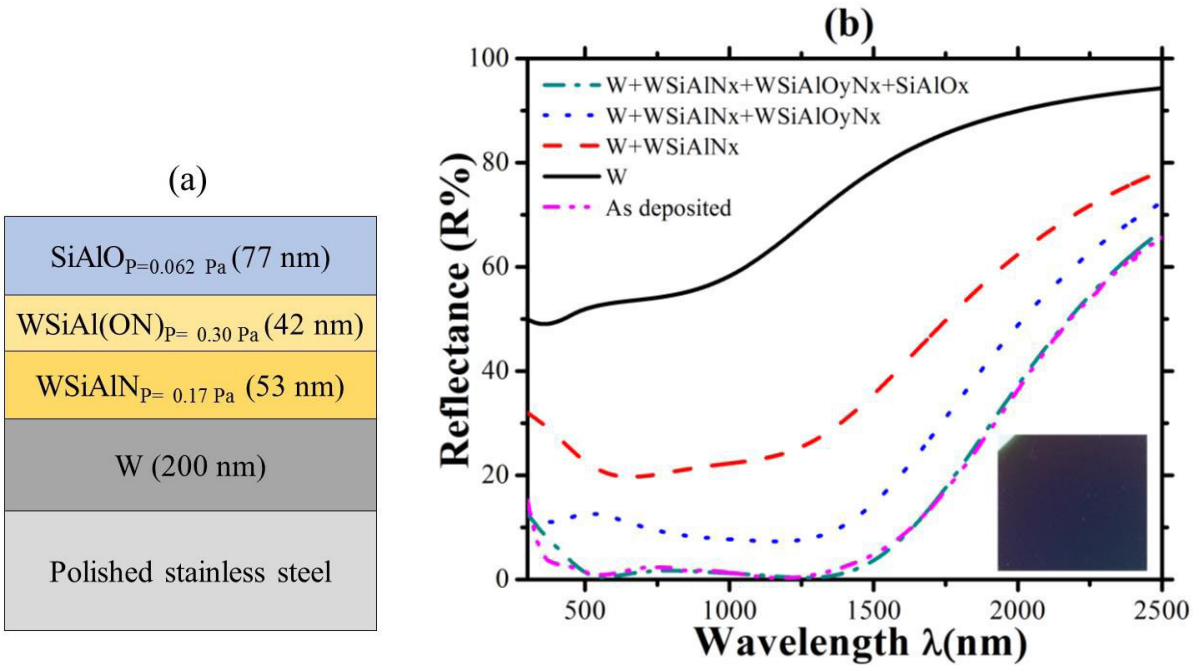

Figure 50: (a) Schematic diagram of the simulated multilayer as obtained by SCOUT. (b) Simulated and experimental reflectance curves of the absorber design.

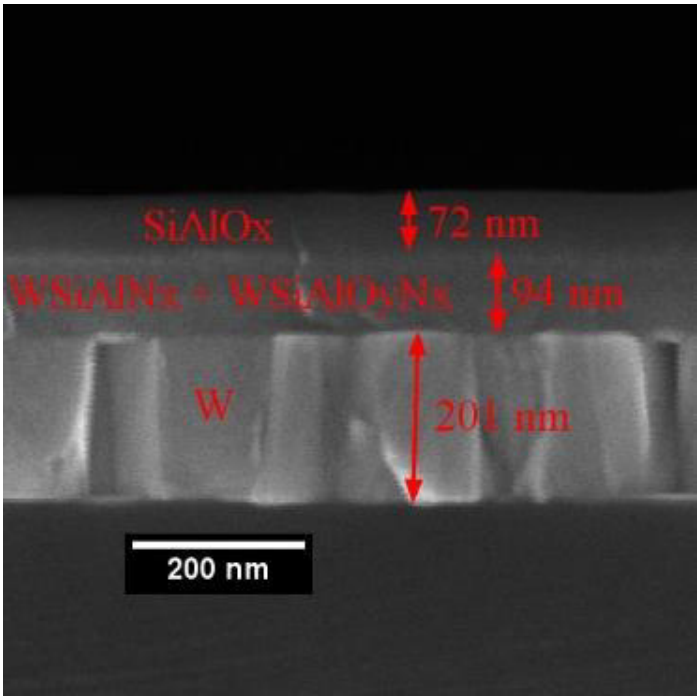

Figure 51: Cross-sectional SEM micrograph of the optical stack, deposited on silicon substrate.

5.2.1 Thermal Stability

For oxidation resistance and long-term thermal stability, the solar absorber tandem was subjected to annealing tests in air, at 450 ºC, and in vacuum, at 600 ºC, for 400 h and 300 h, respectively. Then, solar absorptance (α_{sol}) and thermal emittance (ε) were calculated, after each annealing step, from the reflectance curves by methods described in section 3.4. Fig. 52a represents the reflectance curves of as deposited sample, after 150 h and after 400 h of air annealing. The solar absorptance and the thermal emittance at 400 °C after each step are indicated in the legend of the figure.

No notable changes were seen in the reflectance curve, solar absorptance and thermal emittance values. This means that the absorber stack showed a very good thermal stability when subjected to air annealing. On the other hand, the measurements of the optical constants after vacuum annealing was performed for 150 h, 200 h and 300 h, as shown in Fig. 52b, the results confirm that the stack shows a very good thermal stability after vacuum annealing. These results are very similar to those obtained with coating based on AlSiOx:W cermets with high (HA) and low (LA) metal volume fraction (W/$AlSiO_x$:W(HA)/$AlSiO_x$:W(LA)/$AlSiO_x$) [5] as will see in the next chapter.

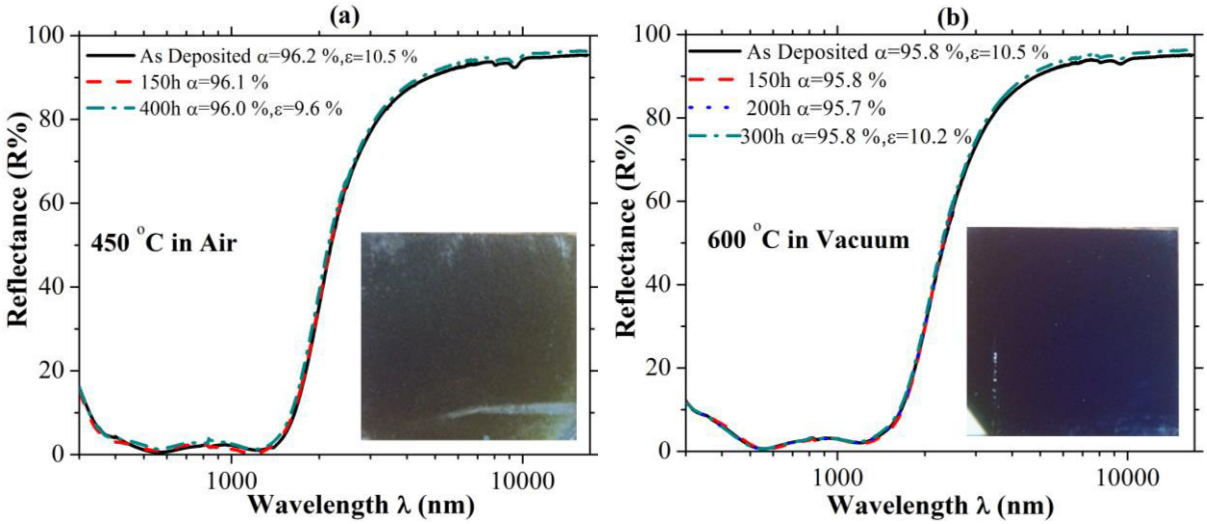

Figure 52: Reflectance of as deposited optical stack and after (a) air thermal annealing at 400 ºC (b) vacuum thermal annealing at 600 ºC, with measured value of solar absorptance (α) and thermal emittance (ε) (calculated for 400 ºC).

The annealing in vacuum was performed at 600 ºC, whereas the air annealing was at 400 ºC. The absorption nitride layers had a higher fraction of W atoms at metallic oxidation state, whereas the oxynitride layer has a big fraction of the W atoms with W-N bonds. In these samples the W content in absorption layers is around 30 at. %. This showing that oxide and oxynitride layers protect the W in nitride and antireflection layers against oxidation, which justifies the high thermal stability.

In order to analyse if the tandem structure had been not changed or affected by oxidation after thermal treatment, the three samples (as deposited, after air and vacuum annealing) were analysed by XRD. Fig. 53 represents the diffractograms of the three samples. As it is shown in the figure, results are completely agreeing with the one obtained from thick single layers that have a poor crystallinity, except the W layer, that is polycrystalline. However, there are no significant changes after the annealing, except small differences in the stainless-steel peaks and in the intensity of W peaks. This confirms that the stack showed a good resistance against oxidation and it has a good thermal stability after annealing in air and vacuum at 450 ºC and 600 ºC, respectively.

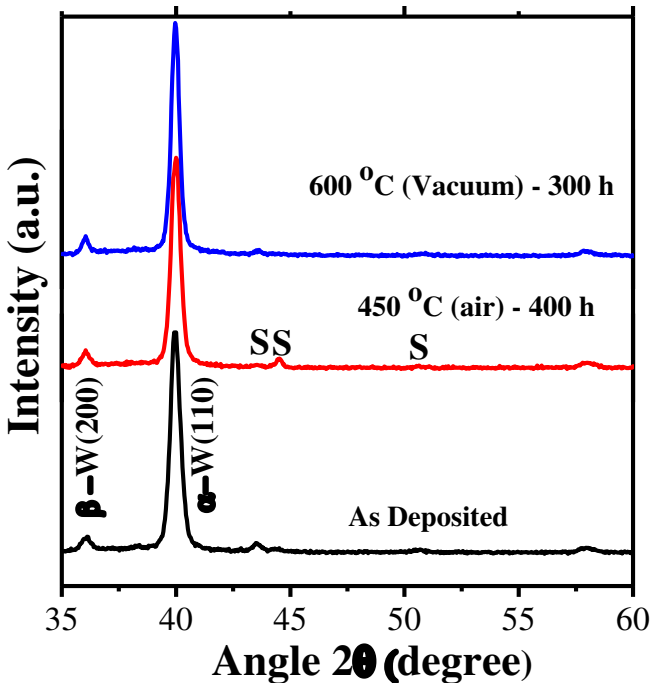

Figure 53: X-ray diffraction of as deposited thermal absorber and after thermal annealing, as indicated in the legend.

In summary, a tandem coating for selective absorption of solar radiation for high temperature applications was fabricated by DC magnetron sputtering method. It is a multilayer based on four layers of structure ($W/WSiAlN_x/WSiAlO_yN_x/SiAlO_x$), as back reflector/high absorber/low absorber/ antireflection layer, respectively. Thicker single layers of $WSiAlN_x$ and $WSiAlO_yN_x$ with the same coating parameters as those in the optical stack were used to study the structural, optical and chemical properties. These layers become more transparent and lose their metallic behavior with increasing nitrogen and oxygen partial pressures as reactive gases. As a result, the optical constants (refractive index and extinction coefficient, n and k) decreased. $WSiAlN_x$ has higher amount of Al, Si, N and W than $WSiAlO_yN_x$ as reported by EDS and XPS analysis. Moreover, XPS analysis prove the existence of tungsten in metal state, that may improve the solar absorptance of the tandem because of its contribution to the absorption in the visible solar radiation wavelength. Based on data from these single layers, the tandem was initially simulated by the SCOUT software. The total thickness of the stack is ~ 367 nm as measured by SEM. Experimental design shows simultaneously high average solar absorptance, α_{sol} =96.0%, and low emissivity, ε= 10.5 % (calculated for 400 ºC), together with high thermal stability at 450 ºC, in air and at 600 ºC, in vacuum, for 400 h and 300 h, respectively. After several steps of thermal annealing in vacuum and air annealing, the reflectance curve of the stack showed an excellent stability of the selectivity (α/ε) values, and there are no significant changes on the tandem reflectance curves. In most cases, the thermal emissivity improved a bit, which implies that the W back reflector layer maintained its reflectivity, meaning that it is well protected by the outermost layers. Finally, the $WSiAlN_x$, $WSiAlO_yN_x$ layers show a featureless morphology, which is in accordance with the XRD amorphous like structure.

Chapter 6 Solar selective absorbing coatings based on $AlSiO_x$:W cermets

In this chapter a design based on $AlSiO_x$:W cermets of a multilayer solar selective absorber coating is presented. The strategy to design and to deposit this multilayer is different of those presented in previous chapters, and the design is an example of the second group of thermal selective solar absorbers described in the introduction. The optical tandem is composed of four layers structure, W/$AlSiO_x$:W(HA)/$AlSiO_x$:W(LA)/$AlSiO_x$, and was deposited on stainless-steel substrates, in the rotation mode, using the magnetron sputtering deposition method. The numerical calculations were performed to simulate the transmittance and the reflectance of different single layers with different metal volume fraction cermets and the film thickness, in the same way as previous designs, and used to calculate the respective dielectric functions. These were used to design the multilayer. The results indicate that this film structure has a good spectral selective property that is suitable for solar thermal applications, with the coatings exhibiting a solar absorptance of 94%-95.5% and emissivity of 10%-14% (at 400 ºC).

6.1 Characterization of the single layers

6.1.1 Optical properties of the Single layers

The tungsten (W) layer is similar to the one studied previously. For the absorbing layers, different cermet $AlSiO_x$:W layers were deposited on glass substrates by varying the applied current to the W target. Optical spectroscopy in both transmittance and reflectance modes was used to characterize the optical properties of the films. The increase in W content in the films led to the expected gradual decrease of the transmittance and consequently to an increase in

the reflectance, which is consistent with the increasing metallic character. Fig. 54 depicts the optical transmittance and reflectance data for representative $AlSiO_x$:W layers prepared with increasing W target current, as indicated in the legend of Fig. 54. By varying the W target current between 0 and 0.7 A it was possible to obtain a wide range of reflectance and transmittance values (and consequently spectral optical constants), from which it is possible to select the layers with adequate spectral optical constants and construct the desired optical stack.

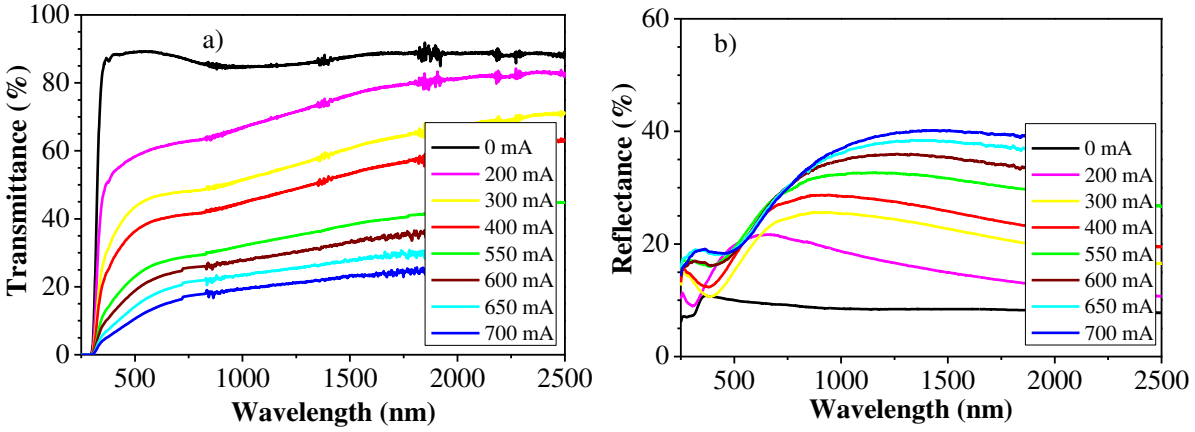

Figure 54: Reflectance (a) and Transmittance (b) of different cermet $AlSiO_x$: W layers deposited on glass, prepared with a substrate holder rotation speed of 15 rpm and with varying W target current.

The refractive index (n) and the extinction coefficient (k) are plotted in Fig. 55 as a function of the wavelength, for the same samples shown in Fig. 54 (substrate holder rotation speed of 15 rpm).

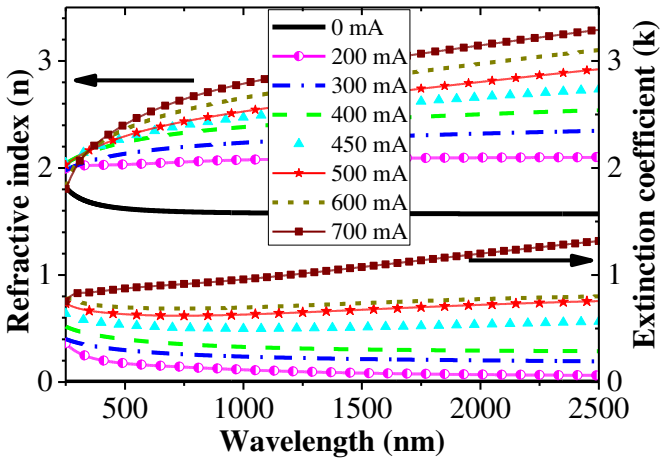

Figure 55: Refractive index (n) and extinction coefficient (k) as a function of wavelength for $AlSiO_x$: W layers prepared with a substrate holder rotation speed of 15 rpm and different W target currents.

As expected, the refractive index and extinction coefficient increase with W content due to the increase of the metallic character. The thicknesses of these films were obtained from SCOUT simulation and they are ranged from 70 to 91 nm. The deposition rate of $AlSiO_x$ in rotation mode is 11.4 nm/min and addition of W lead to increase it, reaching 32 nm/min for a W target current of 0.75 A. The deposition rate as a function of current applied to W target is shown in Fig. 56. The thicknesses were calculated from transmittance and reflectance modelling.

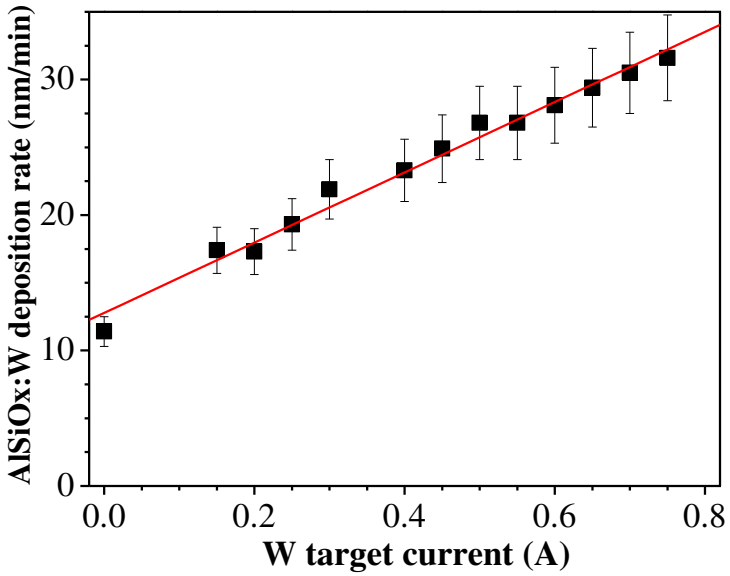

Figure 56: AlSiOx:W deposition rate as a function of the current applied to W target.

The deposition rate increases linearly with the W target current. Similar analysis was performed for samples prepared with rotation speed of 7 rpm, being obtained similar deposition rates, fixing the other deposition parameters. However, the layers prepared with 7 rpm were always less transparent than those prepared with 15 rpm and they have a higher extinction coefficient than the prepared with 15 rpm, which also means that they will have a higher absorptance. As an example, in Fig. 57 are represented the spectral optical constants of two samples deposited with same parameters, varying only the rotation speed, where is shown a significative difference on extinction coefficient. This happens systematically with samples prepared with a constant W target current where the one prepared with a lower rotation speed has always a higher extinction coefficient. With lower rotation speed it is deposited a higher

W thickness in each cycle and results in a sample with a higher extinction coefficient; which is also related with less W atoms in the W^{6+} and W^{5+} oxidation states and more in the W^{4+} oxidation state as will show in the next section. Films with tungsten atoms in the W^{6+} oxidation state are transparent and have a low contribution for the solar radiation absorption. However, tungsten atoms in the W^{5+} and W^{4+} oxidation states already contribute substantially for the solar radiation absorption. As already reported, WOy substoichiometric films become coloured for $y < 2.75$ [189,203], which was justified by the presence of W^{5+} and W^{4+} oxidation states. Thus, the films prepared with lower rotation speed have higher extinction coefficient not only due to the increasing number of tungsten atoms at W^{0} oxidation state, but also to the higher amount of tungsten atoms in the W^{5+} and W^{4+} oxidation states.

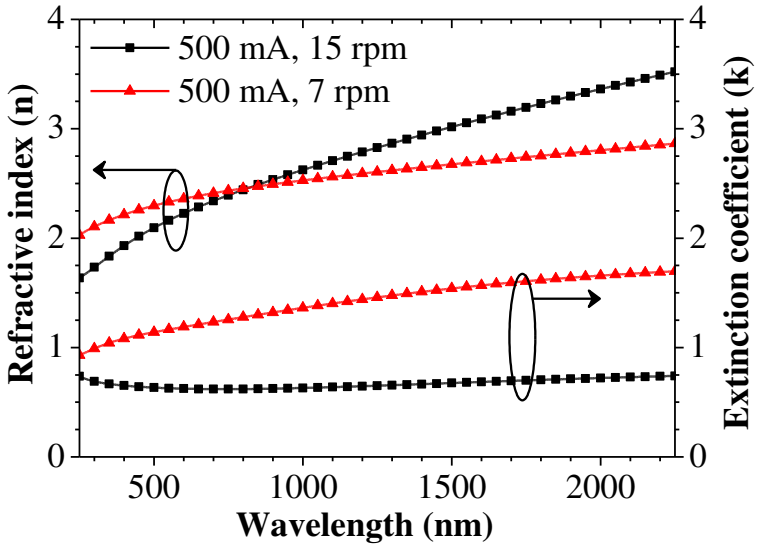

Figure 57: The spectral optical constants of two samples deposited with same parameters, varying only the rotation speed.

6.1.2 The oxidation of W atoms

In order to assess the chemical composition, chemical state and bonding information of the films, two single layers were prepared and analyzed by XPS. These two layers, D1 and D2, were deposited with applied currents of 0.75 A and 0.5 A on W and Al (Si) targets, respectively, with the same argon and oxygen flow rates, but with different rotation speed, 15 rpm for D1 and 7 rpm for D2.

The core level spectra corresponding to W 4f are shown in Fig. 58. The tungsten is present in both metallic and oxidized states, for both samples; the deconvolution of the peaks demonstrates the different oxidation states of tungsten, which are presented in Table 12. The peaks appearing at 30.5 eV and 30.6 eV binding energies can be associated with metallic tungsten in D1 and D2 samples, respectively [189,204]. The peaks at 36 eV, 34.8 eV and 33.1 eV can be related to the oxidation states of W^{6+}, W^{5+} and W^{4+}, respectively, [189,196,197,205] and the peaks at 31.6-31.7 eV can be attributed to the intermediate W^{+1}, W^{2+} and W^{3+} oxidation states commonly known as the W^{x+} oxidation state [189,205]. The latter oxidation state (W^{x+}) can be explained by tungsten ions bonded to oxygen and tungsten ions. The peak associated with W^{6+} oxidation state can have a small contribution coming from the W $5p_{3/2}$ peak associated with W^0 oxidation state because the binding energy of W $5p_{3/2}$ peak is 5.5 eV above that of the W $4f_{7/2}$ peak. However, if any, should be similar for both samples.

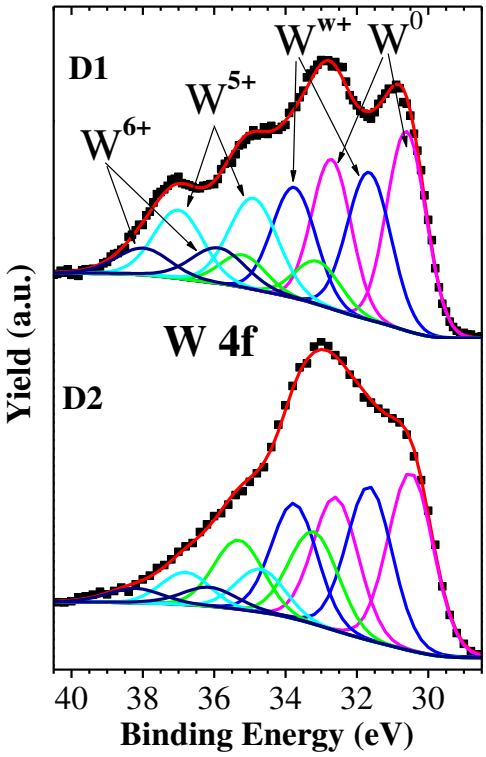

Figure 58: XPS spectra of W 4f electrons for analyzed samples. D1 was prepared with 15 rpm and D2 with 7 rpm.

These results show that, in both samples, about one third of W atoms are in the W^0 oxidation state, another third in the W^{x+} oxidation state and the last third in the W^{4+}, W^{5+} and W^{6+} oxidation states. Sample D1 has 29.3% of the W atoms at higher oxidation states (W^{6+} and W^{5+}), while the sample prepared with lower rotation speed (D2) has only 14.0 % of the W atoms at those oxidation states.

Table 12: Identification of core level binding energies of W 4f core level of analyzed samples.

Sample	D1		D2		
Core level	BE (eV)	Peak area	BE (eV)	Peak area	Oxidation state
W 4f $_{7/2}$	30.6	33.9%	30.5	35.2%	W^0
	31.7	28.2%	31.6	31.2%	W^{x+}
	33.1	8.6%	33.2	19.6%	W^{4+}
	34.9	20.3%	34.6	9.1%	W^{5+}
	35.9	9.0%	36.3	4.9%	W^{6+}

6.1.3 Structural properties of the single layers

$AlSiO_x$:W thick layers were deposited and subsequently analysed by X-ray diffraction. In Fig. 59 are represented the XRD patterns for layers prepared with a rotation speed of 15 rpm (Fig. 59a) and of 7 rpm (Fig. 59b) with different W target currents, as indicated in the legend. The vertical scale is the same in both graphs. In all cases a broad peak is present, around $2\theta=40^o$, which could be assigned to (110) planes of bcc W lattice.

The intensity of the broad peak increases with tungsten current, which is obviously correlated with the tungsten volume fraction. However, the ~7º FWHM indicates that W, SiO_2 and Al_2O_3 phases are amorphous. Using the Scherrer equation and the mentioned width of W peak, a grain size of 1.2 nm was obtained. Similar behaviour was found for W-Al_2O_3 cermet layers deposited by rf sputtering [42]. The other peaks, referred by S, correspond to the stainless-steel substrate.

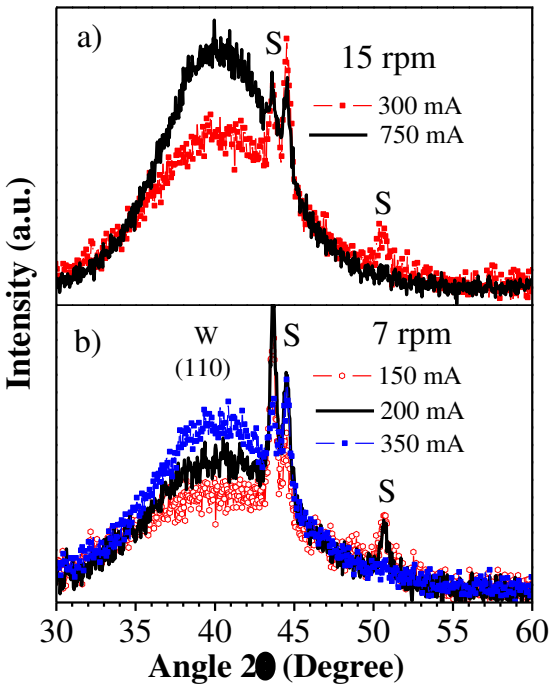

Figure 59: XRD diffractograms performed with an incidence angle of 3º for $AlSiO_x$: W single layers prepared with different W target currents (indicated in the legend) and rotation speeds: (a) 15 rpm (b) 7 rpm. The peaks referred by S, correspond to the stainless-steel substrate.

6.2 Development of the optical stacks

A set of $AlSiO_x$:W single layers for each rotation speed (7 and 15 rpm) with varying the W target current was used to elaborate the optimization of the optical stack. The respective spectral optical constants were used to design the structure of the multilayers, varying the materials and its thicknesses and simulating its reflectance. The multilayers were built with 4 layers, as schematically represented in Fig 60.

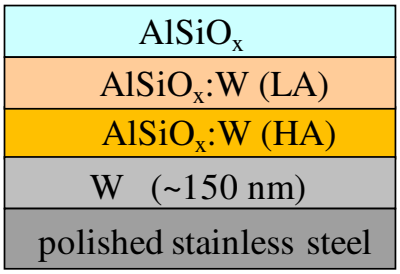

Figure 60: Sketch of multilayer coatings based on $AlSiO_x$:W cermets.

In Table 13 are presented the parameters associated with the single layers used in each multilayer coating stack, being identified by the W target current, the thicknesses and deposition time for the three outermost layers. The first three coatings (A, B and C) were prepared with a rotation speed mode of 15 rpm, while in the fourth (sample D) the rotation speed was set to 7 rpm. The spectral reflectance of these coatings is shown in Fig. 61. The solar absorptance and thermal emittance (at 400 ºC) are shown in the legend of the figure. The solar absorptance and emissivity (at 400 ºC) are both higher for sample A, being related with the higher thicknesses of HA and LA layers. In sample D, the step on the wavelength scale is shifted to lower wavelengths, which impacts in a reduction in both, solar absorptance and emissivity at 400 ºC.

Table 13:Parameters of single layers used in the multilayers, currents on W target, thicknesses and deposition times.

Sample	Current on W target [mA]	Thicknesses [nm]	Deposition time [s]
A	750 / 200 / 0	69 / 30 / 76	130 / 105 / 400
B	750 / 300 / 0	58 / 33 / 69	110 / 90 / 363
C	750 / 300 / 0	53 / 33 / 62	100 / 90 / 326
D	350 / 200 / 0	57 / 30 / 90	149 / 83 / 474

The different coatings, deposited on polished stainless-steel substrates, were analysed by SEM. In Fig.62 are shown the micrographs obtained for samples B (Fig. 62a) and D (Fig. 62b), with the indication of the constituent layers of the optical stack and the respective thicknesses.

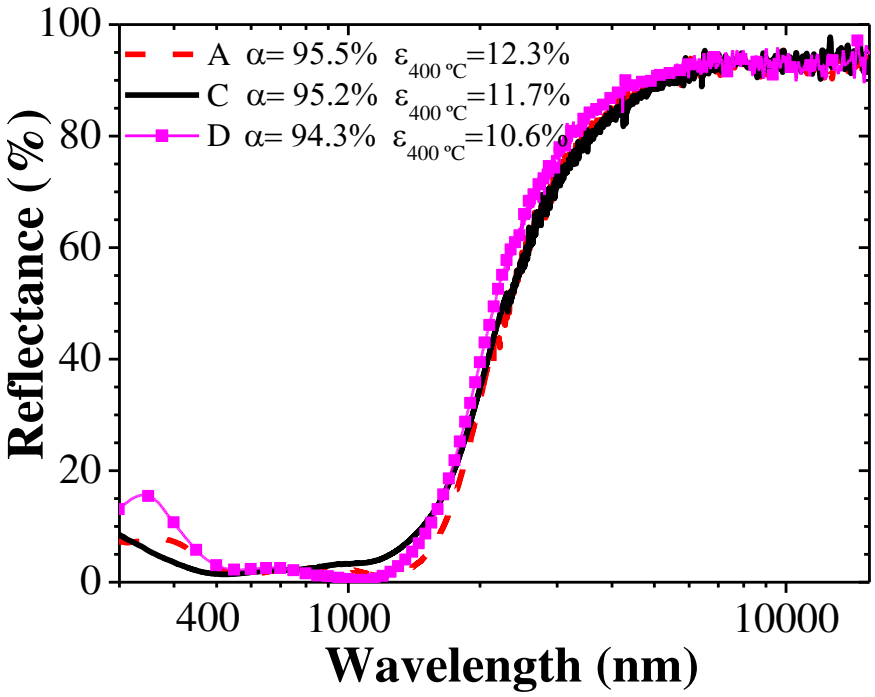

Figure 61: Reflectance of different $AlSiO_x$:W absorber coatings described in table 13. The absorptance and emissivity (at 400 ºC) are also indicated in the legend.

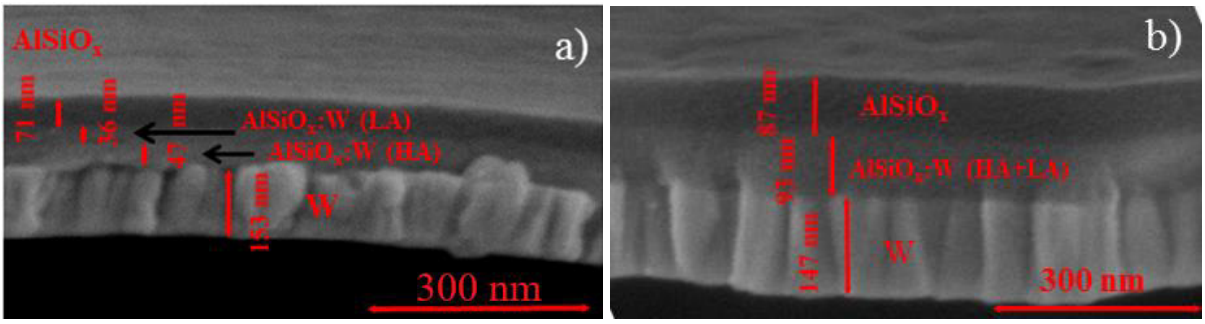

Figure 62: A cross section SEM images of (a) B; and (b) D samples deposited on stainless steel substrates. The bottom layer corresponds to W layer, and the top layer to the antireflection layer. The intermediate layer corresponds to the double layer structure (HA and LA layers).

In all cases, the first layer (W) shows a morphology consistent with a columnar growth. The remaining layers reveal a featureless morphology, which agrees with the amorphous structure obtained from the XRD analyses, as shown in Fig. 62 for $AlSiO_x$:W layers. The top layer is the $AlSiO_x$ antireflection layer. The contrast difference between the two cermet layers in the SEM micrographs is very small, with a slight distinction between them in Fig. 62a, but indistinguishable in Fig. 62b. This behaviour is related with metal volume fraction in the different layers. In sample B, the two cermet layers were deposited applying W target currents

of 0.75 and 0.3 A, respectively, while in sample D the two cermet layers were deposited with W target currents of 0.35 and 0.2 A, although with different rotation speeds, 15 rpm and 7 rpm, respectively. The thicknesses are similar to those mentioned in table 13, within a deviation of 10%.

These samples were analysed by XRD and a similar pattern was obtained for all as deposited samples. The pattern measured for sample D is shown in the Fig. 63. The peaks addressed to tungsten are related with W layer, which is polycrystalline. As expected, from the measurements of single layers, the other layers are XRD amorphous. The small peaks marked with S ($2\theta \approx 43.6º$, $44.5º$and $50.7º$) indicates the peaks associated with stainless steel substrate. Those peaks correspond to fcc-austenite (111), bcc-martensite (110) and austenite (200), respectively. The very small peak appearing at $2\theta \approx 36º$ is related with (200) of β phase of W. The small peak at $2\theta \approx 38.3º$ did not appear in XRD diffractograms of W layer and antireflection layer [26], which means it must be related with the cermet layers, but cannot be clearly addressed to a tungsten oxide phase or to aluminium oxide phase.

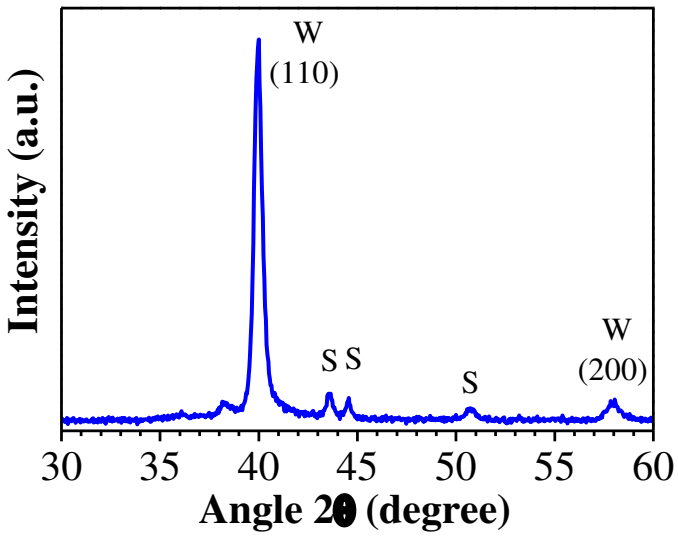

Figure 63: X-Ray diffraction pattern of as-deposited sample D. The measurements were performed with a fixed grazing incidence angle of 3º. S indicates the peaks associated with stainless steel substrate.

6.3 Thermal stability of the optical stacks

The optical stacks were subjected to a thermal annealing in air at 450 ºC and in vacuum at 580 ºC. In Fig. 64 the reflectance of representative coatings in their as-deposited state and after the thermal treatments in air (Fig. 64a and Fig. 64b) and in vacuum (Fig. 64c) is presented. In the legends are indicated the solar absorptance and thermal emittance (calculated at 400 ºC) for different situations.

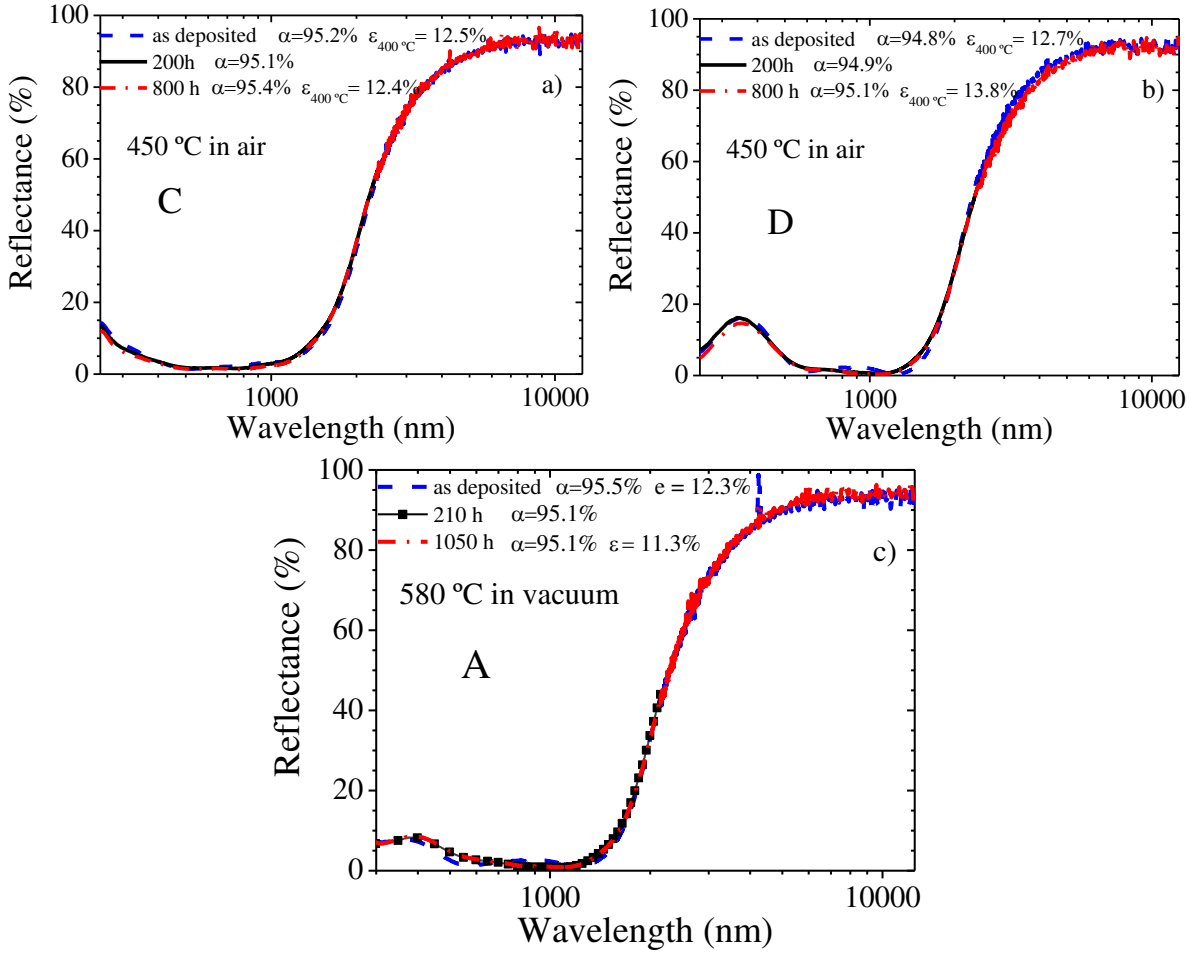

Figure 64: Reflectance of as deposited coatings and after the annealing of: a) sample C at 450 ºC in air, b) sample D at 450 ºC in air, and c) sample A at 580 ºC in vacuum, for the periods indicated in the legend. The solar absorptance and the thermal emittance (calculated at 400 ºC) after each annealing step are also indicated in the legend.

The reflectance profile of samples A, B and C revealed minor changes after the annealing in air at 450 ºC, similar to those shown in Fig. 64a. The changes in sample D were slightly higher, as shown in Fig. 64b. The change in the reflectance profile happened in the first annealing step, of 200 h, and in the following annealing steps only minor changes were seen. In terms of annealing in vacuum at 580 ºC, the samples A, B and C had a similar behaviour, as the one represented in the Fig. 64c, showing very small changes in the reflectance profile after the first annealing step, which induced a small decrease in solar absorptance and in emissivity, but without significant changes after the additional steps.

As also shown in the figure legend, the solar absorptance and thermal emittance (calculated at 400 ºC) values as a function of the annealing time, for annealing in air at 450 ºC and in vacuum at 580 ºC. The solar absorptance value is maintained after 33 days in air, at 450 ºC. The thermal emittance was measured in as deposited samples and after all annealing steps. Several samples revealed a small decrease, and only the sample D showed an increase of thermal emittance. This shows that these coatings have very good thermal stability and oxidation resistance. The similar samples were also annealed in air at 400 ºC, with identical results.

XRD diffractograms of annealed samples and as deposited samples are shown in Fig. 65. The XRD patterns of annealed samples A (Fig. 65a) and B (Fig. 65b) show small changes when compared with those measured in as deposited state. The main changes can be seen in peaks located at $2\theta \approx 43.6^{o}$, 44.5^{o} and 50.7^{o}, which are the peaks associated with 304 stainless steel substrates. A small increase in the intensity of (110) W peak, which can also be due to some grain growth in polycrystalline W layer, contributing for the emissivity decrease as already described in chapter 4 for the case of W/CrAlSiN_x/CrAlSiO_yN_x/SiAlO_x multilayer.

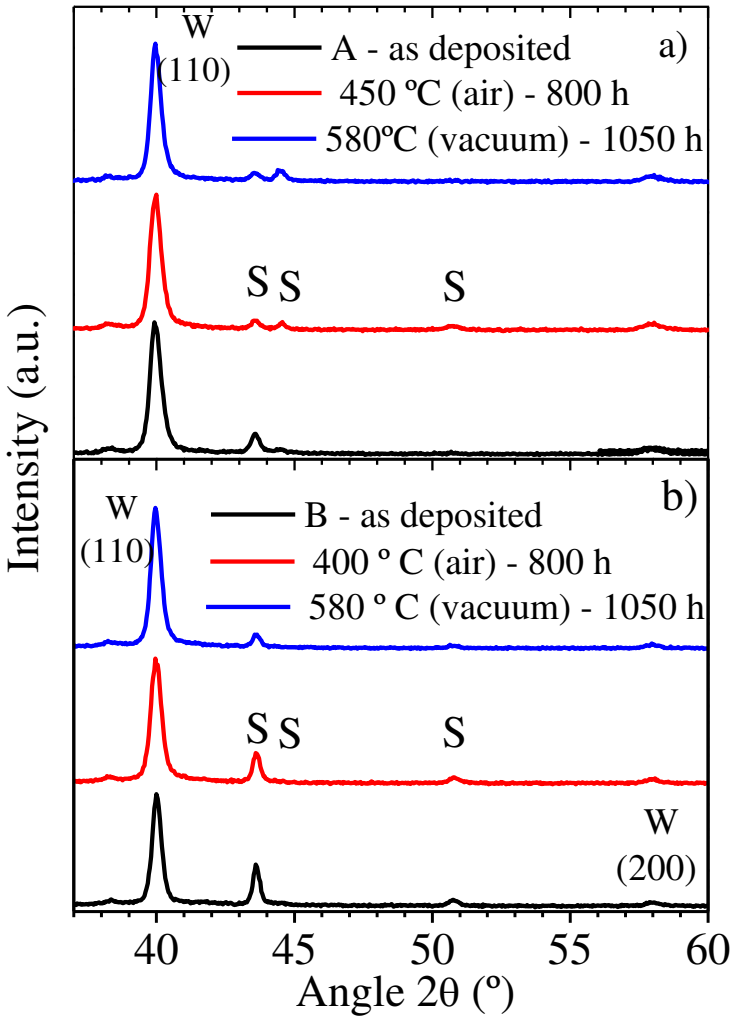

Figure 65: X-Ray patterns of samples A (a) and B (b) measured in as deposited state and after thermal treatments, as indicated in the figure. The legend indicates the diffractograms from bottom to top.

In order to assess any diffusion of metallic atoms towards the surface, three multilayer coatings from same run (sample D) were analyzed by XPS. One was in as deposited state, the second was annealed in air at 400 ºC and the third was annealed in vacuum at 580 ºC, both during 50 h. The antireflection layer, $AlSiO_x$, has a thickness of about 90 nm, which means the analysis was done within this surface layer. Core level spectra corresponding to Al 2p, Si 2p, O 1s and W 4f are shown in Fig. 66 and peak data extracted from fit are presented in Table 14.

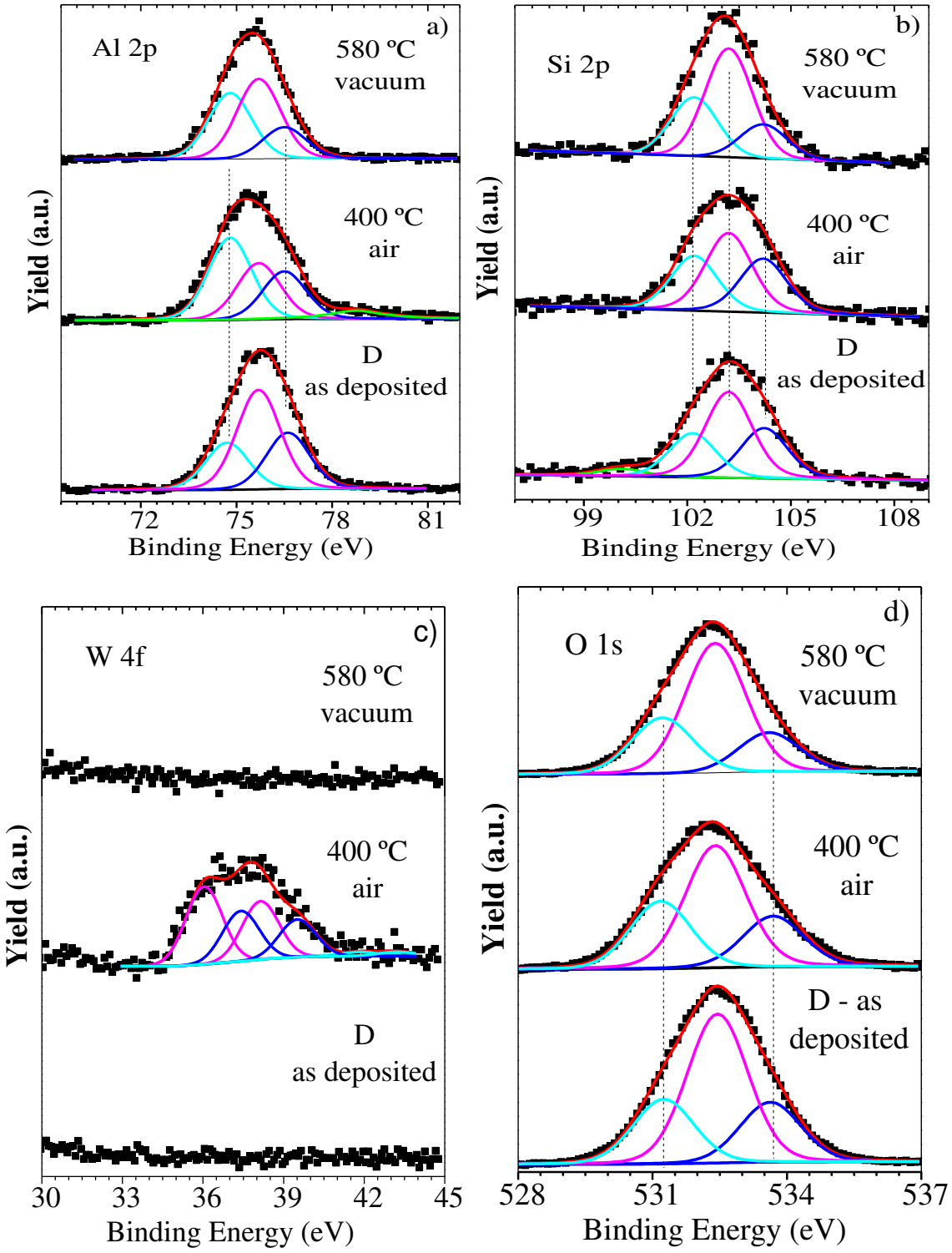

Figure 66: XPS spectra of: (a) Al 2p (b) Si 2p (c) W 4f and (d) O 1s electrons for analyzed D samples.

Fig. 66a shows Al 2p XPS core level spectra, and the results show that Al is present in oxidized (~74.8 eV, ~75.7 eV and ~76.5 eV) states, which binding energies correspond to Al_2O_3 and $Al(OH)_3$ compounds [206]. Fig. 66b shows Si 2p core level spectra. The as deposited sample revealed a small peak located at ~100 eV, which can be ascribed to the Si^+ oxidation state [207], showing that about 4% of the Si atoms are not oxidized. This peak disappeared after the thermal annealing, what can justify a small change in the optical properties of the coating. The remaining peaks, located at 102-104 eV, can be addressed to Si^{3+} and Si^{4+} oxidation states or to oxidized Si [207]. Oxidation was also reported in similar coatings based on SiO_2:W cermet layers[176], where was measured a small increase of oxygen amount together with a decrease of the H content in the surface layer. This past oxidation was also found in SiAlOx layers and described in chapter 4 for the case of W/CrAlSiN_x /CrAlSiO_yN_x /SiAlO_x multilayer.

The core level spectra corresponding to W 4f electrons are shown in Fig. 66c. The as deposited sample and the one annealed at 580 ºC in vacuum did not show any peak, in opposition to what happened with sample annealed in air at 400 ºC. The peaks show the presence of WO_3 in the surface of the antireflection layer. This represents only 0.4 at. % of this layer. More experiments would be needed to clarify this point, because this behaviour cannot be explained only by W out diffusion. The diffusion is a temperature dependent process, and at 580 ºC this out diffusion process would be more favourable, when compared to 400 ºC. However, the justification for this behaviour can be related not only with the annealing temperature but also with the annealing atmosphere. Under vacuum it mainly occurs outward diffusion processes, and AlSiOx is known as good barrier diffusion layer. Under air we have additionally oxidation processes due to oxygen inward diffusion, which can induce volume increase and interface degradation, what can facilitate the migration of oxidized species. This can also be related with incomplete surface coverage by the oxide layer due the presence of some scratches originated by the mechanical surface polishing prior the deposition. The O 1s peaks, ~531.2 and ~532.5 eV, (shown in Fig. 66d) can be addressed to C=O groups and C-OH and/or C-O-C groups, respectively [207]. The peak located at ~533.6 eV can be ascribed to SiO_2.

Table 14: Identification of core level binding energies of Al 2p, Si 2p, W4f and O 1s for as deposited samples and annealed at 400 ºC in air and at 580 ºC in vacuum.

	As deposited		400 ºC Air		580 ºC Vacuum		
	BE (eV)	**Peak area (%)**	**BE (eV)**	**Peak area (%)**	**BE (eV)**	**Peak area (%)**	**Oxidation state**
Al 2p	74.7	23.2	74.8	41.0	74.8	37.3	Al^{3+}
	75.7	49.0	75.7	28.1	75.7	45.0	Al^{3+} (Al_2O_3)
	76.6	27.7	76.5	23.8	76.5	17.7	Al^{3+} $Al(OH)_3$
Si 2p	100.0	4.0	--	--	--	--	Si^{+}
	102.2	23.5	102.2	29.3	102.2	29.2	Si^{2+}
	103.2	45.8	103.2	41.9	103.2	53.9	Si^{3+}
	104.2	26.8	104.2	28.8	104.2	16.9	Si^{4+}
W $4f_{7/2}$	--	--	36.0	60.7	--	--	W^{6+}
	--	--	37.4	39.3	--	--	W^{6+}
O 1s	531.2	23.7	531.2	27.5	531.2	24.9	
	532.5	54.5	532.4	51.2	532.4	57.6	
	533.6	21.9	533.7	21.3	533.6	17.5	

The Rutherford Backscattering was also used to study the possibility W diffusion to sample surface with the annealing. Experimental RBS spectrum of the sample annealed at 400 ºC in air is displayed in Fig. 67. No significant differences were seen with the other two samples, the as deposited and the one annealed in vacuum. Since the outermost layer of the multilayer is the

SiAlOx layer, the backscattered signal from the W in the first AlSiOx: W layer is shifted to lower energies, as shown in Fig. 67. In this layer was not found any W content (within the error of the measurement). The minimum amount that can be detected in this geometry is 0.2 at. %, when the signal can be distinguished from the pileup background. The W content of the AlSiOx: W(LA) layer is 14.2 at. %, while for the AlSiOx: W(HA) layer is 19.9 at.%.

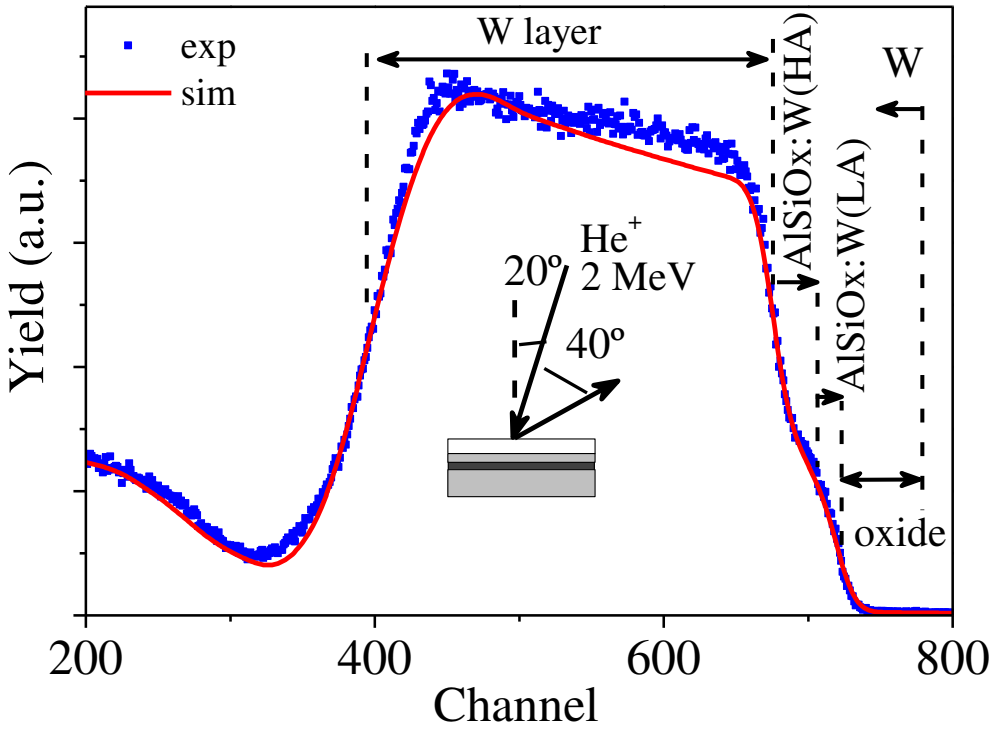

Figure 67: RBS spectrum of D sample after annealing at 400 ºC in air.

In conclusion, the design and the fabrication of a four-layer coating based on the $AlSiO_x$:W cermet layers for selective absorption of solar thermal radiation was performed. The X-ray diffractograms of $AlSiO_x$:W layers indicated that both components, W and $AlSiO_x$, are amorphous. The dielectric function and the thickness of the different layers deposited on glass were calculated through the modelling of the experimental transmittance and reflectance curves by a commercial optical simulation program (SCOUT). The optical constants of the single layers were then used to construct the four-layer stack. The as deposited optical stack, W/$AlSiO_x$:W(HA)/$AlSiO_x$:W(LA)/$AlSiO_x$, revealed a solar absorptance of 94%-95.5% and emissivity of 8%-9% (at 100 ºC) and 10%-14% (at 400 ºC). XPS results showed that the high metal volume fraction cermet layer, $AlSiO_x$: W(HA), of samples A, B and C have about one third of W atoms in the W^0 oxidation state, another third in the W^{x+} oxidation state and the last

third in the W^{4+}, W^{5+} and W^{6+} oxidation states. The samples were subjected to a thermal annealing at 450 ºC in air, and at 580 ºC, in vacuum, and the tandem structure showed very good thermal stability. A small change in the reflectance profile was found after the first annealing step, but no significant changes were found after the additional steps.

Samples annealed under air at 400 ºC revealed the presence of W in the surface of the antireflection surface layer. The as deposited sample and the one annealed at 580 ºC in vacuum did not reveal W at the absorber layer. In a long term and under air annealing, this behaviour would have impact on the optical properties of the absorber. To avoid this, the absorbers are under vacuum which improves its durability

Chapter 7

7.1 Discussion

This section discusses the main results of the thesis. Firstly, the optical properties, chemical composition, chemical structure, morphology and mechanical properties of sputtered $CrAlSiN_x$ and $CrAlSiO_yN_x$, varying P_N and P_{ON} respectively, have been studied in Ch. 4. The spectral optical constants n and k of those layers decrease with increasing P_N and P_{ON}, and the refractive index increases in the wavelength range of 300-1000 nm for all coatings. Films' elemental composition ratio (Cr +Al+ Si)/ (N +O) decreases with increasing nitrogen and oxygen partial pressure. However, the elemental Cr: Al: Si composition ratio remains constant as 1.25: 1.5 :1. XPS reveals an Al surface enrichment and a significant Cr surface depletion, because in the sample analysed by XPS the (Al + Si)/Cr composition ratio is in average 2 times higher than that obtained by RBS and EDS, together with an increment of Al/Si composition ratio. Coatings with higher nitrogen and oxygen content ((Cr+Al+Si)/(N+O) ~1) are polycrystalline with cubic (fcc-B_1) structure, but those used in the solar absorber coatings are sub-stoichiometric. On contrary, all other films are amorphous and show poor hardness. Layers with adequate optical properties for the construction of the optical stack belong to the region of reactive gases partial pressure where the films are amorphous.

The both antireflection $SiAlO_x$ and $AlSiO_x$ oxide layers are transparent with refractive index n= 1.52 and extinction coefficient k ~0. They are amorphous and show an excellent thermal stability, especially after further annealing steps, protecting other layers against oxidation.

In most cases, the W layer showed a combination of both α- and β- phase of growth, but the α- phase is dominant and it is polycrystalline with (110) orientation. Despite that, the results show a very good resistance against oxidation and thermal stability, which means it is well protected by the other outer layer. Tungsten is one of the best materials for this purpose because

it has a high reflectance in the NIR range of wavelength, which improve the selectivity of stacks by decreasing the thermal emission.

The multilayer that consists in a structure of W/CrAlSiN_x/CrAlSiO_yN_x/SiAlO_x shows simultaneously high average solar absorbance, α_{sol}=95.2%, and low emissivity ε= 9.8% (calculated at 400 ºC) together with high thermal stability at 400 ºC, in air, and at 600 ºC, in vacuum, for 650 h. After the first step of thermal annealing in vacuum at 600 ºC, the reflectance curve of the stack shifted towards lower wavelength, which caused a small decrement in the value of solar absorbance. The increase in reflectance in IR wavelength range (λ> 3000 nm) is due to the phase changes of the back-reflector tungsten layer, which also contributes to a decrease in the emissivity after the vacuum annealing. Incomplete oxidized Si atoms in the antireflection layer can eventually introduce small changes in reflectance curves of the stack for wavelengths lower than 1500 nm. However, after further steps of annealing, no significant changes were seen. In most cases, thermal emissivity improved a bit or stayed constant. The RBS and TOF-ERDA analyses have shown a small amount of W diffused during annealing towards stainless steel substrate, and at the same time Cr diffused from the nitride and oxynitride layers towards the surface. The reason for Cr diffusion can be related with the sub-stoichiometry of those layers in terms of (N+O)/(Cr+Al+Si) atomic ratio. Thus, those layers have part of the Cr atoms in metallic oxidation state, which favours the diffusion. To avoid the Cr diffusion, it is necessary to increase the stoichiometry of CrAlSiNx and CrAlSiNxOy layers while maintaining their optical properties The Cr in the surface of the multilayer can also be due to some surface defects. To minimize the W diffusion, a diffusion barrier layer between the stainless-steel substrate and the tungsten layer is necessary and contributed for better performance

For the multilayer stack based on tungsten nitride and oxynitride presented in Ch. 5, the single layers of SiAlN_x and SiAlO_yN_x were used to study the structural, optical and chemical properties. The XPS analysis proved the existence of tungsten in metallic oxidation state, that may improve the solar absorptance of the tandem because of its contribution to the absorption in the visible solar radiation wavelength, although can compromise the long-term thermal stability. The main difference between the used CrAlSiNxOy and SiAlO_yN_x

oxynitride layers in both designs, in term of chemical composition, is the CrAlSiNxOy layers are sub-stoichiometric, whereas $WSiAlO_yN_x$ are almost stoichiometric. This may justify why the optical spectral stack based on $WSiAlN_x/WSiAlO_yN_x$ shows better thermal stability after several steps of thermal annealing in vacuum and air.

The based $AlSiO_x$:W cermets multilayer solar selective absorber coatings are composed of four layers structure, $W/AlSiO_x$:W(HA)/$AlSiO_x$:W(LA)/$AlSiO_x$, deposited on stainless-steel. The film structure has a good spectral selective property that is suitable for solar thermal applications, with the coatings exhibiting a solar absorptance of 94%-95.5% and emissivity of 10%-14% (at 400 ºC). XPS analysis for the sample annealed in air proved the presence of WO_3 in the surface of the antireflection layer. This represents only 0.4 at. % of this layer, which can be negligible and can be due to some surface defects, because W was not seen in the surface of multilayers annealed in vacuum at higher temperature.

The structure of the high absorption layers, $WSiAlN_x$, and $AlSiO_x$:W cermet (750 mA) is very similar. Although the first was prepared with nitrogen and the second with oxygen, the oxidation states of W atoms have a similar distribution, with about one third of the W atoms in the metallic oxidation state, as shown in Fig. 47a and Fig 59 (XPS analysis). The XRD patterns of both layers are also very similar, as shown in Fig. 68.

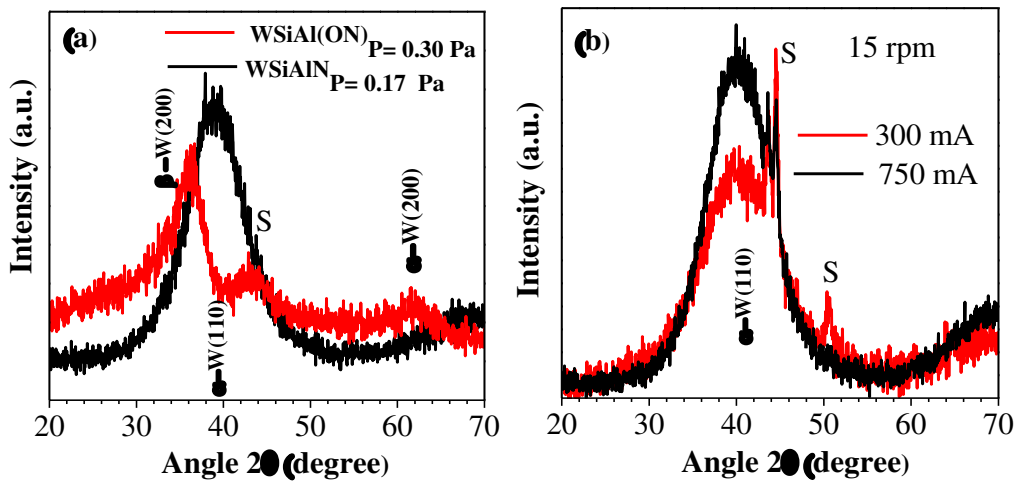

Figure 68: XRD diffractograms of: (a) XRD patterns of $WSiAlNx_{P=0.17\ Pa}$ and $WSiAlOyNx_{P=0.30\ Pa}$ single layers (b) $AlSiO_x$:W single layers prepared with different W target currents and rotation speeds 15 rpm.

In case of low absorption layers, $WSiAlO_yN_x$ and $AlSiO_x$:W cermet (300 mA) they already present some differences. The oxynitride layer does not have W atoms in the metallic oxidation state but has a big fraction of the W atoms with W-N bonds. In these samples the W content in nitride and oxynitride layers is around 30 at.%, whereas in the case of cermet absorption layers the W content is below 20 at.%. The difference is related with the fabrication process because nitride and oxynitride layers could have less W, but in that case, it would be necessary to increase the Si and Al pellets in the W target. In general, the emittance of the tandem was improved after first step of air and vacuum annealing. This means the IR absorption decreased and/or IR reflectance on W layer increased, showing that oxide and oxynitride layers protect the W layer against oxidation. In the case of $AlSiO_x$:W cermets, two targets (W and AlSi) were used to deposit all stack, while in case of the nitride/oxynitride based structure 3 targets (W, WSiAl and SiAl) were used. In the second case it was used a target with high Si content (in first case was Al prevailing) and allowed to obtain an antireflection layer with lower refractive index. This can be one of the reasons the solar absorptance of nitride/oxynitride structure is slightly higher than cermets structure.

7.2 Conclusions

Three types of selective solar thermal absorber for high temperature application were designed, fabricated, characterized, and the respective performance was evaluated. The first two coatings, deposited by magnetron sputtering, are based on transition metal nitride/ oxynitride, consisting in four layers deposited on stainless-steel substrate, as back reflector/ high absorption/ low absorption/ antireflection layers, and they are based on the transition metals chromium and tungsten as W/CrAlSiNx/CrAlSiNxOy/SiAlOx and W/WSiAlNx/ WSiAlNxOy/SiAlOx, respectively. The third is a design based on $AlSiO_x$:W cermets, which is also composed of the four layers structure, W/$AlSiO_x$:W(HA)/$AlSiO_x$:W(LA)/$AlSiO_x$ deposited on stainless-steel substrates.

A comparison between the three solar absorbers presented in the thesis is presented in Table 15. All solutions show simultaneously high solar absorptance, α_{sol}, and low emissivity,

ε, together with high thermal stability in air and in vacuum, allowing to reach the objectives of this research. The solution based on $WSiAlN_x/WSiAlO_yN_x$ tandem showed the best thermal stability, oxidation resistance and it has higher solar absorbance (α_{sol}) while the CrAlSiNx/ CrAlSiNxOy shows the lowest thermal emittance at the temperature (400 ºC). These kinds of selective solar thermal absorber coatings are recommended for high temperature (600 ºC in Vacuum).

Table 15: Comparison between the three solar thermal absorbers

Solar absorber	Solar absorptance (α_{sol}) %	Emissivity ($\varepsilon_{400\ ^oC}$) %	Thermal stability
$W/CrAlSiN_x/CrAlSiO_yN_x/SiAlO_x$	95.2	9.8	Very Good
$W/WSiAlN_x/WSiAlO_yN_x/SiAlO_x$	96.0	10.5	Excellent
$W/AlSiO_x$:W(HA)/$AlSiO_x$:W(LA)/$AlSiO_x$	94-95.5	10.0-14.0	Very good

7.3 Further work.

One of the most interesting future works related to the selective solar thermal absorbers presented in this thesis is to study the upper limits of temperature in vacuum and air. Further studied should be performed for the structure, thermal stabilities, diffusion barrier layers between the stainless-steel substrates and tungsten for the second and third designs.

The research also opens a door for developing and designing other types of selective solar thermal absorbers based on high temperature structures based on metal cermets. Beginning with our published research about the AlSiOx:W cermets tandem, the effect of adding titanium Ti or Pt to and W as transition metals in the cermet matrix AlSiOx as AlSiOx:WTi, AlSiOx:Pt or AlSiOx:WPt can be studied. The use of a Pt back reflector should be considered, if necessary to increase the operating temperature.

References

[1] A. AL-Rjoub, P. Costa, L. Rebouta, M.F Cerqueira, P. Alpuim, N.P. Barradas, E. Alves, Characterization of magnetron sputtered sub-stoichiometric CrAlSiNx and CrAlSiOyNx coatings, Surf. Coatings Technol. 328 (2017) 134–141.

[2] A. AL-Rjoub, P. Costa, L. Rebouta, I. Bogdanovi, K. Arstila, N.P. Barradas. (in press), A study of solar thermal absorber stack based on CrAlSiNx/ CrAlSiNxOy structure by ion beams, Nucl. Inst, Methods Phys. Res. B. (2018).

[3] A. AL-Rjoub, L. Rebouta, P. Costa, N.P. Barradas, E. Alves, P.J. Ferreira, K. Abderra, A. Matilainen, K. Pischow, A design of selective solar absorber for high temperature applications, Sol. Energy. 172 (2018) 177–183.

[4] A. AL-Rjoub, L. Rebouta, P. Costa, L.G. Vieira, Multi-layer solar selective absorber coatings based on W/WSiAlNx/WSiAlOyNx /SiAlOx for high temperature applications, Sol. Energy Mater. Sol. Cells. 186 (2018) 300–308.

[5] D. Dias, L. Rebouta, P. Costa, A. AL-Rjoub, M. Benelmeki, C.J. Tavares, N.P. Barradas, E. Alves, P. Santilli, K. Pischow, Optical and structural analysis of solar selective absorbing coatings based on AlSiOx :W cermets, Sol. Energy. 150 (2017) 335–344.

[6] P. Costa, A. AL-Rjoub, L. Rebouta, N.K. Manninen, D. Alves, B. Almeida, N.P. Barradas, E. Alves, Influence of Al/Si atomic ratio on optical and electrical properties of magnetron sputtered $Al_{1-x}Si_xO_y$ coatings, Thin Solid Films. 669 (2019) 475-481.

[7] A. AL-Rjoub, L. Rebouta, P. Costa, L.G. Vieira, T.M.R. Miranda, N.P. Barradas, E. Alves, CrAlSiN barrier layer to improve the thermal stability of W/CrAlSiNx/CrAlSiOyNx /SiAlOx solar thermal absorber, Sol. Energy Mater. Sol. Cells. 191 (2018) 235-242.

[8] J.M. Jefferson, Global climate change and the challenges for renewable energy, Renew. Energy. 15 (1998) 1–7.

[9] Y. Yang, The Study of Nanostructured Solar Selective Coatings, University of Yourk, 2012.

[10] N. Selvakumar, H.C. Barshilia, Review of physical vapor deposited (PVD) spectrally selective coatings for mid- and high-temperature solar thermal applications, Sol. Energy Mater. Sol. Cells. 98 (2012) 1–23.

[11] S.A. Klein, J.A. Duffie, W.A. Beckman, Transient Considerations of Flat-Plate Solar Collectors, J. Eng. Power. 96 (1974).

[12] H.L. Zhang, J. Baeyens, J. Degrève, G. Cacères, Concentrated solar power plants: Review and design methodology, Renew. Sustain. Energy Rev. 22 (2013) 466–481.

[13] D. Barlev, R. Vidu, P. Stroeve, Innovation in concentrated solar power, Sol. Energy Mater. Sol. Cells. 95 (2011) 2703–2725.

[14] C.L. Martin, D.Y. Goswami, Solar Energy Pocket Reference, 1 st, Earthscan, Michigan, 2005.

[15] D.K. Lamba, A review on parabolic trough type solar collectors: innovation, applications and thermal energy storage, in: YMCA Univ. Sci. Technol., 2012: pp. 90–99.

[16] A. Fernández-García, E. Zarza, L. Valenzuela, M. Pérez, Parabolic-trough solar collectors and their applications, Renew. Sustain. Energy Rev. 14 (2010) 1695–1721.

[17] S.D. Odeh, G.L. Morrison, M. Behnia, Modelling of parabolic trough direct steam generation solar collectors, Sol. Energy. 62 (1998) 395–406.

[18] S. Kalogirou, S. Lloyd, J. Ward, Modelling, optimisation and performance evaluation of a parabolic trough solar collector steam generation system, Sol. Energy. 60 (1997) 49–59.

[19] J. Wang, S. Yang, C. Jiang, Y. Zhang, P.D. Lund, Status and future strategies for Concentrating Solar Power in China, Energy Sci. Eng. 5 (2017) 100–109.

[20] F. Sulaiman, N. Abdullah, B. Singh, M. Singh, A Simulated Design and Analysis of a Solar Thermal Parabolic Trough Concentrator, Int. J. Environ. Ecol. Eng. 6 (2012) 136–140.

[21] M. Eickhoff, US 7,240,675 B2, 2007.

[22] L.D. Jaffe, Test results on parabolic dish concentrators for solar thermal power systems, Sol. Energy. 42 (1989) 173–187.

[23] E. V Votyakov, C.N. Papanicolas, Consistent Multiphysics Simulation of a Central Tower CSP Plant as Applied to ISTORE, in: AIP Conf. Proc., American Institute of Physics, 2017.

[24] A. Boretti, Concentrated Solar Power Plants Capacity Factors: A Review. In: Dai L., Jazar R. (eds) Nonlinear Approaches in Engineering Applications, Springer, Cham, 2018.

[25] IRENA, Renewable Power Generation Costs in 2017, Int. Renew. Energy Agency. (2018).

[26] L. Rebouta, A. Sousa, M. Andritschky, F. Cerqueira, C.J. Tavares, P. Santilli, K. Pischow, Solar selective absorbing coatings based on AlSiN/AlSiON/AlSiOy layers, Appl. Surf. Sci. 356 (2015) 203–212.

[27] C.E. Kennedy, Review of Mid-to High-Temperature Solar Selective Absorber Materials, Natl. Renew. Energy Lab. (2002).

[28] H. Tabor, Selective radiation. I. Wavelength discrimination. II. Wavefront discrimination, Bull. Res. Counc. Isr., Sect. C. 5A:2 (1956).

[29] J.T. Gier, R. V. Dunkle, Selective spectral characteristics as an important factor in the efficiency of solar collocters, Trans. Conf. Use Sol. Energy. 2, Part I (1955) 41–56.

[30] L.H. Shaffer, Wavelength-dependent (selective) processes for the utilization of solar energy, Sol. Energy. 2 (1958).

[31] F. Cao, K. Mcenaney, G. Chen, Z. Ren, A review of cermet-based spectrally selective solar absorbers, Energy Environ. Sci. 7 (2014) 1615–1627.

[32] F. Gomez-Garcia, J. González-Aguilar, G. Olalde, M. Romero, Thermal and hydrodynamic behavior of ceramic volumetric absorbers for central receiver solar power plants: A review, Renew. Sustain. Energy Rev. 57 (2016) 648–658.

[33] S. Mey-Cloutier, C. Caliot, A. Kribus, Y. Gray, G. Flamant, Experimental study of ceramic foams used as high temperature volumetric solar absorber, Sol. Energy. 136 (2016) 226–235.

[34] R. Capuano, T. Fend, P. Schwarzbözl, O. Smirnova, H. Stadler, B. Hoffschmidt, R. Pitz-Paal, Numerical models of advanced ceramic absorbers for volumetric solar receivers, Renew. Sustain. Energy Rev. 58 (2016) 656–665.

[35] Q. Zhang, Y. Yin, D.R. Mills, High efficiency Mo-Al_2O_3 cermet selective surfaces for high-temperature application, Sol. Energy Mater. Sol. Cells. 40 (2006) 43–53.

[36] V. Teixeira, E. Sousa, M.F. Costa, C. Nunes, L. Rosa, M.J. Carvalho, M. Collares-Pereira, E. Roman, J. Gago, Spectrally selective composite coatings of Cr-Cr_2O_3 and Mo- Al_2O_3 for solar energy applications, Thin Solid Films. 392 (2001) 320–326.

[37] F. Cao, D. Kraemer, L. Tang, Y. Li, A.P. Litvinchuk, J. Bao, G. Chen, Z. Ren, A high-performance spectrally-selective solar absorber based on a yttria-stabilized zirconia cermet with high-temperature stability, Energy Environ. Sci. 8 (2015) 3040–3048.

[38] Z.Y. Nuru, C.J. Arendse, R. Nemutudi, O. Nemraoui, M. Maaza, Pt – Al_2O_3 nanocoatings for high temperature concentrated solar thermal power applications, Phys. B Phys. Condens. Matter. 407 (2012) 1634–1637.

[39] E. Sani, L. Mercatelli, P. Sansoni, L. Silvestroni, D. Sciti, Spectrally selective ultra-high temperature ceramic absorbers for high-temperature solar plants, J. Renew. Sustain. Energy. 4 (2012).

[40] E. Sani, M. Meucci, L. Mercatelli, A. Balbo, C. Musa, R. Licheri, R. Orrù, G. Cao, Titanium diboride ceramics for solar thermal absorbers, Sol. Energy Mater. Sol. Cells. 169 (2017) 313–319.

[41] X. Wang, J. Gao, H. Hu, H. Zhang, L. Liang, K. Javaid, High-temperature tolerance in WTi-Al2O3 cermet-based solar selective absorbing coatings with low thermal emissivity, Nano Energy. 37 (2017) 232–241.

[42] A. Antonaia, A. Castaldo, M.L. Addonizio, S. Esposito, Stability of W- Al_2O_3 cermet based solar coating for receiver tube operating at high temperature, Sol. Energy Mater. Sol. Cells. 94 (2010) 1604–1611.

[43] Q. Zhang, D.R. Mills, Very low-emittance solar selective surfaces using new film structures, J. Appl. Physiscs. 72 (1992) 3013–3021.

[44] H.C. Barshilia, N. Selvakumar, K.S. Rajam, Thermal stability of TiAlN/ TiAlON/ Si_3N_4 absorbers prepared by reactive direct, Jounal Vac. Sci. Technol. 25 (2007).

[45] Y. Wu, C. Wang, Y. Sun, Y. Ning, Y. Liu, Y. Xue, W. Wang, S. Zhao, E. Tomasella, Study on the thermal stability of Al/ NbTiSiN/ NbTiSiON/ SiO_2 solar selective absorbing coating, Sol. Energy. 119 (2015) 18–28.

[46] C. Zou, W. Xie, L. Shao, Functional multi-layer solar spectral selective absorbing coatings of AlCrSiN/AlCrSiON/AlCrO for high temperature applications, Sol. Energy Mater. Sol. Cells. 153 (2016) 9–17.

[47] L. Rebouta, P. Capela, M. Andritschky, A. Matilainen, P. Santilli, K. Pischow, E. Alves,

Characterization of TiAlSiN/TiAlSiON/SiO_2 optical stack designed by modelling calculations for solar selective applications, Sol. Energy Mater. Sol. Cells. 105 (2012) 202–207.

[48] A. Dan, A. Biswas, P. Sarkar, S. Kashyap, K. Chattopadhyay, H.C. Barshilia, B. Basu, Enhancing spectrally selective response of W/WAlN/WAlON/ Al_2O_3– Based nanostructured multilayer absorber coating through graded optical constants, Sol. Energy Mater. Sol. Cells. 176 (2018) 157–166.

[49] H.C. Barshilia, N. Selvakumar, K.S. Rajam, D. V. Sridhara Rao, K. Muraleedharan, Deposition and characterization of TiAlN/TiAlON/Si_3N_4 tandem absorbers prepared using reactive direct current magnetron sputtering, Thin Solid Films. 516 (2008) 6071–6078.

[50] J. Jyothi, A. Soum-glaude, H.S. Nagaraja, H.C. Barshilia, Measurement of high temperature emissivity and photothermal conversion e ffi ciency of TiAlC/TiAlCN/TiAlSiCN/TiAlSiCO/ TiAlSiO spectrally selective coating, Sol. Energy Mater. Sol. Cells. 171 (2017) 123–130.

[51] J. Feng, S. Zhang, Y. Lu, H. Yu, L. Kang, The spectral selective absorbing characteristics and thermal stability of SS/TiAlN/TiAlSiN/Si_3N_4 tandem absorber prepared by magnetron sputtering, Sol. Energy. 111 (2015) 350–356.

[52] T.D. Nguyen, S.K. Kim, D.B. Lee, High-temperature oxidation of nano-multilayered TiAlCrSiN thin films in air, Surf. Coatings Technol. 204 (2009) 697–704.

[53] Y. Ning, W. Wang, L. Wang, Y. Sun, P. Song, H. Man, Y. Zhang, B. Dai, J. Zhang, C. Wang, Y. Zhang, S. Zhao, E. Tomasella, A. Bousquet, J. Cellier, Optical simulation and preparation of novel Mo/ZrSiN/ZrSiON/SiO_2 solar selective absorbing coating, Sol. Energy Mater. Sol. Cells. 167 (2017) 178–183.

[54] S.A. Cho, R. Fookes, C.A. Garris, Efficiency of ceramic absorber coatings for solar-thermal conversion, Ceram. Int. 7 (1981) 8–12.

[55] M. Farooq, M.G. Hutchins, A novel design in composities of various materials for solar selective coatings, Sol. Energy Mater. Sol. Cells. 71 (2002) 523–535.

[56] J. Clerk, Maxwell, A Dynamical Theory of the Electromagnetic Field, Phil. Trans. R. Soc. Lond. 155 (1865) 459–512.

[57] G. Hall, Maxwell's electromagnetic theory and special relativity, Philos. Trans. R. Soc. A Math. Phys. Eng. Sci. 366 (2008) 1849–1860.

[58] M. Iqbal, An Introduction To Solar Radiation, 1st ed., Academic Press, New York, 1983.

[59] F. Kasten, A new table and approximate formula for relative optical air mass, Arch. Für Meteorol. Geophys. Und Bioklimatologie. 14 (1965) 206–223.

[60] C. Johnson, Mathematical Physics of BlackBody Radiation, Icarus iDucation. Skolan for datavetenskap och kommunikation, Kungliga Tekniska Hogskolan, Stockholm, 2012.

[61] M. Fox, Optical properties of solids, Oxford University Press Inc., New York, 2001.

[62] J. Weiner, P.-T. Ho, Light-Matter Interaction, John Wiley & Sons, New Jersey, 2008.

[63] B.E.A. Saleh, M.C. Teich, Fundamentals of Photonics, 2nd ed., John Wiley & Sons, Inc, Oxford, 2007.

[64] T.H. Wendell, C.H. Lee, Light-Matter Interaction: Atoms and Molecules in External Fields and Nonlinear Optics, Wiley-VCH Verlag GmbH & Co. KGaA, 2006.

[65] Z. Chen, Carbon Nanotube Spectrally Selective Solar Thermal Absorbers, The Arctic university of Norway, 2016.

[66] I.H. Pérez, Multilayer solar selective coatings for high temperature solar applications : From concept to design, Universidad de Sevilla, 2016.

[67] K. Zhang, L. Hao, M. Du, J. Mi, J.N. Wang, J. ping Meng, A review on thermal stability and high temperature induced ageing mechanisms of solar absorber coatings, Renew. Sustain. Energy Rev. 67 (2017) 1282–1299.

[68] C.C. Kim, J.W. Garland, H. Abad, P.M. Raccah, Modeling the optical dielectric function of semiconductors: Extension of the critical-point parabolic-band approximation, Phys. Rev. B. 45 (1992) 749–767.

[69] S.K. O'Leary, S.R. Johnson, P.K. Lim, The relationship between the distribution of electronic states and the optical absorption spectrum of an amorphous semiconductor: An empirical analysis, J. Appl. Phys. 82 (1997) 3334–3340.

[70] Y. Yin, R.E. Collins, Optimization and analysis of solar selective surfaces with continuous and multilayer profiles, J. Appl. Physiscs. 77 (1995).

[71] H.A. Macleod, Thin film optical coatings, 4 th, CRC Press, New York, 2010.

[72] H.K. Raut, V.A. Ganesh, A.S. Nair, S. Ramakrishna, Anti-reflective coatings: A critical, in-depth review, Energy Environ. Sci. 4 (2011) 3779–3804.

[73] H. Haitjema, Spectrally selective tinoxide and indiumoxide coatings, Technische Universiteit Delf, 2014.

[74] T.C. Paulick, Inversion of normal-incidence (R,T) measurements to obtain n + ik for thin films, Appl. Opt. 25 (1986).

[75] Y.A. Çengel, A.J. Ghajar, Heat and mass transfer : fundamentals & applications, 5th ed., McGraw Hill, New York, 2015.

[76] T. Testafamichael, Characterization of Selective Solar Absorbers, Acta universita Upsaliensis Uppsala, 2000.

[77] C. Da Wen, I. Mudawar, Modeling the effects of surface roughness on the emissivity of aluminum alloys, Int. J. Heat Mass Transf. 49 (2006) 4279–4289.

[78] B.K.G. O. P. Agnihotri, Solar Selective Surfaces, 1 st, Wiley, Michigan, 1981.

[79] E. Randich, D.D. Allred, Chemically vapor-deposited ZrB_2 as a selective solar absorber, Thin Solid Films. 83 (1981) 393–398.

[80] C.A. Arancibia-Bulnes, C.A. Estrada, J.C. Ruiz-Sùarez, Solar absorptance and thermal emittance of cermets with large, Appl. Phys. 33 (2000) 2489–2496.

[81] G. Pellegrini, Experimental Methods for the Preparation of Selectively Absorbing Textured Surfaces for Photothermal Solar Conversion., Sol. Energy Mater. 3 (1980) 391–404.

[82] J. Feng, S. Zhang, X. Liu, H. Yu, H. Ding, Y. Tian, Solar selective absorbing coatings TiN/ TiSiN/SiN prepared on stainless steel substrates, Vaccum. 121 (2015) 135–141.

[83] A.G. Wattoo, C. Xu, L. Yang, C. Ni, C. Yu, X. Nie, M. Yan, S. Mao, Design , fabrication and thermal stability of spectrally selective TiAlN/SiO_2 tandem absorber, Sol. Energy. 138 (2016) 1–9.

[84] A. Soum-glaude, A. Le, M. Bichotte, C. Escape, L. Dubost, Optical characterization of TiAlNx/ TiAlNy/Al_2O_3 tandem solar selective absorber coatings, Sol. Energy Mater. 170 (2017) 254–262.

[85] C. Zou, L. Huang, J. Wang, S. Xue, Effects of antire fl ection layers on the optical and thermal stability properties of a spectrally selective CrAlN – CrAlON based tandem absorber, Sol. Energy Mater. Sol. Cells. 137 (2015) 243–252.

[86] D. Gong, H. Liu, G. Luo, P. Zhang, X. Cheng, B. Yang, Y. Wang, J. Min, W. Wang, S. Chen, Z. Cui, K. Li, Thermal aging test of AlCrNO-based solar selective absorbing coatings prepared by cathodic arc plating, Sol. Energy Mater. Sol. Cells. 136 (2015) 167–171.

[87] P. Song, Y. Wu, L. Wang, Y. Sun, Y. Ning, Y. Zhang, B. Dai, E. Tomasella, A. Bousquet, C. Wang, The investigation of thermal stability of Al/NbMoN/NbMoON/SiO_2 solar selective absorbing coating, Sol. Energy Mater. Sol. Cells. 171 (2017) 253–257.

[88] A. Dan, K. Chattopadhyay, H.C. Barshilia, B. Basu, Angular solar absorptance and thermal stability of W/WAlN/WAlON/ Al_2O_3-based solar selective absorber coating, Appl. Therm. Eng. 109 (2016) 997–1002.

[89] Y. Liu, Z. Wang, D. Lei, C. Wang, A new solar spectral selective absorbing coating of SS–(Fe_3O_4)/ Mo/TiZrN/TiZrON/SiON for high temperature application, Sol. Energy Mater. Sol. Cells. 127 (2014) 143–146.

[90] R. Blickensderfer, D.K. Deardorff, R.L. Lincoln, A. Metallurgy, Spectral reflectance of TiNx and ZrNx films as selective solar absorbers, Sol. Energy. 19 (1977) 429–432.

[91] J.A. Thornton, J.L. Lamb, Thermal stability studies of sputter-deposited multilayer selective absorber coatings, Thin Solid Films. 96 (1982) 175–183.

[92] E. Céspedes, M. Wirz, J.A. Sánchez-garcía, L. Alvarez-fraga, R. Escobar-galindo, C. Prieto, Novel Mo – Si_3N_4 based selective coating for high temperature concentrating solar power applications, Sol. Energy Mater. Sol. Cells. 122 (2014) 217–225.

[93] Q. Zhang, Stainless-steel — AlN cermet selective surfaces deposited by direct current magnetron sputtering technology, Sol. Energy Mater. Sol. Cells. 52 (1998) 95–106.

[94] D.R. McKenzie, Gold, silver, chromium, and copper cermet selective surfaces for evacuated solar collectors, Appl. Phys. Lett. 34 (1979) 25–28.

[95] M. Mast, K. Gindele, M. Köhl, Ni/MgF_2 cermet films as selective solar absorbers, Thin Solid Films. 126 (1985) 37–42.

[96] X. Pang, High temperature solar selective absorber coating deposited by laser cladding, Mater. Res. Express. 4 (2017).

[97] H.D. Liu, T.R. Fu, M.H. Duan, Q. Wan, Y.M. Chen, D.J. Fu, F. Ren, Q.Y. Li, X.D. Cheng, B.

Yang, X.J. Hu, Structure and thermal stability of spectrally selective absorber based on AlCrON coating for solar-thermal conversion applications, Sol. Energy Mater. Sol. Cells. 157 (2016) 108–116.

[98] N. Selvakumar, H.C. Barshilia, K.S. Rajam, A. Biswas, Structure, optical properties and thermal stability of pulsed sputter deposited high temperature HfOx/Mo/HfO_2 solar selective absorbers, Sol. Energy Mater. Sol. Cells. 94 (2010) 1412–1420.

[99] Q. Zhang, D.R. Mills, Q. Zhang, D.R. Mills, Very low-emittance solar selective surfaces using new film structures, J. Appl. Phys. 72 (1992).

[100] F. Cao, D. Kraemer, T. Sun, Y. Lan, G. Chen, Z. Ren, Enhanced Thermal Stability of W-Ni-Al_2O_3 Cermet-Based Spectrally Selective Solar Absorbers with Tungsten Infrared Refl ectors, Adv. Energy Mater. 5 (2015).

[101] Z. Ke, D. Miao, H. Lei, M. Jianping, W. Jining, L. Xiaopeng, D. Zhejun, M. Jie, Z. Bo, Thermal stability test and ageing mechanisms study of different solar selective absorbing coatings, Surf. Coatings Technol. 323 (2017) 65–71.

[102] L. Wu, J. Gao, Z. Liu, L. Liang, F. Xia, H. Cao, Thermal aging characteristics of CrNxOy solar selective absorber coating for flat plate solar thermal collector applications, Sol. Energy Mater. Sol. Cells. 114 (2013) 186–191.

[103] M. Kotilainen, M. Honkanen, K. Mizohata, P. Vuoristo, Influence of temperature-induced copper diffusion on degradation of selective chromium oxy-nitride solar absorber coatings, Sol. Energy Mater. Sol. Cells. 145 (2016) 323–332.

[104] W. Theiss, SCOUT Thin Film Analysis Software Handbook, (2002).

[105] S.K. O'Leary, S.R. Johnson, P.K. Lim, The relationship between the distribution of electronic states and the optical absorption spectrum of an amorphous semiconductor : An empirical analysis, Appl. Phys. 82 (1997).

[106] P. Drude, Galvanomagnetische und thermomagnetische Effecte, Ann. Phys. 308 (1900) 369–402.

[107] L. Benfatto, E. Cappelluti, L. Ortenzi, L. Boeri, Extended Drude model and role of interband transitions in the midinfrared spectra of pnictides, Phys. Rev. B - Condens. Matter Mater. Phys. 83 (2011) 1–5.

[108] SEMAT-Ing, (n.d.). http://www.semat.lab.uminho.pt/index-ing.htm (accessed September 10, 2018).

[109] N.P. Barradas, C. Jeynes, R.P. Webb, U. Kreissig, R. Grötzschel, Unambiguous automatic evaluation of multiple Ion Beam Analysis data with Simulated Annealing, Nucl. Instruments Methods Phys. Res. B. 149 (1999) 233–237.

[110] CTN | IST: Scientific Infrastructures, (2018). http://www.itn.pt/facilities/uk_lab_ion_beam.htm (accessed September 10, 2018).

[111] N.P. Barradas, C. Jeynes, R.P. Webb, Simulated annealing analysis of Rutherford backscattering data, Appl. Phys. Lett. 71 (1997) 291–293.

[112] P. Scherrer, Bestimmung der Größe und der inneren Struktur von Kolloidteilchen mittels Röntgenstrahlen, Nachrichten von Der Gesellschaft Der Wissenschaften Zu Göttingen, Math. Klasse. 26 (1918) 98–100.

[113] CEMUP - Centro de Materiais da Universidade do Porto, (n.d.). http://www.cemup.up.pt/webcemup/IMICROS/IMICROS_lab/IMICROS_las_e.htm (accessed September 10, 2018).

[114] N. Fairely, CasaXPS Manual 2.3. 15, Casa Softw. Ltd. (2009) 1–177.

[115] Ruđer Bošković Institute, (n.d.). https://www.irb.hr/eng (accessed September 10, 2018).

[116] Z. Siketic, I. Bogdanovic, M. Jaks, Development of a time-of-flight spectrometer at the Ruđer Bošković Institute in Zagreb, Nucl. Instruments Methods Phys. Res. B. 266 (2008) 1328–1332.

[117] K. Arstila, J. Julin, M.I. Laitinen, J. Aalto, T. Konu, S. Kärkkäinen, S. Rahkonen, M. Raunio, J. Itkonen, J.-P. Santanen, T. Tuovinen, T. Sajavaara, Potku – New Analysis Software for Heavy Ion Elastic Recoil Detection Analysis K. Detection Analysis, Nucl. Inst. Methods Phys. Res. B. 331 (2014) 34–41.

[118] K. Arstila, T. Sajavaara, J. Keinonen, Monte Carlo simulation of multiple and plural scattering in elastic recoil detection, Nucl. Inst. Methods Phys. Res. B. 174 (2001) 163–172.

[119] C. Oliver, M. Pharr, An improved technique for determining hardness and elastic modulus using load and displacement sensing indentation experiments, J. Mater. Res. 7 (1992) 1564–1583.

[120] H. Chen, Y. Chan, J. Lee, J. Duh, Oxidation behavior of Si-doped nanocomposite CrAlSiN coatings, Surf. Coat. Technol. 205 (2010) 1189–1194.

[121] L. Castaldi, D. Kurapov, A. Reiter, V. Shklover, P. Schwaller, J. Patscheider, High temperature phase changes and oxidation behavior of Cr-Si-N coatings, Surf. Coatings Technol. 202 (2007) 781–785.

[122] L. Castaldi, D. Kurapov, A. Reiter, V. Shklover, P. Schwaller, J. Patscheider, Effect of the oxygen content on the structure, morphology and oxidation resistance of Cr-O-N coatings, Surf. Coatings Technol. 203 (2008) 545–549.

[123] M. Hirai, H. Saito, T. Suzuki, H. Suematsu, W. Jiang, K. Yatsui, Oxidation behavior of Cr-Al-N-O thin films prepared by pulsed laser deposition, Thin Solid Films. 407 (2002) 122–125.

[124] D.B. Lee, T.D. Nguyen, S.K. Kim, Air-oxidation of nano-multilayered CrAlSiN thin films between 800 and 1000 C, Surf. Coatings Technol. 203 (2009) 1199–1204.

[125] A. Karimi, M. Morstein, T. Cselle, Influence of oxygen content on structure and properties of multi-element AlCrSiON oxynitride thin films, Surf. Coatings Technol. 204 (2010) 2716–2722.

[126] Y. Chang, W. Chiu, J. Hung, Mechanical properties and high temperature oxidation of CrAlSiN/TiVN hard coatings synthesized by cathodic arc evaporation, Surf. Coatings Technol. 303 (2016) 18–24.

[127] Q.M. Wang, A superhard CrAlSiN superlattice coating deposited by a multi-arc ion plating : II . Thermal stability and oxidation, Surf. Coat. Technol. 214 (2015) 153–159.

[128] C. Hsu, D. Chen, A study on the abrasive and erosive wear behavior of arc-deposited Cr-N-O

coatings on tool steel, Thin Solid Films. 517 (2009) 1655–1661.

[129] X. Pang, K. Gao, F. Luo, H. Yang, L. Qiao, Y. Wang, A.A. Volinsky, Annealing effects on microstructure and mechanical properties of chromium oxide coatings, Thin Solid Films. 516 (2008) 4685–4689.

[130] T. Polcar, A. Cavaleiro, High-temperature tribological properties of CrAlN, CrAlSiN and AlCrSiN coatings, Surf. Coatings Technol. 206 (2011) 1244–1251.

[131] T. Polcar, T. Vitu, J. Sondor, A. Cavaleiro, Tribological performance of CrAlSiN coatings at high temperatures, Plasma Process. Polym. 6 (2009) 935–940.

[132] Q.M. Wang, Y.N. Wu, M.H. Guo, P.L. Ke, J. Gong, C. Sun, L.S. Wen, Ion-plated Al-O-N and Cr-O-N films on Ni-base superalloys as diffusion barriers, Surf. Coatings Technol. 197 (2005) 68–76.

[133] W. Ho, C.H. Shen, C.L. Chang, D.Y. Wang, Corrosion behaviors of Cr(N,O)/CrN multi-layered coatings by cathodic arc deposition, Surf. Coatings Technol. 202 (2007) 745–749.

[134] W. Ho, C.H. Shen, C.L. Chang, D.Y. Wang, Characteristics of PVD-CrAlSiN films after post-coat heat treatments in nitrogen atmosphere, Appl. Surf. Sci. 257 (2011) 3770–3775.

[135] Y. Qiu, S. Zhang, J. Lee, B. Li, Y. Wang, D. Zhao, D. Sun, Towards hard yet self-lubricious CrAlSiN coatings, Alloy. Compd. 618 (2015) 132–138.

[136] J.D. Lee, Q.M. Wang, S.H. Kim, T.G. Wang, D.W. Shin, K.H. Kim, Microstructure and mechanical properties of quaternary Cr-Si-O-N films by a hybrid coating system, Surf. Coatings Technol. 206 (2012) 3721–3727.

[137] S.K. Tien, C.H. Lin, Y.Z. Tsai, J.G. Duh, Effect of nitrogen flow on the properties of quaternary CrAlSiN coatings at elevated temperatures, Surf. Coatings Technol. 202 (2007) 735–739.

[138] C.M. Lampert, J. Washburn, Microstructure of a black chrome solar selective absorber, Sol. Energy Mater. Sol. Cells. 1 (1978) 81–92.

[139] A. Ambrosini, T.N. Lambert, C.L. Staiger, A. Hall, M. Bencomo, E.B. Stechel, Improved high temperature Solar absorbers for use in concentrating solar power central receiver applications, in: ASME. Energy Sustainability, ASME 2011 5th International Conference on Energy Sustainability, Washington, 2011: pp. 587–594.

[140] S. Khamlich, O. Nemraoui, N. Mongwaketsi, R. McCrindle, N. Cingo, M. Maaza, Black Cr/α-Cr_2O_3 nanoparticles based solar absorbers, Phys. B Phys. Condens. Matter. 407 (2011) 1509–1512.

[141] A.B.C. Ekwealor, Variations of optical and structural propertis with temperature for CrxOy thin films synthesizd in a polymer matrix by chemical bath deposition thechnique, Dig. Jorunal Nanomater. Biostructures. 9 (2014) 423–431.

[142] P. Carcia, G. Hughes, R. French, C. Torardi, G. Reynolds, L. Dieu, Thin Films for Phase-shift masks, Vac. Thin Film. (1999).

[143] F.D. Lai, L.A. Wang, Fabrication and characterization of aluminum oxide/chromium oxide superlattice for attenuated phase-shifting mask working at 193 nm wavelength, Thin Solid

Films. 409 (2002) 220–226.

[144] A. Inspektor, P.A. Salvador, Architecture of PVD coatings for metalcutting applications: A review, Surf. Coatings Technol. 257 (2014) 138–153.

[145] J.M. Wheeler, R. Raghavan, V. Chawla, M. Morstein, J. Michler, Deformation of hard coatings at elevated temperatures, Surf. Coatings Technol. 254 (2014) 382–387.

[146] A. Pélisson, M. Parlinska-Wojtan, H.J. Hug, J. Patscheider, Microstructure and mechanical properties of Al-Si-N transparent hard coatings deposited by magnetron sputtering, Surf. Coatings Technol. 202 (2007) 884–889.

[147] J.W. Kim, K.H. Kim, D.B. Lee, J.J. Moore, Study on high-temperature oxidation behaviors of Cr-Si-N films, Surf. Coatings Technol. 200 (2006) 6702–6705.

[148] Y.P. Purandare, A.P. Ehiasarian, P.E. Hovsepian, Target poisoning during CrN deposition by mixed high power impulse magnetron sputtering and unbalanced magnetron sputtering technique, Am. Vac. Soc. A. 34 (2016).

[149] M. Hassel, I. Hemmerich, H. Kuhlenbeck, H. Freund, High Resolution XPS Study of a Thin Cr2O3(111) Film Grown on Cr(110), Surf. Sci. Spectra. 4 (1998) 246–252.

[150] M.C. Biesinger, B.P. Payne, A.P. Grosvenor, L.W.M. Lau, A.R. Gerson, R.S.C. Smart, Resolving surface chemical states in XPS analysis of first row transition metals, oxides and hydroxides: Cr, Mn, Fe, Co and Ni, Appl. Surf. Sci. 257 (2011) 2717–2730.

[151] A. Conde, A.B. Cristóbal, G. Fuentes, T. Tate, J. de Damborenea, Surface analysis of electrochemically stripped CrN coatings, Surf. Coatings Technol. 201 (2006) 3588–3595.

[152] B. Subramanian, M. Jayachandran, Preparation of chromium oxynitride and chromium nitride films by DC reactive magnetron sputtering and their material properties, Corros. Eng. Sci. Technol. 46 (2011) 554–561.

[153] W. Zhao, F.J. DiSalvo, Direct access to macroporous chromium nitride and chromium titanium nitride with inverse opal structure, Chem. Commun. 51 (2015) 4876–4879.

[154] S. Ladas, L. Sygellou, S. Kennou, M. Wolf, G. Roeder, A. Nutsch, M. Rambach, W. Lerch, An X-ray photoelectron spectroscopy study of ultra-thin oxynitride films, Thin Solid Films. 520 (2011) 871–875.

[155] P. Cova, S. Poulin, O. Grenier, R.A. Masut, A method for the analysis of multiphase bonding structures in amorphous SiOxNy films, Appl. Phys. 97 (2005).

[156] V. Chawla, D. Puri, S. Prakash, B. Sidhu, Oxidation behavior of nanostructured TiAlN and AlCrN thin coatings on ASTM-SA213-T-22 boiler steel vikas, J. Miner. Mater. Charact. Eng. 9 (2010) 247–253.

[157] H.C. Barshilia, N. Selvakumar, B. Deepthi, K.S. Rajam, A comparative study of reactive direct current magnetron sputtered CrAlN and CrN coatings, Surf. Coatings Technol. 201 (2006) 2193–2201.

[158] R.T. Haasch, T.-Y. Lee, D. Gall, J.E. Greene, I. Petrov, Epitaxial CrN(001) grown and analyzed In situ by XPS and UPS. I. Analysis of as deposited Layers, Surf. Sci. Spectra. 7 (2000) 178.

[159] H. Najafi, A. Karimi, M. Morstein, Correlation Between the Oxygen Content and the Structure of $AlCrSiO_xN_{(1-x)}$ Thin Films Deposited by Pulsed DC Magnetron Sputtering, NSTI-Nanotech. 1 (2010) 631–634.

[160] M. Stüber, U. Albers, H. Leiste, K. Seemann, C. Ziebert, S. Ulrich, Magnetron sputtering of hard Cr-Al-N-O thin films, Surf. Coatings Technol. 203 (2008) 661–665.

[161] R. Kaindl, B. Sartory, J. Neidhardt, R. Franz, A. Reiter, P. Polcik, R. Tessadri, C. Mitterer, Semi-quantitative chemical analysis of hard coatings by Raman micro-spectroscopy: the aluminium chromium nitride system as an example, Anal. Bioanal. Chem. 389 (2007) 1569–1576.

[162] J. Soldán, J. Neidhardt, B. Sartory, R. Kaindl, R. Č, P.H. Mayrhofer, Structure – property relations of arc-evaporated Al–Cr –Si–N coatings, Surf. Coat. Technol. 202 (2008) 3555–3562.

[163] C. Gupta, S.H. Chan, A. Agarwal, N. Hatui, S. Keller, U.K. Mishra, First demonstration of AlSiO as gate dielectric in GaN FETs ; applied to a high performance OG-FET, IEEE Electron Device Lett. 3106 (2017).

[164] J.W. Lim, J. Yun, J.H. Lee, Electrical properties of aluminum silicate films grown by plasma nnhanced atomic layer deposition, Electrochem. Solid-Sate Lerrers. 9 (1) (2006) F8–F11.

[165] Y.G. Shen, Y.W. Mai, Influences of oxygen on the formation and stability of A15 B-W thin films, Mater. Sci. Eng. A. 284 (2006) 176–183.

[166] I.A. Weerasekera, S.I. Shah, D. V. Baxter, K.M. Unruh, Structure and stability of sputter deposited beta-tungsten thin films, Appl. Phys. Lett. 64 (1994) 3231–3233.

[167] G.S. Chen, L.C. Yang, H.S. Tian, C.S. Hsu, Evaluating substrate bias on the phase-forming behavior of tungsten thin films deposited by diode and ionized magnetron sputtering, Thin Solid Films. 484 (2005) 83–89.

[168] H.G. Craighead, R. Bartynski, R.B. A, L. Wojcik, A.J. Sievers, Metal/Insulator composite selective absorbers, Sol. Energy Mater. 1 (1979) 105–124.

[169] M. Farooq, Z.H. Lee, Computations of the optical properties of metal/insulator-composites for solar selective absorbers, Renew. Energy. 28 (2003) 1421–1431.

[170] H. Wang, V. Prasad Sivan, A. Mitchell, G. Rosengarten, P. Phelan, L. Wang, Highly efficient selective metamaterial absorber for high-temperature solar thermal energy harvesting, Sol. Energy Mater. Sol. Cells. 137 (2015) 235–242.

[171] IRENA, Renewable Energy Technologies Cost Analysis Series: Concentrating Solar Power, Compr. Renew. Energy. 3 (2012) 595–636.

[172] T. Polcar, A. Cavaleiro, High-temperature tribological properties of CrAlN, CrAlSiN and AlCrSiN coatings, Surf. Coatings Technol. 206 (2011) 1244–1251.

[173] S. Veprek, R.F. Zhang, M.G.J. Veprek-Heijman, S.H. Sheng, A.S. Argon, Superhard nanocomposites: Origin of hardness enhancement, properties and applications, Surf. Coatings Technol. 204 (2010) 1898–1906.

[174] K. Bobzin, N. Bagcivan, P. Immich, S. Bolz, R. Cremer, T. Leyendecker, Mechanical properties and oxidation behaviour of (Al,Cr)N and (Al,Cr,Si)N coatings for cutting tools deposited by

HPPMS, Thin Solid Films. 517 (2008) 1251–1256.

[175] J. Wang, B. Wei, Q. Wei, D. Li, Optical property and thermal stability of Mo/Mo-SiO_2/SiO_2 solar-selective coating prepared by magnetron sputtering, Phys. Status Solidi Appl. Mater. Sci. 208 (2011) 664–667.

[176] E. Wäckelgard, A. Mattsson, R. Bartali, R. Gerosa, G. Gottardi, F. Gustavsson, N. Laidani, V. Micheli, D. Primetzhofer, B. Rivolta, Development of W-SiO_2 and Nb-TiO_2 solar absorber coatings for combined heat and power systems at intermediate operation temperatures, Sol. Energy Mater. Sol. Cells. 133 (2015) 180–193.

[177] M.J. O'Keefe, J.T. Grant, Phase transformation of sputter deposited tungsten thin films with A-15 structure, J. Appl. Phys. 79 (1996) 9134–9141.

[178] D.W. Berreman, F.C. Unterwald, Adjusting poles and zeros of dielectric dispersion to fit reststrahlen of $PrCl_3$ and $LaCl_3$, Phys. Rev. 174 (1968).

[179] M.A. Ordal, L.L. Long, R.J. Bell, S.E. Bell, R.R. Bell, R.W. Alexander, C.A. Ward, Optical properties of the metals Al, Co, Cu, Au, Fe, Pb, Ni, Pd, Pt, Ag, Ti, and W in the infrared and far infrared, Appl. Opt. 22 (1983) 1099.

[180] C.T. Kirk, Quantitative analysis ofthe effect of disorder-induced mode coupling on infrared absorption in silica, Phys. Rev. B. 38 (1988).

[181] L. Stoch, M. Sroda, Infrared spectroscopy in the investigation of oxide glasses structure, J. Mol. Struct. 512–511 (1999) 77–84.

[182] J.A. Luna-López, G. García-Salgado, T. Díaz-Becerril, J.C. López, D.E. Vázquez-Valerdi, H. Juárez-Santiesteban, E. Rosendo-Andrés, A. Coyopol, FTIR, AFM and PL properties of thin SiOxfilms deposited by HFCVD, Mater. Sci. Eng. B. 174 (2010) 88–92.

[183] R. Al-Oweini, H. El-Rassy, Synthesis and characterization by FTIR spectroscopy of silica aerogels prepared using several $Si(OR)_4$ and $R''Si(OR')_3$ precursors, J. Mol. Struct. 919 (2009) 140–145.

[184] A. Lehmann, L. Schumann, K. Hubner, Optical Phonons in Amorphous Silicon Oxides (II), Phys. Stat. Sol. B. 121 (1984) 505–511.

[185] R. Salh, A. Von Czarnowski, M. V. Zamoryanskaya, E. V. Kolesnikova, H.J. Fitting, Cathodoluminescence of SiOx under-stoichiometric silica layers, Phys. Stat. Sol. A. 203 (2006) 2049–2057.

[186] D.I. Voll, C.H. Lengauer, A.N. Beran, H.A. Schneider, Infrared band assignment and structural refinement of Al-Si , Al-Ge , and Ga-Ge mullites, Eur. J. Miner. 13 (2001) 591–604.

[187] J. -Ch. Buhl, Crystallization of Hydrosodalite $Na_6[AlSiO_4]_6(H2O)_8$ and Tetrahydroborate Sodalite $Na_8[AlSiO_4]_6(BH_4)_2$ inside the Openings of Wafer-Thin Steel Mesh, Adv. Chem. Eng. Sci. 7 (2017) 277–290.

[188] D. Voll, P. Angerer, A. Beran, H. Schneider, A new assignment of IR vibrational modes in mullite, Vib. Spectrosc. 30 (2002) 237–243.

[189] F.Y. Xie, L. Gong, X. Liu, Y.T. Tao, W.H. Zhang, S.H. Chen, H. Meng, J. Chen, XPS studies on surface reduction of tungsten oxide nanowire film by Ar^+ bombardment, J. Electron Spectros.

Relat. Phenomena. 185 (2012) 112–118.

[190] X.X. Zhang, Y.Z. Wu, B. Mu, L. Qiao, W.X. Li, J.J. Li, P. Wang, Thermal stability of tungsten sub-nitride thin fi lm prepared by reactive magnetron sputtering, J. Nucl. Mater. 485 (2017) 1–7.

[191] P. Perez-Romo, C. Potvin, J.-M. Manoli, G. Djega-Mariadassou, Phosphorus-doped tungsten oxynitrides : synthesis , characterization , and catalytic behavior in propene hydrogenation and n-heptane isomerization, J. Catal. 205 (2002) 191–198.

[192] D. Cho, T. Chang, C. Shin, Variations in the surface structure and composition of tungsten oxynitride catalyst caused by exposure to air, Catal. Letters. 67 (2000) 163–169.

[193] C. Louro, A. Cavaleiro, F. Montemor, How is the chemical bonding of W-Si-N sputtered coatings ?, Surf. Coat. Technol. 142–144 (2001) 964–970.

[194] Y. Jiang, J.F. Yang, R. Liu, X.P. Wang, Q.F. Fang, Oxidation and corrosion resistance of WC coated tungsten fabricated by SPS carburization, J. Nucl. Mater. 450 (2014) 75–80.

[195] R. Azimirad, P. Khosravi, A.Z. Moshfegh, Influence of hydrogen reduction on growth of tungsten oxide nanowires, J. Exp. Nanosci. 7 (2012) 597–607.

[196] P. Uppachai, V. Harnchana, S. Pimanpang, V. Amornkitbamrung, A.P. Brown, R.M.D. Brydson, A substoichiometric tungsten oxide catalyst provides a sustainable and efficient counter electrode for dye-sensitized solar cells, Electrochim. Acta. 145 (2014) 27–33.

[197] J. Zhang, J.P. Tu, X.H. Xia, Y. Qiao, Y. Lu, An all-solid-state electrochromic device based on NiO/WO_3 complementary structure and solid hybrid polyelectrolyte, Sol. Energy Mater. Sol. Cells. 93 (2009) 1840–1845.

[198] Y. Dong, J. Li, Tungsten nitride nanocrystals on nitrogen-doped carbon black as efficient electrocatalysts for oxygen reduction reactions, Chem. Commun. 51 (2014) 572–575.

[199] M. Rahman, S. Kamrul, Ellipsometric , XPS and FTIR study on SiCN films deposited by hot-wire chemical vapor deposition method, Mater. Sci. Semicond. Process. 42 (2016) 373–377.

[200] G.M. Ingo, N. Zacchetti, D. Sala, C. Coluzza, Xray photoelectron spectroscopy investigation on the chemical structure of amorphous silicon nitride (aSiNx), J. Vac. Sci. Technol. 7 (2014).

[201] H.J. Kim, I. Bae, S. Cho, J. Boo, B. Lee, J. Heo, I. Chung, B. Hong, Synthesis and characteristics of NH2- functionalized polymer films to align and immobilize DNA molecules, Nanoscale Res. Lett. 7 (2012).

[202] N.H. Turner, A.M. Singlet, Determination of Peak Positions and Areas from Wide-scan XPS Spectra, Surf. Interface Anal. 15 (1990) 215–222. doi:10.1002/sia.740150305.

[203] L. Berggren, G.A. Niklasson, Influence of sputtering conditions on the solar and luminous optical properties of amorphous LixWoythin films, Sol. Energy Mater. Sol. Cells. 85 (2005) 573–586. doi:10.1016/j.solmat.2004.05.016.

[204] H.Y. Wong, C.W. Ong, K.W. Wong, S.P. Wong, W.Y. Cheung, Effects of ion beam bombardment on electrochromic tungsten oxide films studied by X-ray photoelectron spectroscopy and Rutherford back-scattering, Thin Solid Films. 376 (2000) 131–139.

[205] T. Yang, Y. Zhang, C. Li, Chemical and structural analysis of solvothermal synthesized tungsten oxide nanotube without template and its hydrogen sensitive property, J. Alloys Compd. 584 (2014) 546–552.

[206] H. Li, A. Belkind, F. Jansen, Z. Orban, An in situ XPS study of oxygen plasma cleaning of aluminum surfaces, Surf. Coatings Technol. 92 (1997) 171–177.

[207] M. Shioji, T. Shiraishi, K. Takahashi, H. Nohira, K. Azuma, Y. Nakata, Y. Takata, S. Shin, K. Kobayashi, T. Hattori, X-ray photoelectron spectroscopy study on SiO2/Si interface structures formed by three kinds of atomic oxygen at 300 °C, Appl. Phys. Lett. 84 (2004) 3756–3